Ca^{2+} handling and stress responses of photoreceptor mitochondria

Rachel Alicia Hutto

A dissertation

submitted in partial fulfillment of the requirements for the degree of

Doctor of Philosophy

University of Washington
2020

Reading Committee:

James B. Hurley, Chair

Susan E. Brockerhoff

Suzanne Hoppins

Program Authorized to Offer Degree:
Biochemistry

Abstract

Ca^{2+} handling and stress responses of photoreceptor mitochondria

Rachel Alicia Hutto

Chair of the Supervisory Committee:
Professor James B. Hurley
Biochemistry

Maintenance of mitochondrial function and integrity is essential for cellular health. Mitochondria play key roles in ATP generation, cellular signaling, and control of cell death. These functions are linked to mitochondrial Ca^{2+} content, which until recently has been thought to be controlled primarily by the mitochondrial Ca^{2+} uniporter (MCU) complex. We characterized this complex in photoreceptors, specialized neurons in the eye that rely on Ca^{2+} signaling for function, require a high rate of ATP production, and have a unique mitochondrial architecture. I was surprised to find that retinas express exceptionally low levels of MCU protein and that abrogating its expression does not compromise photoreceptor survival or function. Instead, my findings indicate that in the absence of MCU an alternative pathway in photoreceptor mitochondria can support uptake of Ca^{2+}. I also showed that overexpression of MCU in cone photoreceptors accelerates recovery from light stimulation and alters citric acid cycle metabolite pools. MCU overexpression also compromises mitochondrial integrity, but cones can survive this chronic mitochondrial Ca^{2+} stress for many months. Cones respond to mitochondrial stress (Ca^{2+}, translational, and cold stress) by selectively trafficking damaged mitochondria away from their normal location in the ellipsoid. These mislocalized mitochondria are recycled via lysosomes and can even be exported from the cell. My dissertation highlights the unique characteristics of photoreceptor mitochondria and demonstrates that photoreceptors have adaptations to mitochondrial stress that promote their survival.

Table of Contents

Acknowledgements

A thesis is usually acknowledged as the work of one person, but it is truly the work of many. Throughout my thesis work I have been helped and supported by so many people that have enriched my academic journey and personal life. I would first like to thank my wonderful mentors Dr. James Hurley and Dr. Susan Brockerhoff, who guided me throughout my studies with insight, patience, and kindness. They not only advised me in regard to the science presented here, but also generously supported my personal development and pursuits outside of the lab. I count myself incredibly lucky to have had both of them as advisors. I would also like to thank my thesis committee (Suzanne Hoppins, Rong Tian, and Justin Kollman) for their guidance and helpful ideas throughout graduate school.

I have been fortunate to work with many talented scientists in the Hurley and Brockerhoff labs. Celia Bisbach is chief among them, and her meticulous work and insight have made this thesis possible. I am also grateful for the generous gifts of time, brain power, and friendship from Connor Jankowski, Michelle Giarmarco, Benjamin Bauer, Kristine Tsantilas, Whitney Cleghorn, Abbi Engel, Daniel Brock, Ashlee Evans, William Ge, Brian Robbings, Jon Linton, and Mark Kanow. My incredible collaborators have not only worked to collect exhaustive electrophysiology data, they have also offered experimental insights and thoughtful feedback: thank you to Fatima Abbas, Frans Vinberg, Deepak Poria, and Vladimir J. Kefalov. Much of the insights from this work were gained through electron microscopy, and Ed Parker made this possible. Finally, I would be nowhere without the tireless work of the animal facility staff: thank you Stanley Kim and Jeanot Muster for the daily work you do.

Aside from the support of scientists in my field, I have been blessed with the friendship of an incredible cohort of scientists when I began graduate school. They have supported me through the good and bad science and enriched my life. To have the friendship of such brilliant and wonderful people is truly a blessing. Thank you, Alexandria Walls, Robert Langan, Domnita Rusnac, Eleanor Vane, and Gülsima Usluer.

I must also thank my wonderful and loving family for all of their support – in graduate school, but also throughout my life. Mom and Dad – you always pushed me to try my best but made sure I always knew that I didn't have to be perfect. Grandma and Grandpa – the generous heart that you have shown me has inspired me to live life to the fullest. The love of my family has helped me weather the turbulent times in my life, a barrier against the crashing waves.

I am privileged to be married to a wonderful, supportive partner. Sean Gillespie, thank you for being my rock, for sharing your love and kindness, and for enriching my life each day. Your support throughout creating this thesis has been incredible and I will always be so grateful.

Chapter 1: Introduction

Maintaining mitochondrial health is critical for cellular function

Mitochondria are essential for eukaryotic and multicellular life. Mitochondria are primary drivers of ATP production, providing energy that powers cellular function. Mitochondria are also hubs for metabolic pathways - the citric acid cycle provides biosynthetic precursors of lipids, nucleotides, amino acids, and glucose. Mitochondria can even modulate diverse cellular signals, coupling them to metabolic output and mitochondrial dynamics.[1] However, these same organelles that support cellular function can also stimulate apoptosis or necrosis if they are compromised.[2]

Mitochondrial dysfunction has been implicated in the pathophysiology of many diseases. The first documented disease linked to mitochondria was published in 1962, when Luft and colleagues deduced that a woman suffering from weight loss despite excess caloric intake suffered from mitochondrial uncoupling.[3] Since then, mitochondrial dysfunction has been associated with numerous diseases affecting a variety of systems: type II diabetes,[4] sarcopenia,[5] Alzheimer's disease,[6] cardiovascular disease,[7] cancer,[8] and more (for review, see ref [9]). Mitochondria are even implicated in the gradual loss of cell viability during aging and have been therapeutic targets for extending healthspan.[10] These observations make it clear that maintenance of proper mitochondrial function is key for long-term cell function and viability.

How do cells support a healthy mitochondrial network? First, let's examine some of the numerous triggers of mitochondrial stress and their outcomes, summarized in **Figure 1.1**. Mitochondria can fail due to genetic factors, including mutations in the mitochondrial genome or in parts of the nuclear genome that encode for mitochondrial proteins. In the case of mitochondrial DNA, which can have a high copy number and lacks the robust repair mechanisms of nuclear DNA, mutations can be readily acquired over a lifetime. Metabolic factors are also associated with mitochondrial stress, as both oversupply and deficiency of metabolites can cause dysfunction. Mitochondria act as stores for a variety of ions (primarily Fe^{2+} and Ca^{2+}), and ion overload disrupts mitochondrial integrity and can lead directly to cell death. Finally, extrinsic factors such as oxygen levels, environmental toxins, inhibitors of the electron transport chain, and even infectious disease can compromise mitochondrial health. [11,12]

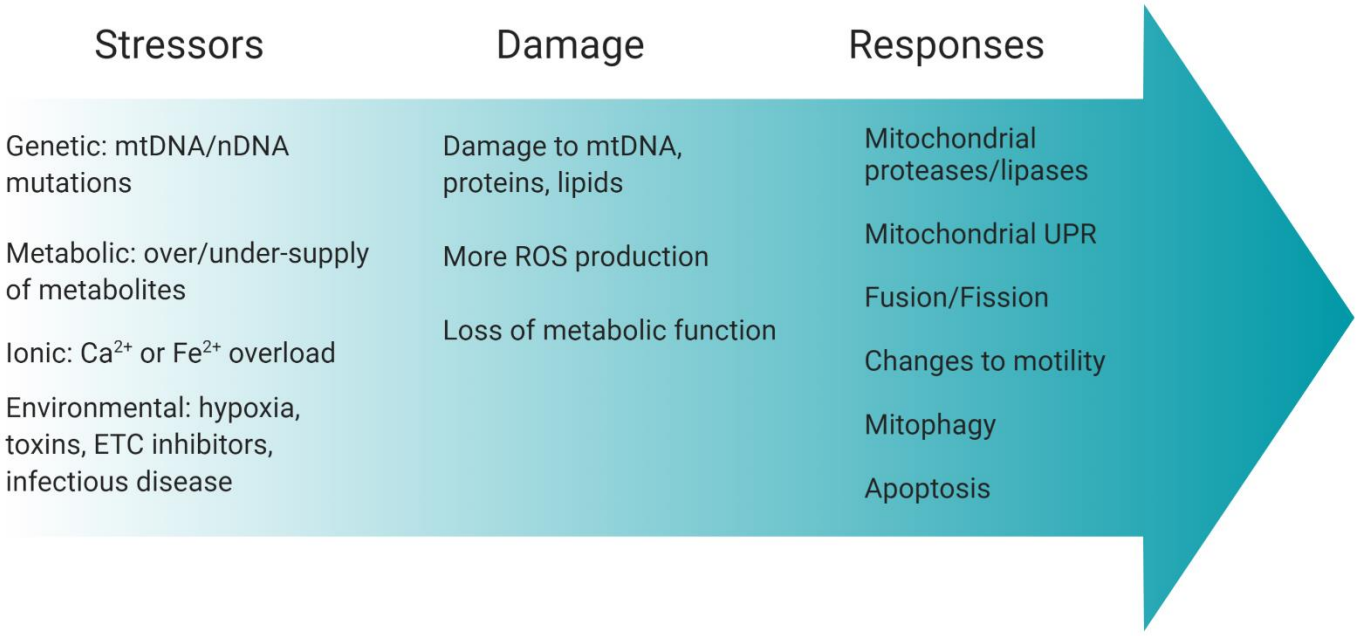

Figure 1.1: Summary of mitochondrial stressors, the damage they can cause, and the mitochondrial responses. Key: mtDNA = mitochondrial DNA, n = nuclear DNA, ETC = electron transport chain, ROS = reactive oxygen species, UPR = unfolded protein response.

In response to a stressor, much of the damage to mitochondria – their proteins, lipids, and DNA – is mediated by reactive oxygen species (ROS). These are generated by the mitochondria themselves upon "leak" of single electrons to oxygen, whether from the electron transport chain complexes or from matrix enzymes including aconitase, α-ketoglutarate dehydrogenase, and pyruvate dehydrogenase.[13] ROS-mediated damage to mitochondrial components compromise mitochondrial structure, metabolism, and ATP generation. While mitochondria are particularly vulnerable to ROS, they can also fight back. Mitochondria contain enzymes that can remove ROS and can degrade damaged proteins and lipids via proteases and lipases.[11,13] ROS accumulation makes mitochondria an unfavorable environment for protein folding, but mitochondria can combat this by activating the mitochondrial unfolded protein response.[14]

Mitochondria are dynamic, which allows them to adapt to various stressors and maintain homeostasis. Mitochondrial movement was first documented in 1915 by Margaret Lewis; without a camera to capture it, she painstakingly illustrated dynamic mitochondria in living cells.[15] Mitochondria fuse and divide, actively moving around the cell. This is essential to mitochondrial quality control: fusion allows mitochondria to share factors such as mtDNA, and fission allows dysfunctional mitochondria to be separated from the healthy network.[16,17]

Mitochondrial movement can be altered in response to stressors. Often, mitochondrial damage stops mitochondrial movement. Stresses such as elevated mitochondrial Ca^{2+} and ROS arrest mitochondrial motility.[18–20] Loss of mitochondrial membrane potential can also stop mitochondria, as this recruits the ubiquitin ligase Parkin to mitochondria and targets their transport machinery for degradation.[21,22] Sometimes, stress can actually cause mitochondria to move: the mitochondrial anchoring protein syntaphilin can be released upon chronic mitochondrial stress, and collapse of the mitochondrial network around the nucleus can be triggered by hypoxia and proteosomal stress.[18,23,24] Immobilizing defective mitochondria may facilitate their segregation from the rest of the mitochondrial network, while moving mitochondria toward the nucleus may allow communication between the organelles to coordinate a response.[25]

When all else fails, and mitochondria are “beyond saving”, the cell can resort to mitophagy. Mitophagy is the selective degradation of mitochondria by autophagy machinery, which involves surrounding mitochondria with an autophagosomal membrane and eventual fusion of the membrane-bound organelle with an acidic lysosome. The exact molecular players that govern formation of the autophagosomal membrane around mitochondria are still poorly understood. One well-characterized initiator of autophagy is mitochondrial depolarization, which stabilizes PINK1, recruits Parkin to the mitochondria, and facilitates phagosome formation.[26] However, mitochondrial depolarization and the PINK1/Parkin system are not required for mitophagy - autophagosomes can be recruited to mitochondria with intact membrane potential and basal mitophagy is uncompromised upon loss of PINK1.[27,28]

Finally, in some cases, it is possible for a cell to outsource mitochondrial recycling altogether. Cells can form nanotubules between each other to facilitate the transfer of organelles including mitochondria.[29,30] Sometimes this can occur when the donor cell is “altruistic”, supplying healthy mitochondria to stressed cells to rescue mitochondrial dysfunction.[31] However, retinal ganglion cells can extrude their mitochondria, letting nearby astrocytes degrade them.[32] The axons of these neurons stretch from the back of the eye to the optic nerve head of the brain. Their long axons make it an energetically costly task to transport axonal mitochondria back to the cell body for mitophagy, so this is a particularly advantageous adaptation. A similar phenomenon has been observed in C. elegans neurons, which can extrude large vesicles (“exophers”) that contain mitochondria upon cellular and mitochondrial stress.[33] This is not restricted to neurons, as HeLa cells can extrude mitochondria upon ROS damage.[34]

Mitochondrial function is linked to Ca^{2+} content

Mitochondrial function is tied to the concentration of Ca^{2+} in the mitochondrial matrix. The Ca^{2+}-dependent dehydrogenases of the citric acid cycle have enhanced flux when mitochondrial Ca^{2+} is elevated.[35,36] Increasing mitochondrial Ca^{2+} has been shown to increase ATP generation, and Ca^{2+} may regulate the activity of ATP synthase directly.[37–40] Though the mechanism is a topic of debate, mitochondrial Ca^{2+} uptake can promote ROS production.[41] Ca^{2+} uptake into the mitochondria can influence localized Ca^{2+} signals in the cytosol, decreasing their amplitude or spatial patterning.[42,43] Finally, excessive levels of mitochondrial matrix Ca^{2+} are the essential trigger for opening of the mitochondrial permeability transition pore, which begins the cascade for apoptotic cell death.[44]

Mitochondrial Ca^{2+} content is controlled by channels on the inner and outer mitochondrial membrane. Ca^{2+} is thought to primarily enter the outer membrane through VDAC, a channel with a large pore and low selectivity that allows mitochondrial Ca^{2+} in the inner membrane space.[45] Since 1961, when Ca^{2+} conductance into the mitochondrial matrix was first characterized, we have known of the existence of a high conductance, selective uniporter for Ca^{2+} on the mitochondrial inner membrane.[46] However, the molecular identity of this protein remained elusive until 2011, when two groups (through independent approaches) discovered the molecular identity of the channel termed MCU (mitochondrial calcium uniporter).[47,48] The MCU channel is modulated by multiple proteins, including those necessary for its function in vertebrates (EMRE) and regulators of the channel's Ca^{2+} conductance (MICU1, MICU2, MICU3).[49–53] Many other proteins have also been reported to interact with MCU.[54–59]

Expression of MCU and its regulators is tissue-specific, and thus there are tissue-specific responses to modulating those components. Skeletal muscle is characterized by an abundance of MCU and relatively little expression of its regulators MICU1/2.[60] Loss of MCU specifically in skeletal muscle impairs exercise performance and oxidative phosphorylation mediated by a decrease in pyruvate dehydrogenase activity.[61] Overexpression of MCU in skeletal muscle increases muscle size and protects against muscle atrophy.[62] Neurons express a tissue-specific enhancer of MCU Ca^{2+} conductance, MICU3.[53] Accordingly, MCU overexpression in neurons causes neuronal cell death and its loss is protective in neurons lacking key mitophagy components.[63–65]

Photoreceptors are unique neurons with unique mitochondria

Photoreceptors are the specialized neurons in the eye that change their membrane potential in response to incoming light in a process called phototransduction. Photoreceptors transduce that signal into neurochemical changes that are received by other retinal neurons and transmit information to the brain. There are two primary types of photoreceptors in vertebrates: rods, which respond to dim light, and cones, which respond to bright light. To perform their light-sensing function, photoreceptors have several unique characteristics that differentiate them from other neurons.

The structure of photoreceptors supports their function (**Figure 1.2**). The relatively short axons of photoreceptors culminate in ribbon synapses. These specialized synapses allow the cells to release hundreds of vesicles per second, facilitating a large gradient of neurotransmitter release that can represent the dynamic range of light stimuli.[66] Opposite the synapse, photoreceptors have a unique structure called the outer segment, a dense stack of membranes which contain the proteins necessary for detection of light.

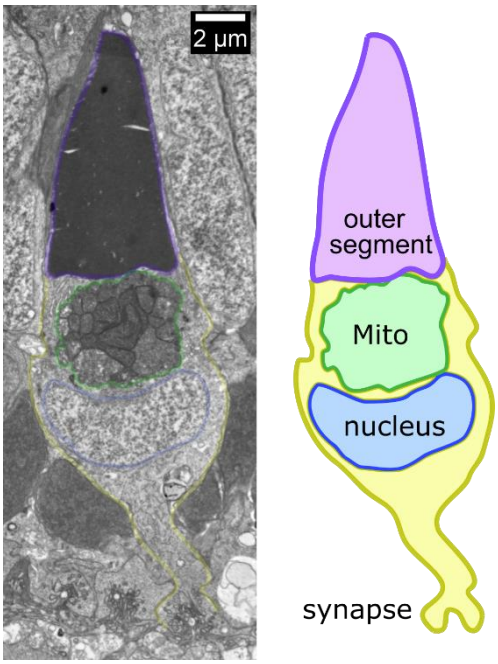

Figure 1.2: Anatomy of a photoreceptor.

Electron micrograph of a cone photoreceptor from a 1 month old zebrafish. The outer segment (purple) is composed of membrane stacks where phototransduction occurs. The specialized ribbon synapse (yellow) releases neurotransmitter-containing vesicles. The dense mitochondrial cluster (Mito, green) is in the ellipsoid region of the cell, between the nucleus (blue) and outer segment.

The mitochondria of photoreceptors are also unique. Photoreceptor mitochondria are highly concentrated in a region of the cell body called the ellipsoid, between the outer segment and the rest of the cell. As much as 85% of the volume of the ellipsoid is comprised of mitochondria in

primate photoreceptors.[67] In avascular retinas, where availability of oxygen in the inner retina is limited, mitochondria are reported to be exclusively at the ellipsoid region of photoreceptors.[68] Photoreceptor mitochondria have great structural diversity between animals: ellipsoids can contain mitochondria in dense clusters, tubular structures, or even hollow rings. The appearance, structure, and cristae patterning of these mitochondria are highly variable among vertebrates and often unique to photoreceptors.[69] Cone photoreceptors can contain "mega-mitochondria", and express cone-specific genes that enable the production of giant mitochondria.[70] Ellipsoid mitochondria may even serve a light-guiding function, focusing incoming light from the inner retina and synapse onto the outer segment.[67]

To properly respond to light, photoreceptors rely on Ca^{2+} as a second messenger.[71,72] Light stimulation results in a net efflux of Ca^{2+} and Na^{+} from the outer segment that causes hyperpolarization of the membrane; the resulting decrease in Ca^{2+} alters activities of several proteins that counteract the effect of light. At the synapse, hyperpolarization closes voltage-gated Ca^{2+} channels, halting the influx of Ca^{2+} ions necessary to stimulate release of the neurotransmitter glutamate to downstream neurons. In the darkness, the constitutive pumping of ions across the plasma membrane and the energetically demanding task of neurotransmission contribute to the extraordinarily high ATP demand of photoreceptors.[73] Overall, there is less energy demand in light.

Photoreceptor dysfunction and death have been linked to changes in Ca^{2+} homeostasis.[74,75] Organelles help maintain Ca^{2+} homeostasis, and in photoreceptors cytosolic Ca^{2+} is buffered and regulated by both the ER and the mitochondria.[76] Photoreceptors undergo huge Ca^{2+} fluctuations in response to light, and it has been speculated that ellipsoid mitochondria may protect the cell body from the cytosolic Ca^{2+} that accumulates in the outer segment in darkness.[77–79] When I started my thesis work, nothing was known about how photoreceptor mitochondria buffer cytosolic Ca^{2+} and the role of the MCU complex in photoreceptor health and function had not been investigated.

Moving forward: Characterizing Ca^{2+} dynamics and stress adaptations in photoreceptor mitochondria

The purpose of this thesis is to characterize the specialization of photoreceptor mitochondria, with an emphasis on the MCU complex. We first assessed MCU complex components in the retina and found that photoreceptors express a level of MCU that is unusually low compared to other tissues. We hypothesized that this may be protective, limiting Ca^{2+} inflow to prevent mitochondrial dysfunction and cell death. Consistent with this hypothesis, we found that MCU overexpression in photoreceptors compromises mitochondrial integrity whereas loss of MCU does not affect photoreceptor health. Cytosolic Ca^{2+} changes and the photoreceptor response to light are altered upon MCU overexpression but remain unchanged when MCU is lost. The Ca^{2+}-sensitive dehydrogenases of the citric acid cycle have increased flux upon overexpression of MCU, while loss of MCU does not seem to appreciably affect their activity. In fact, retinas appear to rely on another unknown mechanism for Ca^{2+} entry into mitochondria.

Surprisingly, we found that despite the extensive mitochondrial abnormalities observed in MCU-overexpressing photoreceptors, the cells were able to survive the stress for many months. Our investigations revealed that photoreceptors respond to Ca^{2+}-induced mitochondrial stress by selectively trafficking damaged mitochondria away from the ellipsoid region of the cell. Based on this observation we also showed that this process of mitochondrial sorting is active in healthy photoreceptors and it can be triggered by other modes of mitochondrial stress. In normal retinas, mislocalized mitochondrial are preferentially recycled in lysosomes, and photoreceptors can export mitochondria into the inner retina. These studies highlight the remarkable adaptations of photoreceptor mitochondria and provide novel insights into the mechanisms by which photoreceptors tolerate chronic mitochondrial stress.

Chapter 2: Increasing Ca^{2+} in photoreceptor mitochondria alters metabolites, accelerates photoresponse recovery, and reveals adaptations to mitochondrial stress

Introduction

Photoreceptors, the neurons that initiate vision, must survive in a hostile cellular environment. In the retina they are exposed to damaging light radiation, experience 100-fold fluctuations in intracellular Ca^{2+}, are located near blood vessels with high levels of O_2, and use ATP faster than most other types of cells. Despite these chronic stressors, most people retain vision throughout their lives, highlighting the extraordinary ability of photoreceptors to regulate cellular homeostasis and maintain viability.

Maintenance of Ca^{2+} homeostasis is critical for photoreceptor function and survival. Photoreceptors rely on Ca^{2+} as a second messenger for recovery from transient light signals, adaptation to constant illumination, and neurotransmission.[71,72] Both chronic elevations and chronic decreases in cytosolic Ca^{2+} have been implicated in photoreceptor cell death and retinal disease.[74,80] Ca^{2+}-associated cell death is often mediated by mitochondria, as mitochondrial Ca^{2+} overload triggers opening of the mitochondrial permeability transition pore (mPTP) and subsequent cell death.[44] Accordingly, increases in cellular Ca^{2+} in isolated rat retinas cause photoreceptor-selective apoptosis that depends on mPTP activity.[81]

Mitochondrial Ca^{2+} uptake can also be beneficial to the cell. Cytosolic Ca^{2+} is buffered by mitochondria, and in photoreceptors the precise localization of mitochondria to the ellipsoid can protect the cell body from the cytosolic Ca^{2+} that accumulates in the outer segment in darkness.[77,78,79] Uptake of Ca^{2+} into mitochondria can also influence their energetic output.[40] However, metabolic responses to changes in mitochondrial Ca^{2+} vary across tissues, reflecting the diverse metabolic demands of different cell types.[82]

Ca^{2+} import into the mitochondrial matrix occurs via the mitochondrial Ca^{2+} uniporter complex (MCU complex), comprised of a multimer of the pore-forming protein MCU and many associated regulatory proteins.[47–49] The protein EMRE is necessary for MCU function in vertebrates, while MICU proteins (MICU1-3) tune Ca^{2+} uptake through the uniporter complex.[50–53] This degree of regulation, along with the variability of modulator expression across tissues, implies that the

activity of the MCU complex is attuned to cellular needs and critical in the interplay between optimal function and prolonged survival.

To investigate the relationship between mitochondrial Ca^{2+} and photoreceptor physiology we analyzed expression of MCU and its regulators MICU1, MICU2 and MICU3 in zebrafish retina. While regulator expression is similar between retinal and brain tissue, MCU expression is unusually low in cone photoreceptors. We hypothesized that limiting mitochondrial Ca^{2+} influx via MCU may serve a protective function, so we generated zebrafish models of cone-specific MCU overexpression to test how cones respond to the increase of this key modulator of mitochondrial Ca^{2+}.

Results

Cones express low levels of MCU

We developed a custom antibody against amino acids 21-202 of zebrafish MCU and validated its specificity with a global zebrafish MCU knock-out (KO, **Figure 2.1A**). MCU protein expression is high in brain, lower in the heart, and lowest in the retina (**Figure 2.1A**). Retina resembles heart when MCU is normalized to mitochondrial proteins cytochrome oxidase (MTCO1) and succinate dehydrogenase (SDH) (**Figure 2.1B**). However, transcript expression of the MCU regulators MICU1, MICU2, and MICU3 resembles brain more than heart (**Figure 2.1C**).

Our antibody was not suitable for immunohistochemistry of endogenous MCU, so we used the pde6c$^{-/-}$ zebrafish model of cone-specific degeneration to estimate MCU expression in cones. In this model, cones degenerate and rod photoreceptors populate the retina.[83] Cones have more mitochondrial volume than rods.[67,84] Without cones, there are fewer mitochondrial membrane proteins but no significant loss of MCU signal (**Figure 2.1D,E**). This shows that cone mitochondria must have less MCU than mitochondria of other retinal neurons.

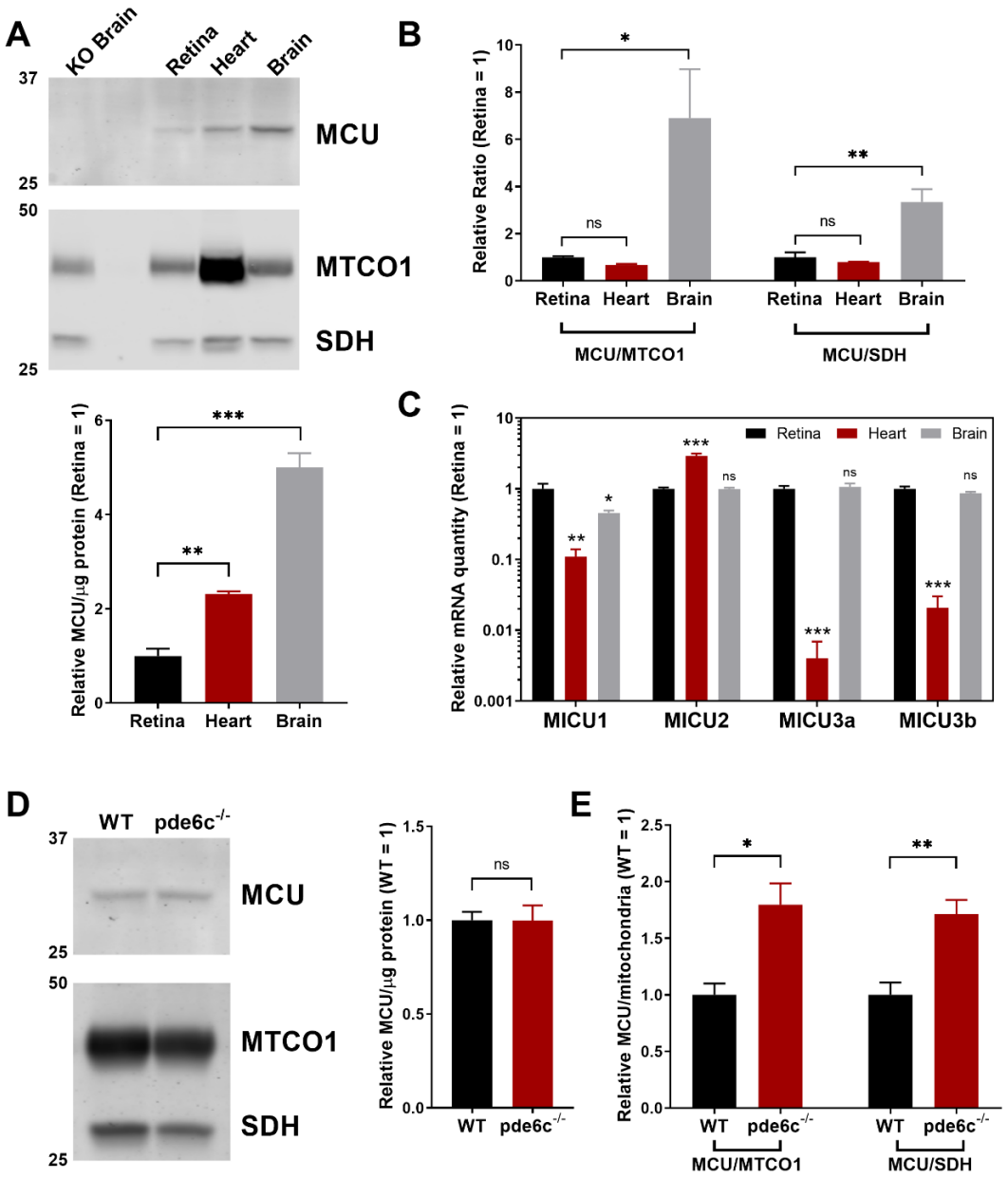

Figure 2.1: MCU expression is limited in the retina, particularly in cones.

A. Western blot of zebrafish tissue lysate, enriched for mitochondrial proteins and probed for MCU, mitochondrial cytochrome oxidase (MTCO1), and succinate dehydrogenase (SDH). Samples were pooled from either 4 retinas, 2 hearts, or 1 brain and performed with n=3 replicates of each pool. Each lane contains 8 µg of protein. The lower panel shows quantification of the replicates, normalized to retina tissue. The mean is reported and bars = standard error. **p<0.01, ***p<0.001 using ANOVA followed by Dunnett post-hoc test (comparison to retina).

B. Within each lane from gels analyzed in panel A, the ratios of MCU signal to the mitochondrial proteins MTCO1 and SDH were determined. Values were normalized relative to retina tissue. The mean is reported and bars = standard error. *p<0.05, **p<0.01 using ANOVA followed by Dunnett post-hoc test (comparison to retina).

C. qRT-PCR quantification of relative mRNA of MICU proteins (relative to reference gene *Ef1α* and/or *b2m*, see methods) across retina, heart, and brain tissues. The mean is reported and bars = standard error. *p<0.05, **p<0.01, ***p<0.001 and ns = not significant using ANOVA followed by Dunnett post-hoc test (comparison to retina).

D. Mitochondria-enriched retinal lysate of WT and pde6c$^{-/-}$ cone deficient retinas. Each lane is from lysate of two pooled retinas from a single fish. The right panel shows quantification of replicates; n=4 fish. Each lane contains 30 µg of protein. The mean is reported and bars = standard error. Ns = not significant using Welch's t-test.

E. Relative quantification of the ratio of MCU to mitochondrial proteins MTCO1 and SDH in WT and pde6c$^{-/-}$ cone deficient retinas from experiments in D. The mean is reported and bars = standard error. *p<0.05, **p<0.01 using Welch's t-test.

Overexpression of MCU in cones raises basal [Ca^{2+}] in the mitochondrial matrix

We hypothesized that low expression of MCU in cones could be protective and sought to identify the consequences of increasing mitochondrial Ca^{2+} content. We established a stable transgenic line that uses MCU-T2A-RFP under control of the promoter for cone transducin ("*gnat2"* or "TαCP") to overexpress zebrafish MCU in cones (**Figure 2.2A**). Because of the T2A sequence, cones overexpressing MCU (MCU OE) also express cytosolic RFP.[85] MCU expression in MCU OE retinas is 102 ± 5 -fold higher than normal (**Figure 2.2B,C**). The overexpressed MCU localizes to cone mitochondria (**Figure 2.2D**).

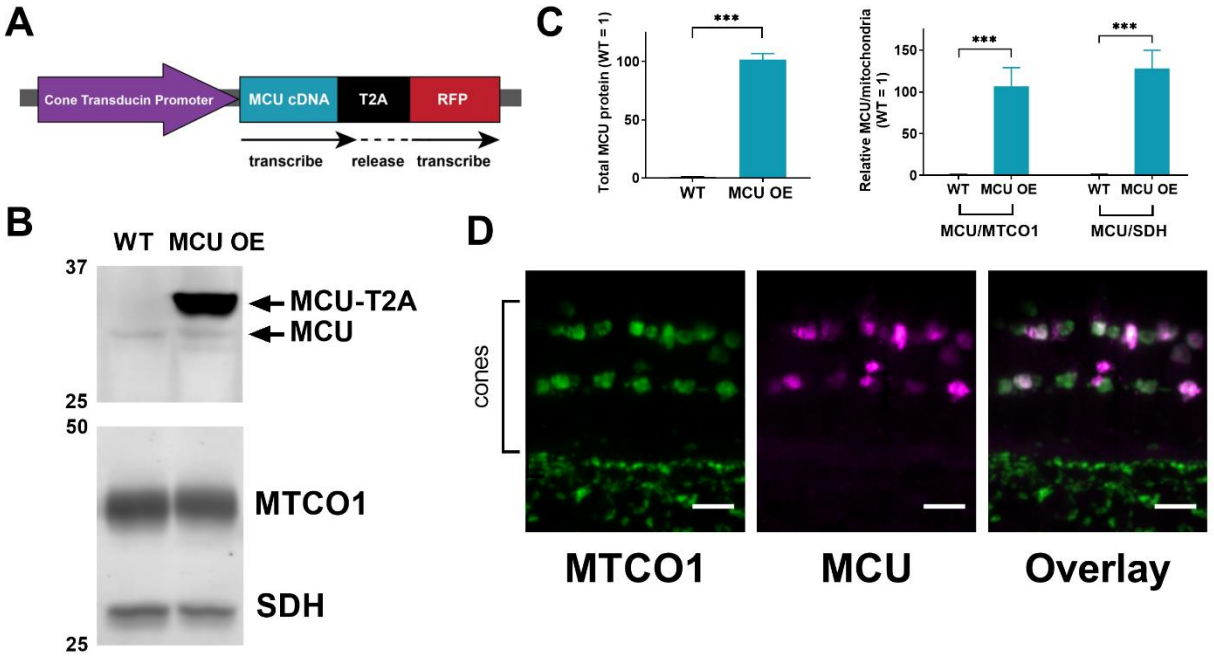

Figure 2.2: Generation of a cone-specific mcu overexpression zebrafish model

A. Schematic of the MCU OE construct. The cone transducin promoter (TαCP, *gnat2*) drives expression of zebrafish MCU cDNA in all cone subtypes. The MCU cDNA is tagged with a T2A sequence followed by RFP. The T2A sequence causes ribosomes to stall and release the nascent MCU polypeptide with some added peptides from the T2A sequence before translating the RFP separately. Thus, RFP is present in the cytosol of cones with MCU overexpression.

B. Mitochondria-enriched retinal lysate of WT and MCU OE retinas probed with antibodies for MCU, MTCO1, and SDH. Each lane contains 8 µg of protein from lysate of two pooled retinas from a single fish.

C. Quantification of relative MCU signal as a function of protein concentration and relative to other mitochondrial markers from the type of analysis shown in B (n = 4 fish). Both exogenous and endogenous MCU were used for total MCU quantification in the MCU OE retina. The mean is reported and bars = standard error. ***p<0.001 using Welch's t-test.

D. Immunohistochemistry of a larval zebrafish retina expressing the MCU construct in A using MCU and mitochondrial cytochrome oxidase (MTCO1) antibodies. Scale bar = 5 µm.

Ca^{2+} influx depends on MCU and its regulators, so we investigated whether MCU overexpression alone increases the steady-state concentration of free Ca^{2+} in cone mitochondria. We used *gnat2*:mito-GCaMP3 fish, which express the Ca^{2+} sensor GCaMP3 in cone mitochondria.[79] Mito-GCaMP3 fluorescence in the mitochondrial clusters of live zebrafish larvae is 4.4 fold higher (median, Q1: 3.4, Q3: 6.06 fold) in MCU OE compared to wild-type (WT) siblings (**Figure 2.3A**). We next prepared *ex vivo* retinal slices of adult *gnat2*:mito-GCaMP3 zebrafish, measuring the baseline mito-GCaMP3 fluorescence (F_0), the maximum fluorescence (F_{max}) by addition of ionomycin to the media containing 2 mM Ca^{2+}, and the minimum fluorescence (F_{min}) by addition of 5 mM EGTA to chelate Ca^{2+} (**Figure 2.3B**). Comparing (F_0 - F_{min}) to (F_{max} - F_{min}) indicated that baseline GCaMP3 is at 20 ± 1% of maximum fluorescence in WT mitochondria and 48 ± 2% of maximum in MCU OE mitochondria. Using these measurements and a K_D of 345 nM for the binding of Ca^{2+} to GCaMP3,[86] the baseline free $[Ca^{2+}]_{mito}$ in WT mitochondria is 80.0 nM (median; Q1: 67.1, Q3: 110.5 nM) and in MCU OE mitochondria is 320.6 nM (median; Q1: 223.9, Q3: 509.0 nM) (**Figure 2.3C**).

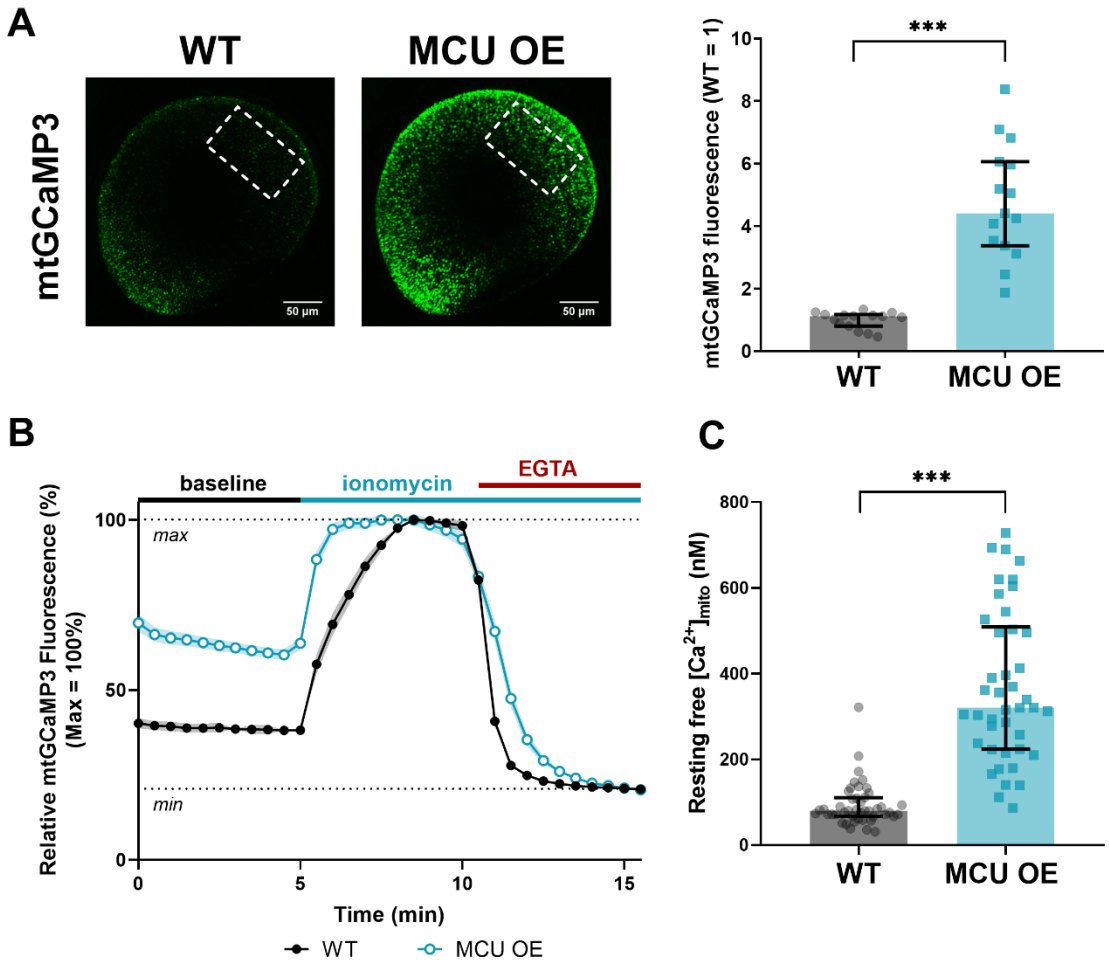

Figure 2.3: Overexpression of MCU in cones raises basal $[Ca^{2+}]$ in the mitochondrial matrix

Full legend on following page.

A. Total cone mitochondria clusters in a larval zebrafish eye expressing *gnat2*:mtGCaMP3, a mitochondrial Ca^{2+} sensor (green). Dotted outlines demarcate the region of the eye used for fluorescence quantification. The median is reported with bars = interquartile range, n=15 larvae for both WT and MCU OE. ***p<0.001 using Mann-Whitney test.

B. Relative mito-GCaMP3 fluorescence of cone mitochondrial clusters in adult retinal slices of *gnat2:*mtGCaMP3 fish (WT or MCU OE) collected between 3 and 4 months of age. Baseline fluorescence was first assayed in the presence of KRB buffer containing 2 mM $CaCl_2$, then ionomycin (5 µM) was added to the slice to allow 2 mM Ca^{2+} entry into the mitochondria to saturate the probe. Next, EGTA (5 mM) was added to the solution (keeping [ionomycin] constant) to chelate Ca^{2+} and establish the minimum GCaMP3 fluorescence signal. n= 45 mitochondrial clusters (3 fish) for WT and n=42 mitochondrial clusters (3 fish) for MCU OE. Slices were imaged every 30 seconds. The mean is reported and shaded region = standard error.

C. Approximation of resting free [Ca^{2+}] in mitochondria clusters assayed in B using the equation $[Ca^{2+}] = K_D \times \frac{\theta}{1-\theta}$, where $\theta = \frac{F_0 - F_{min}}{F_{max} - F_{min}}$. We used the previously reported K_D of GCaMP3 (345 nM, from ref 23) as an approximation for our calculation. Reporting the median with bars = interquartile range and ***p<0.001 using Mann-Whitney test.

Cones overexpressing MCU survive through early adulthood despite changes to mitochondrial morphology

Mitochondria respond to excessive matrix Ca^{2+} by swelling, losing optical/electron density, and potentially opening the mitochondrial permeability transition pore that can trigger cell death.[2,87,88] Abnormal mitochondria are also observed in animal models of elevated $[Ca^{2+}]_{mito}$.[89,90] By just 120 hours of age, MCU OE cones contain many large, swollen mitochondria that have lost significant cristae and electron density, but otherwise appear normal and survive (**Figure 2.4A,B**). As MCU OE fish age, cones maintain a mix of both healthy and swollen mitochondria (**Figure 2,4C**). This heterogeneity is consistent with reports of differential swelling and permeability across a population of mitochondria in response to Ca^{2+}.[87,91,92]

We next assessed long-term survival of MCU OE cones. By visualizing cones with *gnat2*:GFP expression (**Figure 2.4D**), analyzing histology with Richardson's stain (**Figure 2.4E**), and quantifying double-cone nuclei (**Figure 2.4F**) we found that MCU OE cones are preserved at 3 months and 6 months of age. Throughout this period, cones maintain a heterogenous population of normal and swollen mitochondria. By 10 months severe cone loss occurs. Rods remain intact and abundant even after cone loss (**Figure 2.4E, black arrow**). The remaining cones in 10 month MCU OE retinas no longer have large swollen mitochondria but instead have severely fragmented mitochondria (**Figure 2.4G**), which are associated with apoptosis.[93–95]

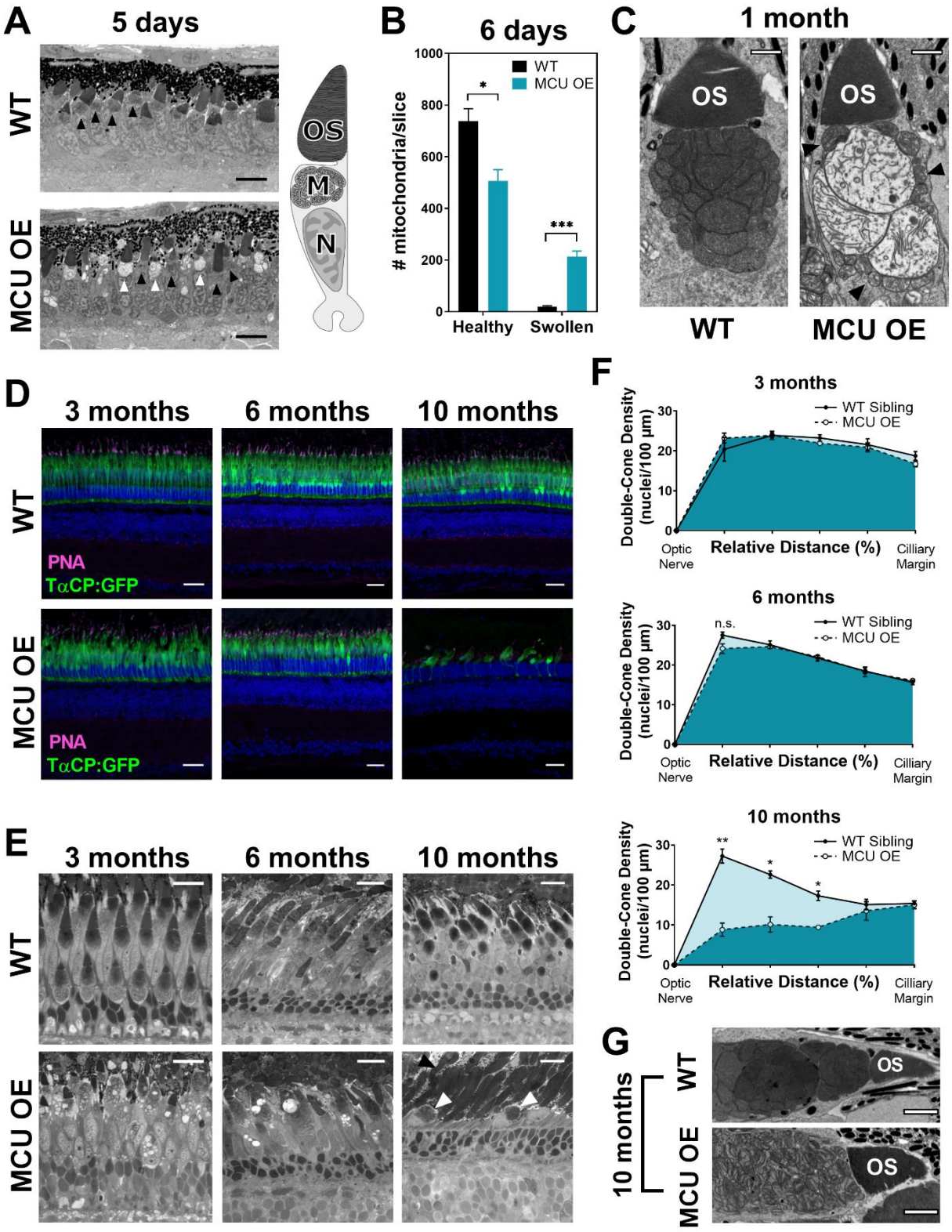

Figure 2.4: Cones overexpressing MCU survive through early adulthood despite mitochondrial abnormalities, but eventually degenerate.

A. Electron micrograph (EM) of MCU cones at 120 hours (5 days) of age. MCU OE cone mitochondria are very heterogenous; some are healthy with dense cristae (black arrow) and others are swollen with little cristae density (white arrow). Scale bar = 5 µm. Right: a schematic of a cone cell with the outer segment (OS), mitochondria (M) in the ellipsoid region, and nucleus (N) labelled.

B. Quantification of cone mitochondrial phenotypes from EM images of whole zebrafish larval eyes (single slice at optic nerve) at 6 days of age. n=3 larvae for both WT and MCU OE fish. The mean is reported and bars = standard error. *p<0.05, ***p<0.001 using a t-test with the Holm-Sidak correction for multiple tests.

C. EM images of cone mitochondria in WT sibling and MCU OE fish at 1 month of age. Mitochondria remain heterogenous in MCU OE cones as they age, with cones containing a mix of healthy mitochondria (black arrows) and swollen mitochondria. Scale bar = 1 µm.

D. WT sibling and MCU OE retinas stained with Hoescht (blue) and exhibiting fluorescence from *gnat2*:GFP in all cone types (green) at 3 months, 6 months, and 10 months of age. Cone outer segments are labelled with α-PNA (magenta). Scale bar = 25 µm.

E. WT sibling and MCU OE retinas stained with Richardson's stain at 3 months, 6 months, and 10 months of age. Swollen mitochondria are still observed in 3 month and 6 month cones. By 10 months, the cones are very few and have severe morphological disturbances (white arrow); however, rod mitochondria and outer segments remain intact (black arrow). Scale bar = 25 µm.

Retinas with MCU overexpressing cones have increased isocitrate dehydrogenase and α-ketoglutarate dehydrogenase activity

The remarkable survival of MCU OE cones allowed us to determine how altered mitochondrial [Ca^{2+}] and structure affect cone metabolism prior to degeneration. Zebrafish retinas are cone-dominant; we found cones comprise ~40% of the mitochondrial mass in a zebrafish retina (**Figure 2.1D**, MTCO1 and SDH in cone-deficient retinas are present at 56 ± 4% and 58 ± 5% of WT levels, n = 4). Thus, analysis of whole retinas provides valuable information regarding changes to mitochondrial metabolism in cones.

In vitro studies have shown that Ca^{2+} lowers the K_m of isocitrate dehydrogenase (IDH) and α-ketoglutarate dehydrogenase (α-KGDH) for their substrates.[35,96] We sought to determine if MCU OE in cones alters the activities of these enzymes. Cones rely on glucose as a fuel, so we incubated 4-month old WT and MCU OE retinas in U-^{13}C-glucose and used gas chromatography-mass spectrometry (GC-MS) to quantify ^{13}C-labeled TCA cycle metabolites **(Figure 2.5A)**.

Steady-state levels of m2 citrate and m2 isocitrate are lower in MCU OE retinas (**Figure 2.5B**). m2 α-ketoglutarate levels are unchanged, while m2 succinate, m2 fumarate, m2 malate, and m2 aspartate are higher in MCU OE retinas. This is consistent with both IDH and α-KGDH being stimulated by Ca^{2+}. Ca^{2+} stimulation of IDH lowers its K_m for isocitrate, meaning it is more active at lower concentrations and able to deplete isocitrate pools. Increased IDH activity in isolation would cause m2 α-ketoglutarate accumulation, but instead we observe similar steady-state levels of m2 α-ketoglutarate in MCU OE and WT retinas and accumulation of metabolites only downstream of α-KGDH. This suggests that MCU OE retinas also have enhanced α-KGDH activity, preventing the buildup of α-ketoglutarate and increasing production of downstream metabolites. This shift in steady-state levels is also reflected in the total (sum of unlabeled and

all isotopomers) metabolite levels **(Figure 2.6G)**. Additional metabolite data showing unaltered glycolytic activity in MCU OE retinas, full isotopomer distribution at the 30-minute time point, and isotopic enrichment is also included **(Figures 2.6A, B, D, E)**.

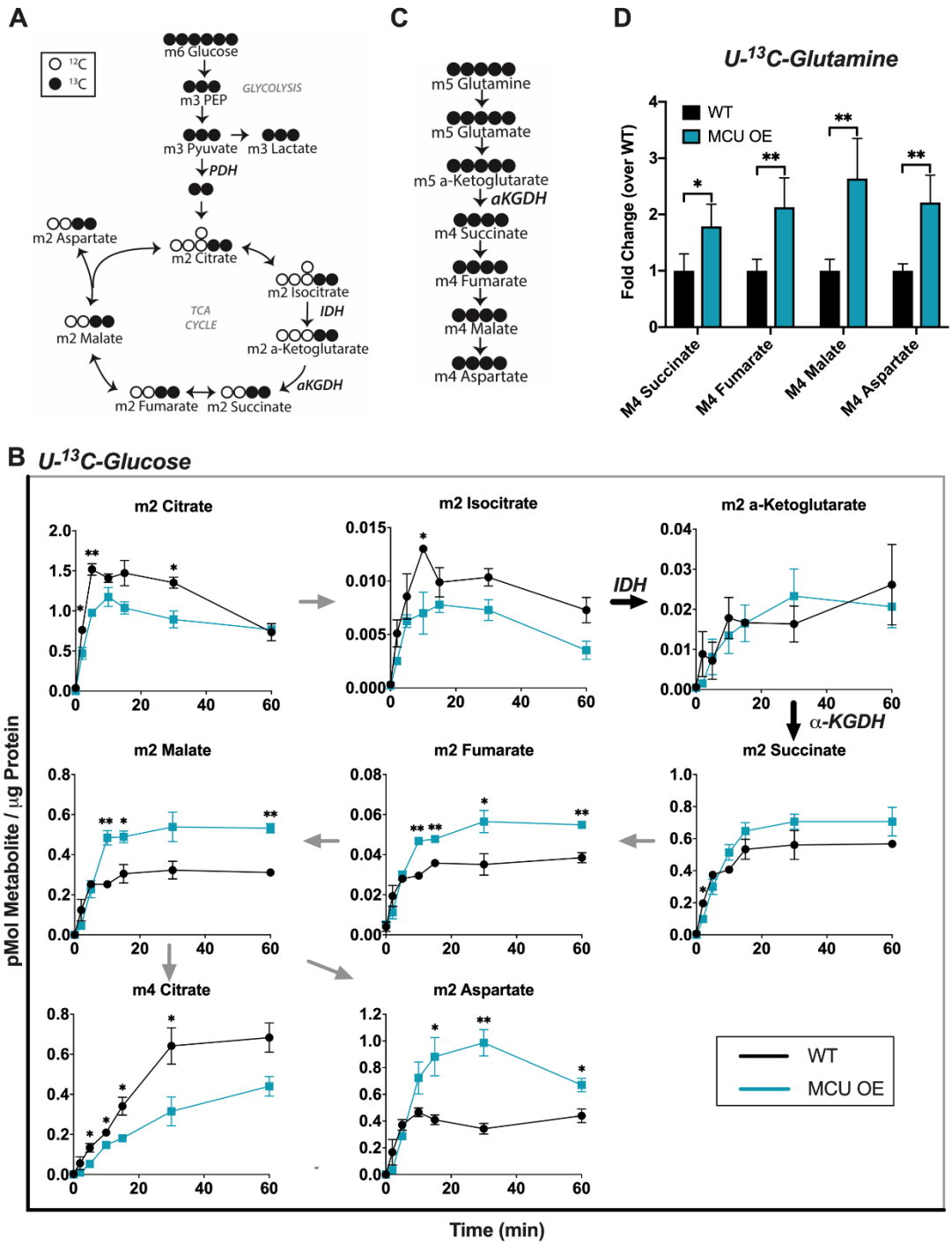

Figure 2.5: MCU OE cones have increased IDH and α-KGDH activity.

Full legend on following page.

A. Diagram showing how labelled carbons from U-^{13}C-glucose are incorporated through glycolysis and the first round of the TCA cycle. Shaded = labeled carbon, empty = unlabeled carbon.

B. Levels of isotopomers in WT and MCU OE retinas supplied with U-^{13}C-glucose. 'm' signifies the number of ^{13}C-labeled carbons in each metabolite. 'm2' TCA cycle metabolites are made from one round of the TCA cycle. Data points represent averages from n=3 retinas from 3 different fish. Fish were 4 months of age. *p<0.05, **p<0.01 using Welch's t-test. Bars = standard error.

C. Diagram showing how labelled carbons from U-^{13}C-glutamine are incorporated into α-ketoglutarate and downstream metabolites. Shaded = labeled carbon, empty = unlabeled carbon.

D. Levels of isotopomers in WT and MCU retinas supplied with 2 mM ^{13}C-glutamine for 15 minutes. Data points represent averages from n=3 retinas from 3 different fish. Fish were 4 months of age. *p<0.05, **p<0.01 using Welch's t-test. Bars = standard error.

Glucose is a physiologically relevant fuel for photoreceptors, but it does not allow for IDH and α-KGDH activity to be observed in isolation because the two are intrinsically linked in the TCA cycle. To confirm that α-KGDH is stimulated by Ca^{2+} in MCU OE cones, we bypassed IDH and fueled α-KGDH directly with U-^{13}C-glutamine **(Figure 2.5C)**. MCU OE retinas fueled with U-^{13}C-glutamine accumulate higher levels of metabolites downstream of α-KGDH **(Figure 2.5D,** glutamine titration in **Figure 2.6F**). These observations confirm that Ca^{2+} enhances α-KGDH activity in zebrafish cones.

It has been reported both *in vitro* and *in vivo* that Ca^{2+} can boost PDH activity by stimulating PDP1c, a subunit of the phosphatase that converts inactive phosphorylated PDH to active unphosphorylated PDH.[35,97] We hypothesized MCU OE cones would have a lower ratio of phosphorylated/total PDH due to increased mitochondrial Ca^{2+}, but instead it is slightly increased (1.12 ± 0.04-fold higher in MCU OE, $p < 0.05$ using Welch's t-test) **(Figure 2.6C)**.

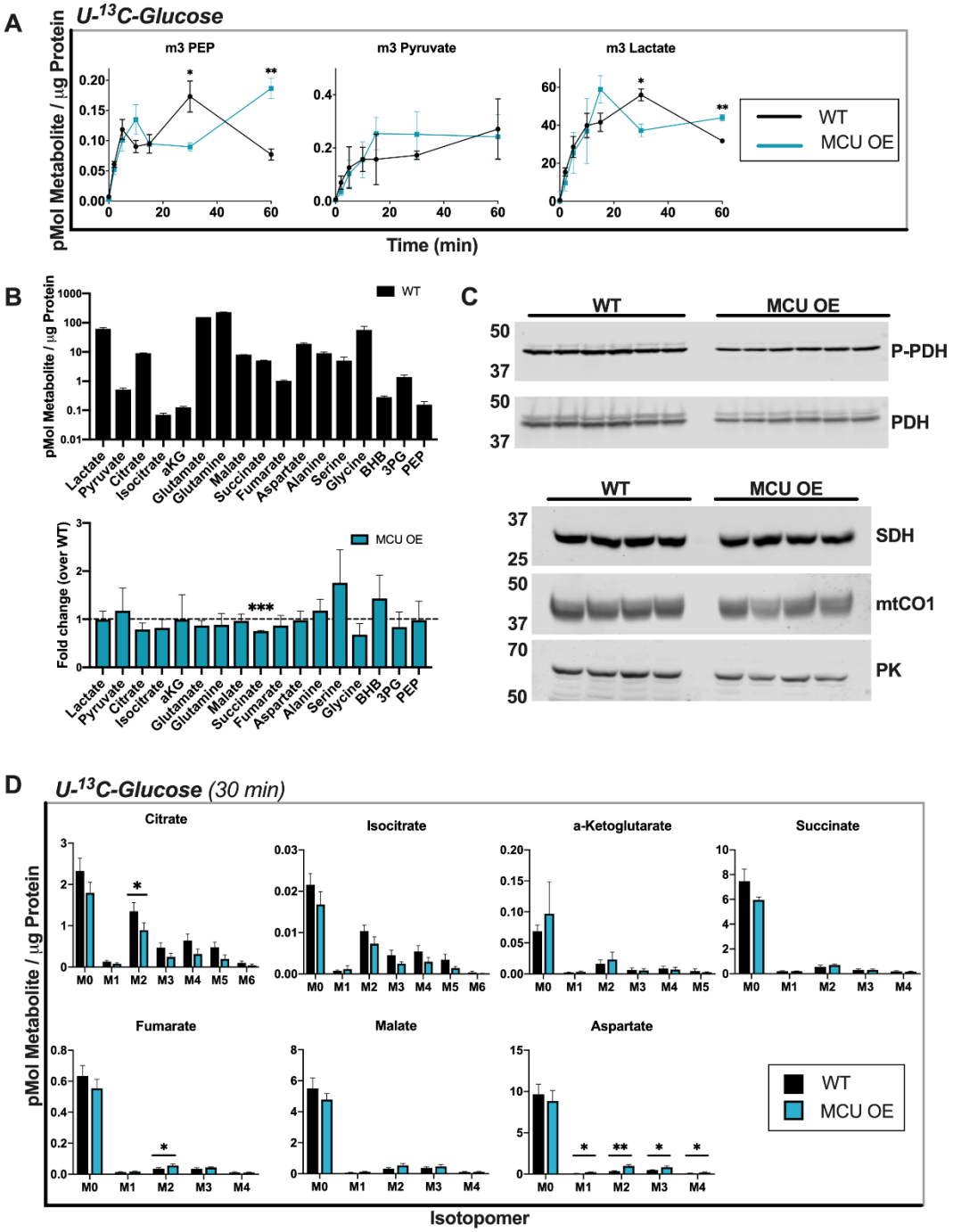

Figure 2.6: Further metabolic characterization of MCU OE retinas.

A. Glycolytic intermediates from 4-month-old WT and MCU OE retinas supplied with ^{13}C-glucose. We observed no trends of altered glycolytic flux over time between WT and MCU OE retinas. *p<0.05, **p<0.01 using Welch's t-test.

B. Total metabolite levels in freshly dissected 4-month-old WT zebrafish retinas and relative levels of these metabolites in MCU OE retinas. (BHB: β-hydroxybutyrate, 3PG: 3-phosphoglycerate, PEP: phosphoenolpyruvate).

C. Top: Immunoblot showing P-PDH and total PDH expression in WT and MCU OE retinas. n=6 WT and 6 MCU OE retinas from 3 different fish. The P-PDH/PDH ratio is 1.12 ± 0.04-fold higher in MCU OE retinas, p<0.05 using Welch's t-test. Bottom: Immunoblot of MTCO1, SDH, and Pyruvate Kinase (PK) in WT and MCU OE retinas. We observed that expression of every protein we probed for (PDH, SDH, mtCO1 and pyruvate kinase) was slightly lower in MCU OE retinas, even when the same amount of protein lysate was loaded. We hypothesize that this is because in MCU OE retinas, MCU and RFP comprise a much larger fraction of the total protein, so other proteins appear less abundant when normalizing to total protein. n=4 WT and 4 MCU OE retinas from 4 different fish.

D. Distribution of isotopomers in 4-month-old WT and MCU OE retinas fed with U-^{13}C-Glucose for 30 min.

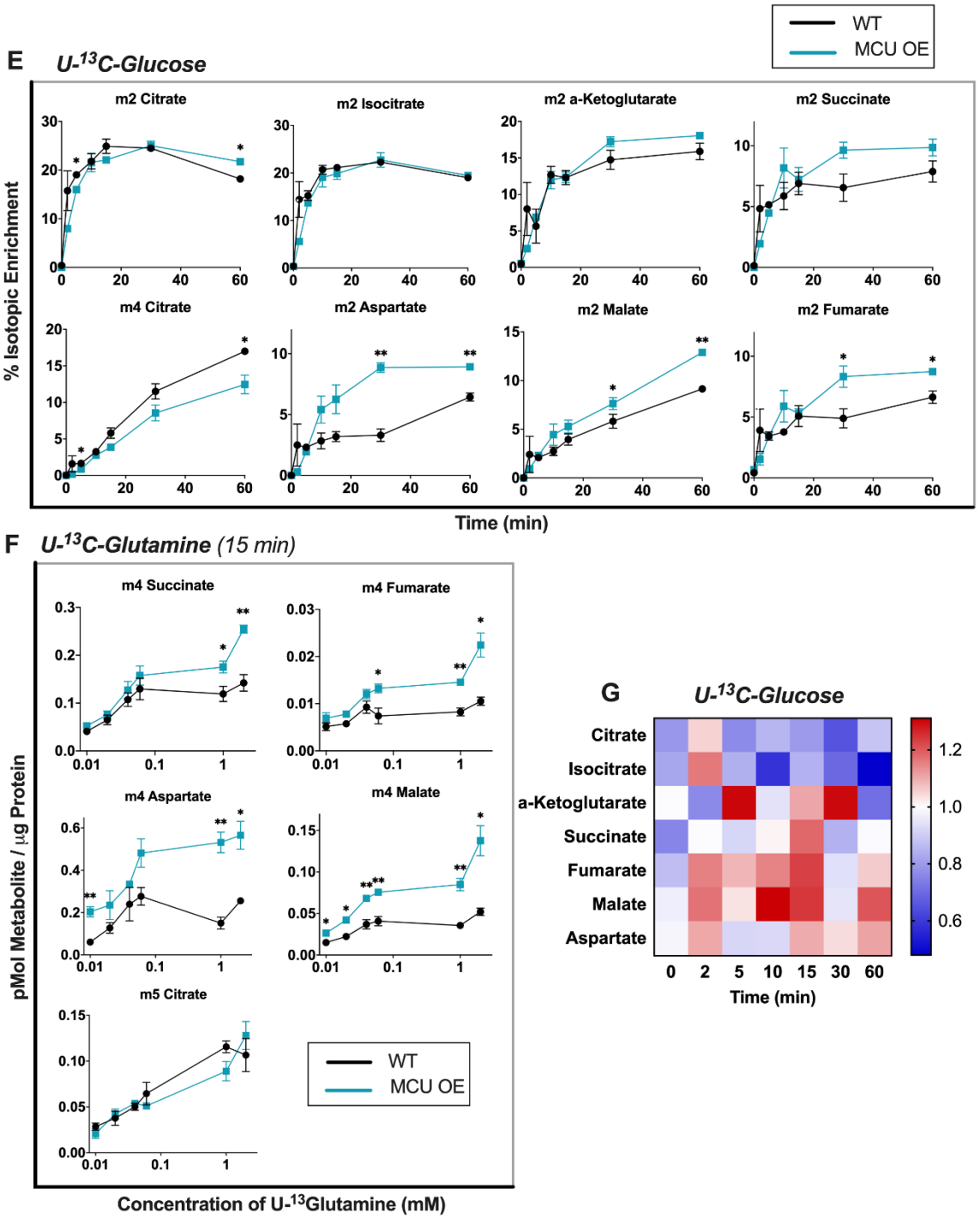

Figure 2.6: Further metabolic characterization of MCU OE retinas.

E. Isotopic enrichment (µg isotopomer/µg total metabolite) of 4-month-old WT and MCU OE retinas supplied with U-^{13}C-Glucose. Since total citrate and isocitrate pools are depleted (see supplemental figure 5G), isotopic enrichment of m2 citrate and m2 isocitrate appear unchanged in MCU OE retinas.

F. Titration of 4-month-old WT and MCU OE retinas supplied with ^{13}C-glutamine (0.1, 0.2, 0.4, 0.6, 1, and 2 mM) for 15 minutes. m5 citrate (produced from reductive carboxylation) is included to show that only metabolites directly downstream of α-KGDH are produced at higher levels in MCU OE cones. Data points represent averages from n=3 retinas from 3 different fish. *p<0.05, **p<0.01 using Welch's t-test.

G. Heat map showing altered distribution of total levels of TCA cycle metabolite in MCU OE retinas fed with U-^{13}C-Glucose (relative to WT). At most time points, total levels of citrate and isocitrate are decreased in MCU OE retinas, while total levels of metabolites downstream of α-KGDH are increased.

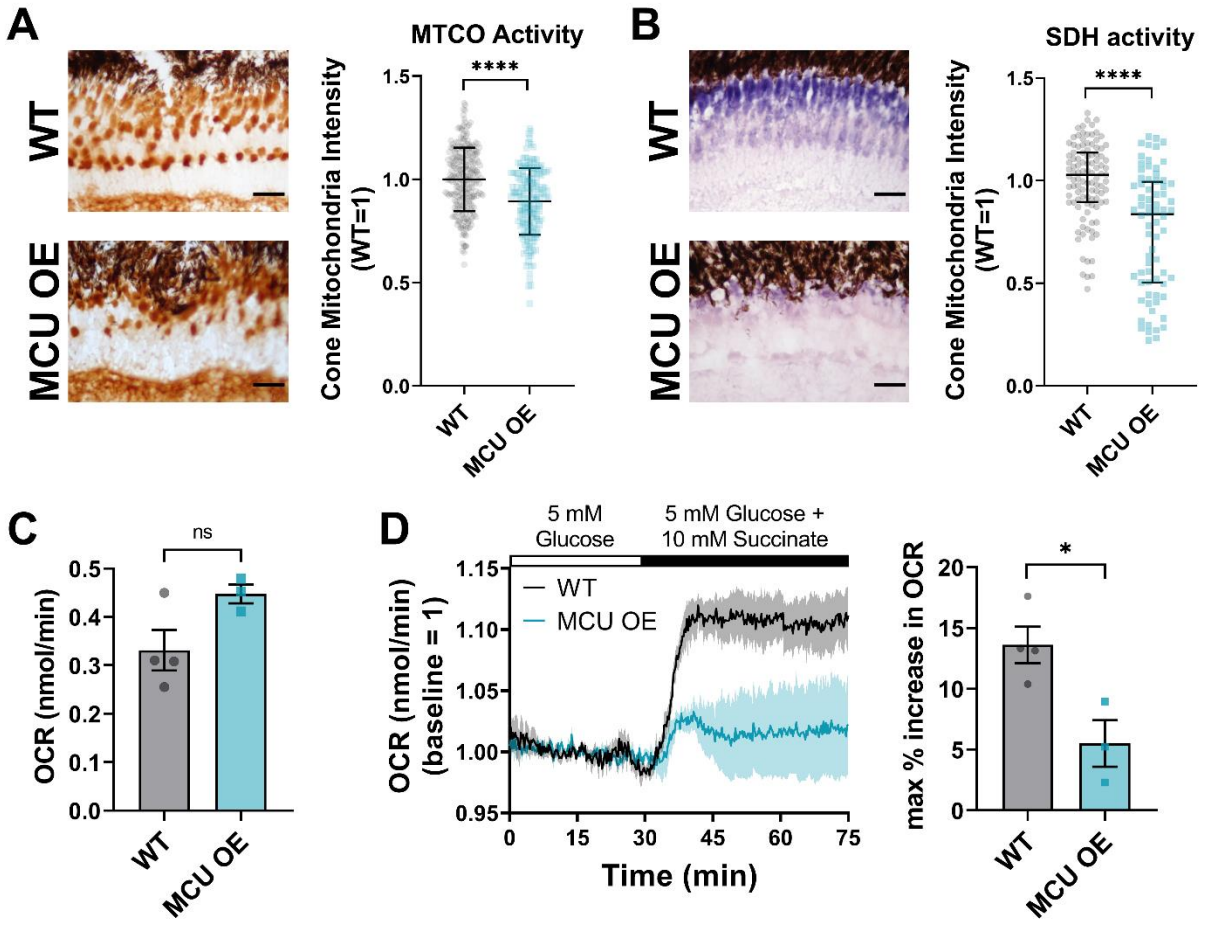

Figure 2.7: SDH activity is compromised in cones overexpressing MCU.

A. Enzyme histochemistry of cytochrome oxidase (MTCO) activity in retinas from 3 month old fish. Maximal capacity for MTCO activity was slightly but significantly decreased in MCU OE cone mitochondria. Scale bar, black = 25 um. Mitochondria (n=249 WT, 178 MCU OE) were sampled from 3 retinas each condition.The mean is reported with bars = standard deviation. ****p<0.0001 using Welch's t-test.

B. Enzyme histochemistry of succinate dehydrogenase (SDH) activity in retinas from 3 month old fish. Maximal capacity for SDH activity was decreased in MCU OE cone mitochondria. Scale bar, black = 25 um. Mitochondria (n=105 WT, 72 MCU OE) were sampled from 3 retinas each condition. Normality tests were not passed, so median is reported with bars = IQ range. ****p<0.0001 using Mann-Whitney test.

C. Oxygen consumption rate (OCR) of retinas in the presence of 5 mM glucose alone. Datapoints represent OCR values in separate chambers, with 6 pooled retinas in each. The mean is reported with bars = standard error. Difference was not significant using Welch's t-test.

D. Left: Increase in oxygen consumption rate (OCR) of retinas supplied with 10 mM succinate + 5 mM glucose after equilibrating in glucose alone for 30 min. Traces are compiled from n=4 chambers for WT and n=3 chambers for MCU OE. 6 pooled retinas were in each chamber. The mean is reported with shaded area = standard error. Right: The maximum recorded percentage increase from baseline is reported for each chamber. Mean reported, error bars = standard error. *p<0.05 using Welch's t-test.

To assess metabolic function specifically in cone cells, we examined the activity of the respiratory chain complexes MTCO and SDH in MCU OE cone mitochondrial clusters using enzyme histochemistry. These assays supply exogenous substrate, and most directly reflect the maximal capacity of enzymatic activity. MTCO activity is compromised in MCU OE cones, with mitochondria on average exhibiting 89.4 ± 1.2% of WT activity (**Figure 2.7A**). We saw a larger reduction in SDH activity (75.4 ± 3.4% of WT activity, Figure 2.7B). Despite this, we did not see a reduction in the basal oxygen consumption of MCU OE retinas, and instead observed a non-significant trend to higher basal oxygen consumption (p=0.075, **Figure 2.7C**). Because supplementation with labelled glucose did not indicate compromised SDH activity, we instead measured changes in oxygen consumption when exogenous succinate was supplied to MCU OE retinas. In WT retinas, a 13.6 ± 1.5% increase in oxygen consumption occurs when retinas are supplied succinate in the presence of glucose (**Figure 2.7D**). MCU OE retinas have a smaller response to succinate, with only a 5.5 ± 1.9% increase in oxygen consumption.

Overexpression of MCU in cones reduces cytosolic Ca^{2+} transients and alters their phototransduction kinetics

Cytosolic Ca^{2+} signals are critical for cone function, so we tested if MCU OE cones could clear cytosolic Ca^{2+} transients faster than in their WT counterparts. We pre-incubated retinal slices from *gnat2*:GCaMP3 fish in a 0 mM Ca^{2+} solution, then introduced a bolus of 5 mM $CaCl_2$ and monitored clearance of cytosolic Ca^{2+} from the cell body (**Figure 2.8A**). MCU OE cones clear Ca^{2+} from the cell body cytosol 2.3 ± 0.1 times faster than their WT siblings, as determined by the decay constant of a single exponential fit (**Figure 2.8B, 2.9A**). The peak fold change in cone cell body GCaMP3 fluorescence in response to the Ca^{2+} bolus is lower in MCU OE cones (**Figure 2.8C**). To determine whether these changes were due to Ca^{2+} uptake via MCU, we incubated MCU OE retinal slices in the MCU inhibitor Ru360. Ru360 treatment partially but significantly restores the WT kinetics (**Figure 2.8A-C**). The incompleteness of the effect may be attributed to other buffering mechanisms affected by MCU overexpression (such as the ER), insufficient permeability of Ru360 into cells, or an abundance of MICU1 which can block Ru360 binding to MCU.[98]

Cytosolic Ca^{2+} in photoreceptor outer segments regulates the gain of phototransduction, light response recovery kinetics and light adaptation.[99–102] Efficient clearance of Ca^{2+} from the outer segment in response to light is critical for rapid recovery of the photoresponse, so we asked whether overexpressing MCU in cones accelerates recovery prior to cone degeneration.[80] Using an *ex vivo* ERG technique to measure pharmacologically isolated cone photoreceptor responses, we found that the initial phase of photoresponse recovery following light flashes is accelerated by MCU overexpression (**Figure 2.8D**). This is more apparent in the dim flash responses, which have a shorter time to half-maximum in MCU OE retinas (**Figure 2.8E**). At the age tested (7 months) the maximal response amplitude (R_{max}) is somewhat decreased in MCU OE retinas (**Figure 2.9B**). However, the dim flash responses normalized to R_{max} have larger amplitude in MCU cones compared to WT, suggesting an increased gain of phototransduction (**Figure 2.8D** and **Figure 2.9C**). To evaluate this, we determined the amplification constant (A) using a model introduced by Lamb and Pugh.[103] We found a significant increase in A in MCU OE retinas, consistent with increased gain of phototransduction activation reactions **(Figure 2.9D)**.

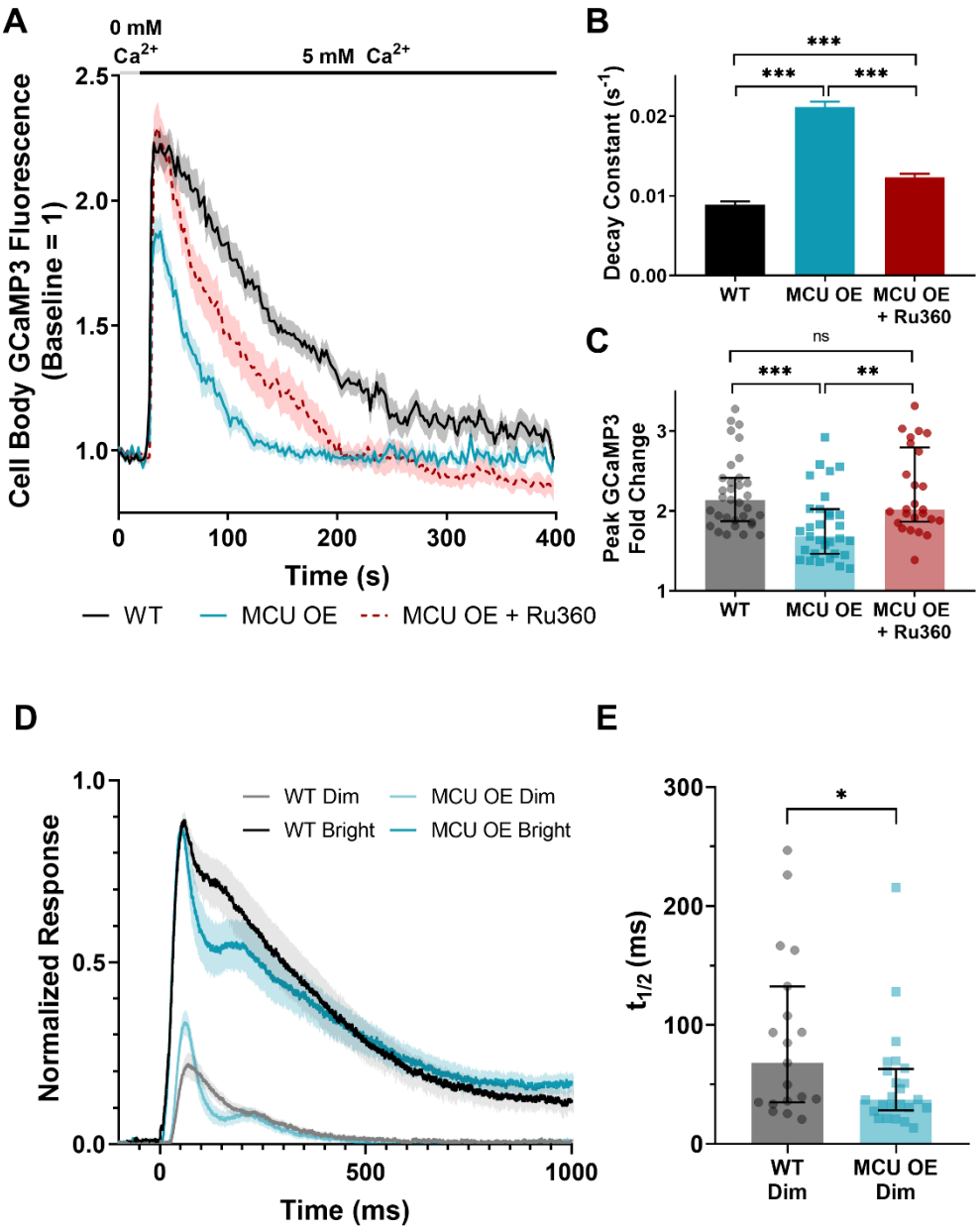

Figure 2.8: Overexpression of MCU reduces cone cytosolic Ca^{2+} transients and alters phototransduction kinetics.

A. Isolated retinas from *gnat2*:GCaMP3 fish pre-incubated in 0 mM Ca^{2+} for 10 min then subjected to a 5 mM Ca^{2+} bolus (black bar). Fish used were WT, MCU OE, or MCU OE retinas preincubated in Ru360 (100 µM) and maintained throughout the experiment. N=33 cells (7 fish) for WT, n=31 cells (7 fish) for MCU OE, n=26 cells (3 fish) for MCU OE + Ru360. Fish were between 3-5 months of age and slices were imaged every 2s. The mean is reported and shaded region = standard error.

B. Decay constant of Ca^{2+} clearance for experiments shown in A. The mean is reported and bars = standard error. ***p<0.001 using ANOVA followed by Tukey post-hoc test.

C. Peak GCaMP3 fluorescence fold-change from baseline for experiments shown in A. The median is reported and bars = interquartile range. WT: median=2.14, Q1=1.87, Q3=2.42. MCU OE: median=1.68, Q1=1.46, Q3=2.02. MCU OE + Ru360: median=2.02, Q1=1.87, Q3=2.80. **p<0.01, ***p<0.001 using Kruskal-Wallis followed by Dunn post-hoc test.

D. The normalized *ex vivo* a-wave response isolated using DL-AP4 (40 µM) and CNQX (40 µM). Each retina response is normalized to R_{max}, the maximum response at the brightest light intensity. Bright flash stimulus intensity is 800,457 photons μm^{-2} and 20ms in duration. N=19 retinas (11 fish) for WT siblings, n=24 retinas (14 fish) for MCU OE. Fish were 7 months of age. The mean is reported and shaded region = standard error.

E. Time to half maximum of the individual responses to a dim stimulus flash from data shown in D. Dim flash stimulus intensity is 2144 photons μm^{-2} and 5ms in duration. The median is reported and bars = interquartile range. WT: median=68.1 s, Q1=34.9, Q3=132.4. MCU OE: median=37.1 s, Q1=28.2, Q3=63.0 *p<0.05 using Mann-Whitney test.

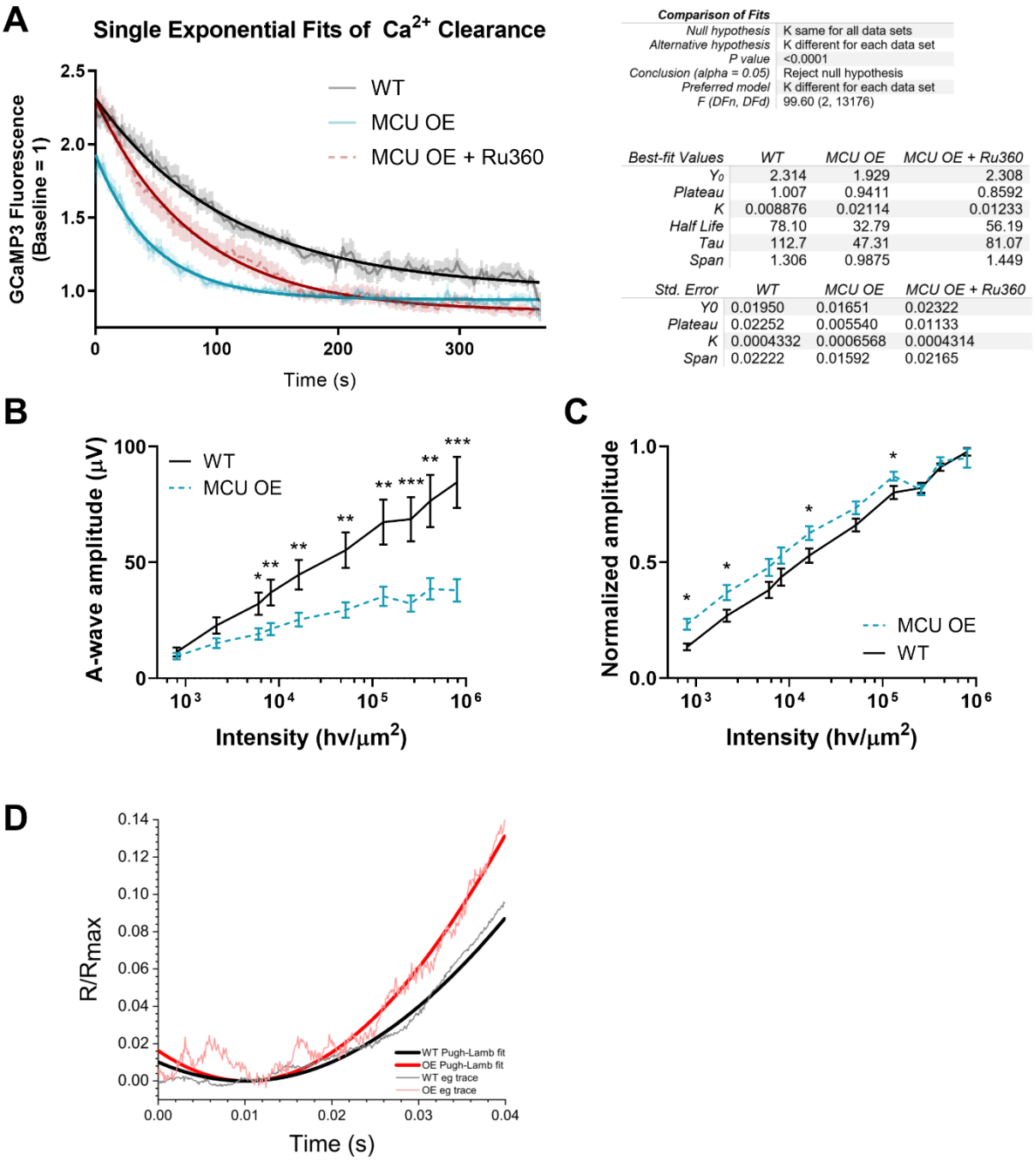

Comparison of Fits	
Null hypothesis	K same for all data sets
Alternative hypothesis	K different for each data set
P value	<0.0001
Conclusion (alpha = 0.05)	Reject null hypothesis
Preferred model	K different for each data set
F (DFn, DFd)	99.60 (2, 13176)

Best-fit Values	WT	MCU OE	MCU OE + Ru360
Y_0	2.314	1.929	2.308
Plateau	1.007	0.9411	0.8592
K	0.008876	0.02114	0.01233
Half Life	78.10	32.79	56.19
Tau	112.7	47.31	81.07
Span	1.306	0.9875	1.449

Std. Error	WT	MCU OE	MCU OE + Ru360
Y0	0.01950	0.01651	0.02322
Plateau	0.02252	0.005540	0.01133
K	0.0004332	0.0006568	0.0004314
Span	0.02222	0.01592	0.02165

Figure 2.9: Fitting of Ca^{2+} clearance data and other ERG parameters.

A. Truncated Ca^{2+} clearance data used for fitting with a one-phase exponential decay function (least squares fit) in GraphPad Prism 8.0.1. The fitted exponentials are shown by a solid, dark line. No constraints were included for Y_0 or the plateau, K > 0. K is different for each data set, with p <0.0001. Descriptive statistics of the fit included in table.

B. Absolute amplitude of the isolated a-wave response to varying intensity light of WT and MCU OE retinas for experiments shown in Figure 4D. Bars = standard error. *p<0.05 using Welch's t-test.

C. Amplitude of a-wave responses in WT and MCU OE retinas normalized to the maximum response for experiments shown in Figure 4D. Bars = standard error. *p<0.05 using Welch's t-test.

D. Lamb-Pugh model fits to ex-vivo ERG dim flash responses normalized to R_{max} of example WT and OE retinas, with original response traces in pale red/grey. WT mean A = 0.0128 $\mu m^2 s^{-2}$ ± 0.0143, n= 16 retinas. MCU OE mean A = 0.18278 $\mu m^2 s^{-2}$ ± 0.0217, n= 23 retinas. *p<0.05 using Welch's t test.

Cones respond to MCU overexpression by decreasing MICU3 expression and selectively transporting abnormal mitochondria away from the ellipsoid

We assessed what adaptations may enable long-term survival of MCU OE cones. We analyzed retinal transcripts of MICU1, MICU2, MICU3a, and MICU3b in 3-month-old retinas and found that MICU3a, reported to be a neuronal-specific enhancer of Ca^{2+} uptake via MCU[53], was significantly lower in MCU OE retinas (**Figure 2.10A**). This would presumably limit Ca^{2+} influx into mitochondria and thereby contribute to cone survival. However, this cannot compensate completely for the MCU overexpression phenotype since we observe swollen mitochondria and increased basal mitochondrial Ca^{2+} at this age and beyond (**Figure 2.3C, Figure 2.4E**).

Cones also respond to MCU overexpression by altering their mitochondrial distribution. Mitochondria normally are confined solely to the ellipsoid region in zebrafish cones, between the nucleus and the outer segment.[104] However, large mitochondrial clusters are present outside of this region in MCU OE retinas (**Figure 2.10B**). We recorded time-lapses of live zebrafish larvae expressing *gnat2*:mito-GCaMP3 and *gnat2*:MCU-T2A-RFP that revealed a slow, directed movement of mitochondrial clusters away from the ellipsoid region toward the synapse (**Figure 2.10C**).

All mitochondria observed outside of the ellipsoid region of MCU OE cones have a swollen phenotype by electron microscopy **(Figure 2.10D)**. Some MCU cones with swollen, mislocalized mitochondria contain mostly normal mitochondria within the ellipsoid (**Figure 2.10E**). 3D reconstructions of MCU OE mitochondria from electron micrographs suggest that movement of abnormal mitochondria away from the ellipsoid region is active, as moving mitochondria deform the nucleus on their way toward the synapse (**Figure 2.10F**).

These observations led us to hypothesize that cones can selectively export damaged mitochondria from the ellipsoid and that Ca^{2+} may stimulate this. If this were true, subjecting MCU OE cones to higher intracellular Ca^{2+} would increase Ca^{2+}-associated mitochondrial stress and mitochondrial movement. Intracellular Ca^{2+} in cones is constitutively elevated in darkness, so we compared MCU OE fish on a normal light cycle to those incubated in complete darkness the day prior to imaging. Dark pre-incubation increases the number of mislocalized mitochondria in *gnat2*:mito-GCaMP3 fish (**Figure 7G**). This is not attributable to changes in probe fluorescence, which was unchanged under imaging conditions (Dark = 103 ± 5% of Light, p=0.653 using Welch's t-test, n=16 fish). Quantification of mislocalized mitochondria in

Richardson's stained sections confirms that darkness exposure increases mitochondrial mislocalization (**Figure 7H**).

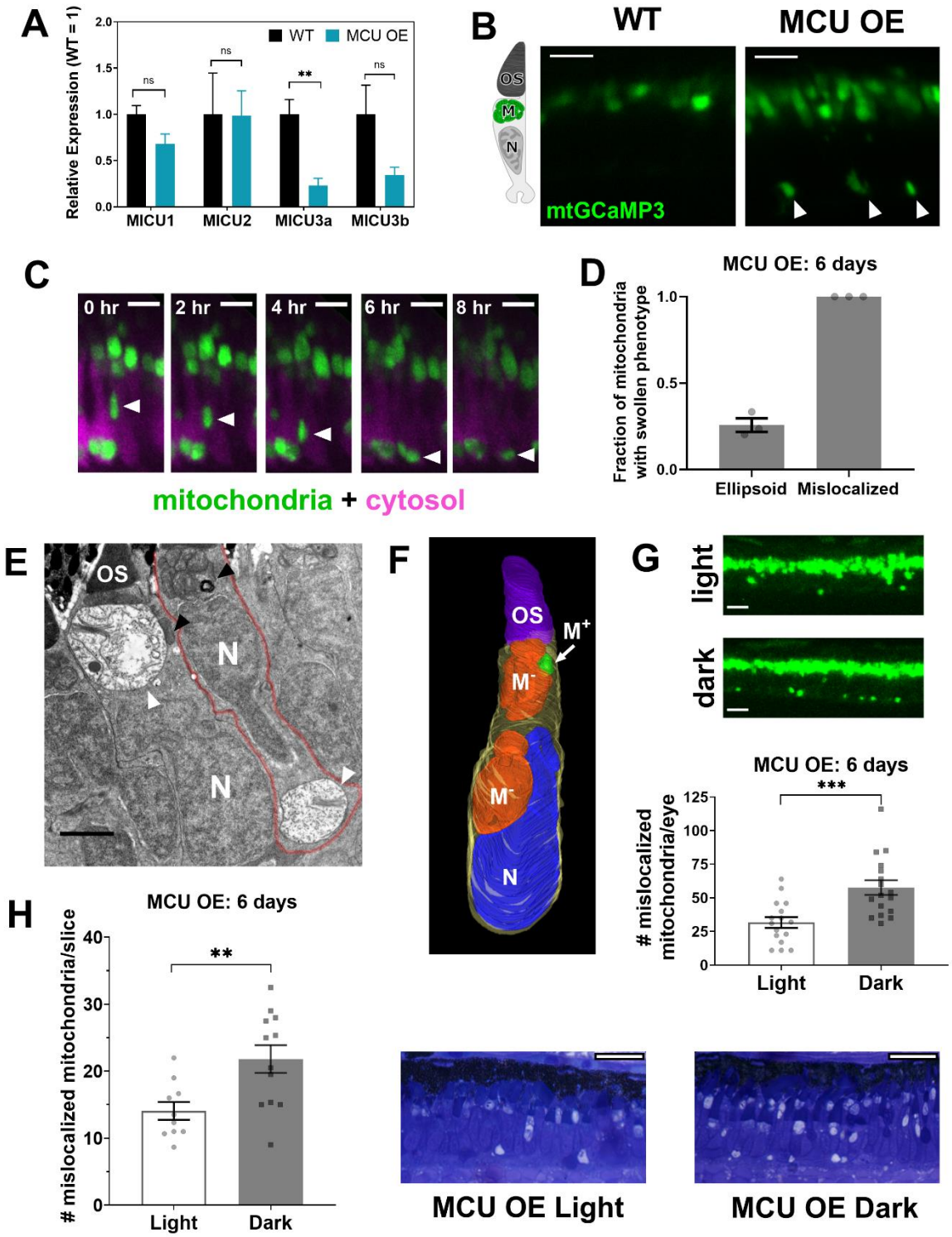

Figure 2.10: Cones respond to MCU overexpression by decreasing MICU3 transcript and selectively transporting abnormal mitochondria away from the ellipsoid.

A. qRT-PCR quantification of relative mRNA of MICU proteins (relative to reference gene *Ef1α*, see methods) between WT and MCU OE retinas at 3 months of age (n=3). The mean is reported and bars = standard error. **p<0.01 and ns = not significant using Welch's t-test.

B. Cone mitochondrial clusters in live larvae expressing *gnat2*:mtGCaMP3. WT mitochondria were imaged with higher laser power to show localization. In MCU OE models, mitochondrial clusters were found near the synapse and nuclear layer (white arrows), which was not observed in WT siblings. Left: cone schematic with OS = outer segment, M = mitochondrial cluster, N = nucleus. Scale bar = 5 µm.

C. 8 hour timelapse of a migrating mitochondrial cluster (green, white arrow) in live MCU OE *gnat2*:mtGCaMP3 larvae. Cone cell bodies express cytosolic RFP (magenta). Scale bar = 5 µm.

D. Quantification of cone mitochondria in WT sibling and MCU OE fish from EM images of whole zebrafish larval eyes (single slice at optic nerve) at 6 days of age. Fraction of swollen mitochondria was determined by counting swollen mitochondria relative to total cone mitochondria either in the ellipsoid or mislocalized. n=3 larvae for both WT and MCU OE fish. The mean is reported and bars = standard error.

E. EM image from MCU OE larvae at 14 days of age. A single cone photoreceptor can contain both healthy mitochondria (black arrows) in the ellipsoid region and swollen mitochondria (white arrows) near the synapse. Cone cell membrane outlined in red overlay to aid visualization. Scale bar = 2 µm. OS = outer segment, N = nucleus.

Discussion

The key findings of this study are 1) MCU is expressed at very low levels in cone photoreceptors, 2) metabolic and physiologic functions of cones are influenced by enhanced mitochondrial Ca^{2+} influx, and 3) cones can adapt to elevated mitochondrial Ca^{2+} and survive this stress for many months. These findings are summarized in **Figure 2.11**.

Our findings challenge the idea that mitochondrial Ca^{2+} overload is a primary driver of photoreceptor degeneration. MCU in cones is normally maintained at low levels, yet cones can robustly survive MCU expressed beyond physiological levels that causes a four-fold increase in basal matrix [Ca^{2+}] and mitochondrial disruption. Their prolonged survival suggests mitochondrial Ca^{2+} overload may not be the cause of rapid photoreceptor degeneration linked to mutations that increase cytosolic [Ca^{2+}]. This is consistent with the finding that cellular Ca^{2+} buffering is not overloaded in zebrafish pde6c mutant cones or rd1 mutant mouse rods.[105] Our findings appear to differ from an *ex vivo* study showing mitochondria-mediated cell death in rods caused by elevated external Ca^{2+}.[81] A possible explanation for these different findings is that our study monitors cell survival within a living organism where the stress is chronic and normal adaptive mechanisms are intact.

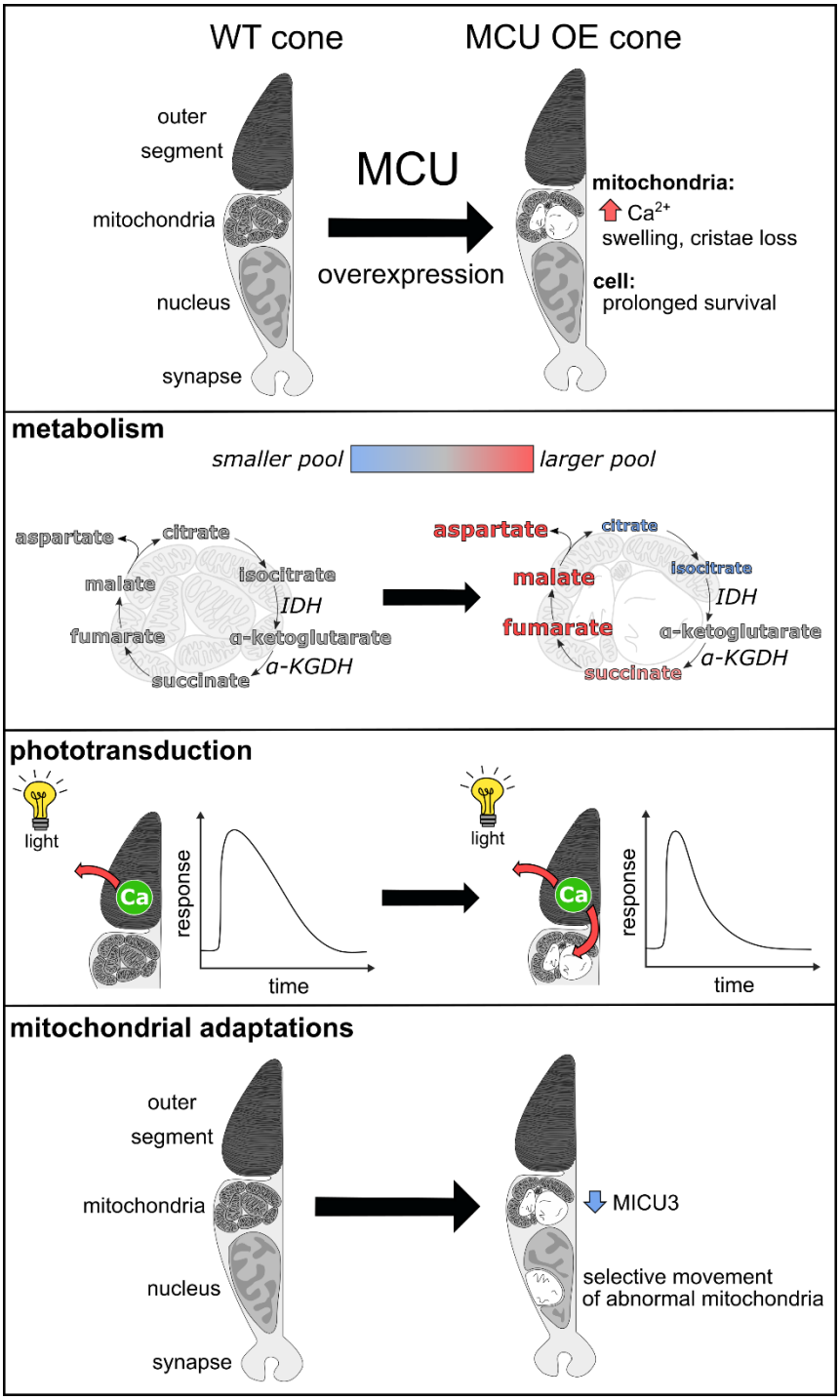

Figure 2.11: Summary of phenotypes in the MCU OE cone model.

Cones, which normally have low MCU expression, experience an increase in mitochondrial matrix Ca^{2+} and mitochondrial swelling when MCU is overexpressed. Cones survive this stress for many months. Mitochondrial metabolite pools are altered consistent with enhanced activity of IDH and α-KGDH. Recovery of the photoreceptor to light stimuli, dependent on Ca^{2+} clearance from the outer segment, is faster when MCU is overexpressed. Cones respond to chronic elevated mitochondrial Ca^{2+} by decreasing transcription of the MCU enhancer MICU3 and selectively moving abnormal mitochondria away from the ellipsoid region of the cell.

Cone adaptations to mitochondrial Ca^{2+} stress

Determining how cones survive chronic mitochondrial Ca^{2+} stress and mitochondrial disruption is key to understanding cone homeostasis and long-term viability. We found that cones respond to elevated mitochondrial Ca^{2+} by decreasing expression of the Ca^{2+} uptake enhancer MICU3 and selectively transporting abnormal mitochondria away from the ellipsoid. Mitochondrial movement away from the ellipsoid could protect cones from mitochondrial Ca^{2+} overload. The ellipsoid is adjacent to the outer segment, which reaches high, sustained levels of Ca^{2+} in darkness. Trafficking of damaged mitochondria may be an important adaptation for long-term survival of normal cones; cones in aging humans contain swollen mitochondria similar to MCU OE mitochondria, and retinal mitolysosomes are highly concentrated in the photoreceptor nuclear layer, away from the ellipsoid.[106,107] We hypothesize that selective mitochondrial movement can occur in normal cones, but is dramatically enhanced by the widespread mitochondrial damage upon MCU overexpression.

Both cytosolic and mitochondrial matrix Ca^{2+} are associated with reduced mitochondrial movement in neurons.[20,108–110] Mitochondrial damage is also associated with cessation of movement.[21,22,111] However, in MCU OE cones damaged mitochondria are selectively trafficked, and higher intracellular Ca^{2+} in darkness enhances this movement. It is possible that acute mitochondrial stress responses differ from chronic stress responses, which have recently been reported to trigger release of the anchoring protein SNPH to induce transport of stressed mitochondria.[23] These disparate observations highlight the need for further investigation of the role of mitochondrial Ca^{2+} content and subsequent stress in mitochondrial movement in neurons.

Mitochondria can alter phototransduction kinetics

Mitochondria can act as a barrier between the Ca^{2+} pools in the outer segment and the rest of the cell.[79] Their proximity to the outer segment raises the possibility that they influence Ca^{2+} in the outer segment, where Ca^{2+} clearance is essential to promote photoresponse recovery and adaptation. Clearance of outer segment Ca^{2+} is thought to be accomplished primarily by plasma membrane Na^+/Ca^{2+}, K^+ exchangers, but cones lacking these can respond to light, light-adapt, and degenerate rather slowly, suggesting that there is an additional pathway that clears Ca^{2+} from cone outer segments.[75,112] Survival of MCU OE cones allowed us to investigate the capacity for mitochondria to influence the photoresponse, and we report that faster clearance of

cytosolic Ca^{2+} is accompanied by accelerated photoresponse recovery. This indicates that mitochondrial Ca^{2+} uptake in photoreceptors can contribute to Ca^{2+} clearance from the outer segment and modulate the kinetics of the photoreceptor response to light. Mitochondria may contribute to normal photorecovery, as delayed rod photorecovery is observed in human patients with malfunctioning mitochondria.[113]

MCU overexpression enhances IDH and α-KGDH activity

The perturbations to mitochondrial structure and localization in MCU OE cones could cause Ca^{2+}-independent changes to mitochondrial metabolism. However, TCA cycle metabolites are not globally decreased and MCU OE retinas have unaltered glycolytic activity, suggesting they are not compensating for decreased mitochondrial metabolic function. Instead of disrupting mitochondrial metabolism, MCU overexpression specifically alters the steady-state levels of TCA cycle metabolites, consistent with enhanced activities of the Ca^{2+}-sensitive enzymes IDH and α-KGDH.

The highest levels of intracellular free Ca^{2+} in photoreceptors occur in darkness, when energy demand and O_2 consumption are greatest. Ca^{2+} could play an important role in stimulating increased TCA cycle activity in photoreceptors in darkness.[73,114] Rod photoreceptors in mouse retinas accumulate higher levels of TCA cycle metabolites downstream of α-KGDH in darkness than in light.[115] Here, we report a similar accumulation of downstream metabolites in MCU OE cones. We also note that enhanced IDH and α-KGDH activities deplete upstream pools of citrate and isocitrate. MCU OE retinas do not increase citrate production in response to a decrease in the steady-state level of citrate, suggesting that TCA cycle activity in cones is limited either by pyruvate entry into mitochondria or by acetyl-CoA production.

An increase in the P-PDH/total PDH ratio is a common metabolic phenotype in MCU KO tissues.[116] However, we did not find evidence for Ca^{2+} stimulation of PDH phosphatase in cones. Since the P-PDH/total PDH ratio also does not decrease when MCU is overexpressed in muscle cells, it is possible that changes in mitochondrial bioenergetics resulting from increased mitochondrial Ca^{2+} feed into the complex regulation of PDH.[62] For example, stimulation of α-KGDH and IDH activity may result in higher NADH levels in MCU OE cones, which in turn stimulates PDH kinase to balance increased PDP1c activity.

The activity of succinate dehydrogenase (SDH) is compromised in MCU OE cones. However, tracing experiments do not show a labelling pattern consistent with decreased SDH activity in

the conversion of glucose-derived succinate to fumarate. Notably, when examining total pools of metabolites (unlabeled), succinate is the only metabolite that is significantly decreased in MCU OE retinas (**Figure 2.6B**). A decrease in succinate levels is not consistent with decreased SDH activity in the forward reaction but is consistent with decreased reverse SDH activity (which would not be detected in the glucose labelling experiment). Recent evidence suggests that the retina is metabolically specialized to favor the reverse mode of SDH (Bisbach et al 2020, accepted at *Cell Reports*), so it is possible that disruption of the mitochondria by MCU overexpression diminishes this activity.

Conclusions and Future Directions

Photoreceptors must maintain viability throughout a lifetime despite chronic stress associated with light damage, ATP demand, O_2 exposure, and Ca^{2+} fluctuations. Our findings show that cone photoreceptors are remarkably tolerant of Ca^{2+}-associated mitochondrial stress, an adaptation that likely promotes their long-term survival. Cones can survive high levels of MCU expression, and while excess protein could potentially cause other secondary effects, we observe specific changes to metabolism and phototransduction kinetics consistent with enhanced mitochondrial Ca^{2+} uptake. Cones respond to elevated mitochondrial Ca^{2+} by selectively trafficking abnormal mitochondria away from their normal position in the ellipsoid and decreasing transcription of the Ca^{2+} uptake enhancer MICU3. The cone MCU OE model can be used in future studies as a tool to examine mitochondrial movement and trafficking in cones and dissect in more detail the adaptive mechanisms that promote survival in response to chronic mitochondrial stress. Furthermore, the distinct localization of mitochondria in zebrafish cones makes the MCU OE model an attractive system to study mechanisms underlying mitochondrial sorting and movement.

Materials and Methods

Zebrafish Maintenance. Experiments with zebrafish were authorized by the University of Washington and University of Utah Institutional Animal Care and Use Committees. All fish used in this analysis were maintained in the University of Washington South Lake Union aquatics facility or the Centralized Zebrafish Animal Resource (CZAR) at the University of Utah at 27.5C on a 14 h/10 h light/dark cycle, and were maintained in the $Roy^{-/-}$ genetic background. All wild-type fish (WT) used in analysis were age-matched siblings to Tg(gnat2:MCU-T2A-RFP) fish (MCU OE) or age-matched siblings to $pde6c^{w59}$ ($pde6c^{-/-}$).[83] Fish used for slice preparation, protein quantification, and metabolomics analysis were male and female siblings between 3 and 6 months of age. Fish used in ERG analysis were male and female siblings collected at 7 months of age. For histological analysis, ages of sibling fish are included in the figure and legend. Formal methods of randomization were not used.

Zebrafish MCU antibody. The cDNA encoding amino acids 21 – 202 of *Danio rerio* MCU (NM_001077325) was cloned downstream of GST using the pGEX-2T (GE) expression vector. Overexpression was induced in *E.coli* (BL21) by addition of 1mM IPTG at 0.2 OD followed by incubation with vigorous shaking for 5h at 37° C. The tiny fraction of soluble fusion was purified using glutathione sepharose following the manufacturer's instructions (GE Healthcare). Polyclonal antibodies were generated using injections of 0.5 – 1mg protein (R and R Research Co.). Two columns were used to clean the serum. One column contained total *E.coli* proteins covalently coupled to cyanogen bromide beads and the second column contained purified GST protein coupled to cyanogen bromide beads (GE Healthcare). Serum was cleaned by sequential incubations of 3 – 5 hours at room temperature with each column after which it was analyzed on an SDS page gel for lack of cross reactivity with GST and *E.coli* proteins from a total cell extract. Identification of MCU was validated by the absence of a protein of the correct molecular weight in extracts obtained from a CRISPR generated KO strain. The zebrafish MCU antibody was used at a dilution of 1:750 for western blotting and 1:50 for immunohistochemistry.

Zebrafish models. The transgenic zebrafish lines Tg(gnat2:GCaMP3), Tg(gnat2:EGFP), and Tg(mito-GCaMP3) have been described previously.[79,105,117] Generation of the global MCU KO line was performed using gRNA with the following sequence 5'-CCTCATACCTGGTGCAGCCCCCC-3' using methods as previously described.[118] For generation of the Tg(*gnat2*:MCU-T2A-RFP) line, zebrafish MCU cDNA was isolated from WT

zebrafish larvae (5 dpf) using the forward primer 5'- AGAGATGGCTGCGAAAAGTGT-3' and reverse primer 5'- TTCTCATCAGTCCTTGCTGGT-3'. Overhang qPCR methods in conjunction with Fast-Cloning were used to add the T2A ribosomal stalling sequence and the RFP protein coding sequence; this was cloned into a pCR8/GW vector (Invitrogen). Plasmids were assembled using the Gateway-Tol2 system.[119] Expression of MCU-T2A-RFP was driven by the cone transducin alpha promoter (TαCP, gnat2), and the RFP coding sequence was flanked by a polyA tail sequence to increase transcript stability.[117] A destination vector with a sBFP2 heart marker for aid in transgenic identification was obtained from Cecilia Moens.[120] The fully assembled construct was injected into embryos at the 1-cell stage with Tol2 transposase mRNA. Larvae mosaic for the transgene were raised to adulthood to identify founder carriers. A single F_0 founder was used to generate F_1 fish that were screened for a single insertion of the transgene; F_2 fish from two F_1 substrains with a single insertion were used for analysis in this study.

Primers for qRT-PCR. All designed primers were empirically tested to confirm primer efficiency was between 90-110%. Only primers passing this benchmark were used for analysis. Primer sequences for the reference genes *EF1a*, *b2m*, *Rpl13a*, and *TBF* were identical to previous reports testing zebrafish reference gene stability (*EF1a*, *Rpl13a*: ref [121], *b2m*, *TBP*: ref [122]).

MICU1: Forward: 5'-ACGTTAAAGCAGAATCGTAGAGG-3' Reverse: 5'-CGCAAGCGGTACATATCAGAC-3'	**MICU3a:** Forward: 5'-CGTCCCATGAGCATCGTTTC-3' Reverse: 5'-TCCAACTCCTGTTTGGTGAGG-3'
MICU2: Forward: 5'-ACTGAGTACCTGTTTCTCCTCAC-3' Reverse: 5'-GGTCCATTTACTTTCTTCAGCTTCT-3'	**MICU3b:** Forward: 5'-GCTTGGTGCAAGAATAGTTCTCTTT-3' Reverse: 5'-TGCAGGTTGTCCATGAATCTGT-3'

qRT-PCR. An Applied Biosystems 7500 Fast Real-Time PCR System in conjunction with iTaq™ Universal SYBR® Green Supermix (Bio-Rad, 1725120) was used for qPCR measurements according to the manufacturer's instructions. The reference genes *EF1a*, *b2m*, *TBF*, and *rpl13a* were screened across the tissue panel using NormFinder to identify reference genes with the highest stability.[123] NormFinder identified the combination of *EF1a* and *b2m* as most stable for retina-brain comparisons and *EF1a* as most stable for retina-heart comparisons. *EF1a* was identified as the most stable for WT vs MCU OE retina comparisons. Quantification of relative

mRNA quantity used 3 biological replicates of each tissue, each performed in technical triplicate. From each technical triplicate, the average C_t value for the gene of interest and reference gene(s) were used to generate a ΔC_t value for each biological replicate. Comparing each tissue of interest to the retina generated a $\Delta\Delta C_t$ value; these were converted to a normalized expression level using the $2^{-\Delta\Delta Ct}$ method (Livak assumptions). Standard error of the ΔC_t value for each tissue was propagated to the final comparison using standard error propagation rules. Calculations were based off the geNorm method of qPCR normalization.[124]

Commercial antibodies and stains.

Mitochondrial cytochrome oxidase, MTCO1 (Abcam, ab14705, RRID:AB_2084810); used in immunohistochemistry (IHC) and immunoblotting at 1:1000 dilution.

Succinate dehydrogenase B, SDHB (Abcam, ab14714, RRID:AB_301432); used in IHC and immunoblotting at 1:1000 dilution.

Pyruvate Dehydrogenase E1 subunit, PDH (Abcam, ab110334, RRID:AB_10866116)**; u**sed in immunoblotting at 1:1000 dilution.

Phosphorylated Pyruvate Dehydrogenase E1 subunit Ser293, P-PDH (EMD Millipore, ABS204, RRID:AB_11205754); used in immunoblotting at 1:2000 dilution.

Pyruvate Kinase, PK (Abcam, ab137791); used in immunoblotting at 1:1000 dilution.

Hoechst 33342, Trihydrochloride, Trihydrate stain (ThermoFischer, H3570); used in IHC at 5 µM concentration.

Lectin PNA Alexa Fluor 647 conjugate (ThermoFischer, L32460); used in IHC at 1:200 dilution after suspending at a concentration of 1 mg/mL in H2O.

Goat Anti-Mouse IgG H&L, Alexa Fluor 488 (Abcam, ab150113, RRID:AB_2576208); used in IHC at 1:1000 dilution.

Goat Anti-Rabbit IgG H&L, Alexa Fluor 647 (Abcam, ab150083, RRID:AB_2714032); used in IHC at 1:1000 dilution.

IRDye 800CW donkey anti-rabbit IgG (H+L) (LI-COR Biosciences, 925-32213, RRID: AB_2715510); used at 1:5000 dilution for immunoblotting.

IRDye 680RD donkey anti-mouse IgG (H+L) (LI-COR Biosciences, 925-32212, RRID: AB_2716622); used at 1:5000 dilution for immunoblotting.

IRDye 680RD donkey anti-rabbit IgG (H+L) (LI-COR Biosciences, 925-68073, RRID: AB_2716687); used at 1:5000 dilution for immunoblotting.

IRDye 800CW goat anti-mouse IgG (H+L) (LI-COR Biosciences, 925-32210, RRID: AB_2687825); used at 1:5000 dilution for immunoblotting.

Mitochondrial enrichment and sample preparation for immunoblotting. Freshly dissected organs were homogenized with a dounce homogenizer in 50 mM Tris buffer containing sucrose (200 mM), NaCl (150 mM), and EGTA (1 mM) with a protease inhibitor mini tablet (ThermoFischer, 88666). Homogenized samples were centrifuged at a low speed of 1,000 x g for 10 minutes at 4°C, then the supernatant (containing mitochondria) was collected and centrifuged at a high speed of 17,000 x g for 45 minutes. The supernatant was discarded and the pellet (containing mitochondria) was homogenized for 1 minute in RIPA buffer. Homogenized mitochondria were sonicated on ice for three 5 second pulses. A standard BCA assay using Pierce™ BCA Protein Assay Kit (ThermoFischer, 23225) was performed according to the manufacturer's instructions for protein concentration determination. Samples were diluted with RIPA buffer to ensure an equal volume and equal protein concentration of each sample could be loaded into wells for immunoblotting.

Immunoblotting. Samples were loaded into wells on 12-14% acrylamide gels made in-house. Each sample contained 20% 5X SDS buffer containing β-mercaptoethanol. After running the gel at 150V for 1 hr, gels were transferred onto PVDF membranes (Millipore, IPFL00010) and blocked for 1 hr at room temperature in LI-COR Odyssey Blocking Buffer (LI-COR, 927-40000). Primary antibodies were diluted in blocking buffer at specified concentrations and incubated overnight at 4°C. Membranes were washed with PBST and PBS, then incubated with secondary antibody for 1 hr at 25°C and washed again before imaging. Membranes were imaged and bands were quantified using the LI-COR Odyssey CLx Imaging System (RRID:SCR_014579). Gels were repeated a minimum of twice, with images from one representative experiment.

Immunohistochemistry (IHC) and degeneration quantification. All adult eyes were isolated from light-adapted zebrafish, and a small incision in the cornea was made to allow 4% paraformaldehyde fixative to enter the eye. Whole larvae were euthanized then incubated in 4% paraformaldehyde. After fixation overnight at 4°C, eyes were rinsed in PBS then subject to a sucrose gradient (20% and 30%), embedding in OCT, and cryosectioned at 12 µm. For sections stained with MCU antibody, antigen retrieval was performed by steaming sections in 10 mM sodium citrate (0.05% Tween-20, pH 6.0). Sections were washed in PBS, then blocked in PBS containing 5% donkey serum, 2 mg/mL bovine serum albumin, and 0.3% Triton X-100 for 1 hr. Primary antibodies were diluted in this buffer as specified, then applied to cryosection overnight at 4°C. Secondary antibodies were diluted as specified and applied to section for 1 hr in darkness at 25C. For PNA-labelled samples, sections were incubated in diluted PNA-647 for 30 minutes at 25°C. Tissues were washed, incubated in Hoescht stain for 10 minutes, then

mounted in Fluoromount-G® (SouthernBiotech, 0100-01) under glass coverslips. Slides were imaged using a Leica LSP8 confocal microscope with a 63X oil objective. Leica LAS-X software (RRID:SCR_013673) was used to acquire images.

For quantification of cone nuclei in *gnat2*:GFP fish, high-resolution images of whole zebrafish retina slices were stitched together using ImageJ Grid/Collection stitching.[125] Both the dorsal and ventral regions of the retina were straightened along the cone nuclei axis using ImageJ from the optic nerve to the cilliary margin. This axis was divided into 5 equal parts, then double-cone nuclei were counted in each region, normalizing to the length in µm (height of the region was equal across samples, double cone nuclei are along a single axis). Double-cone nuclei were used for quantification as they are most easily distinguished from rod nuclei. GFP expression was used to confirm that the double-cone nuclei counted were indeed cone nuclei. All counting was performed blinded (masked) to sample identity.

Live larval imaging of mtGCaMP3. Larvae used for imaging were maintained in embryo media containing 0.003% 1-phenyl 2-thiourea (PTU, Sigma-Aldrich P7629) starting at 20 hours post-fertilization. Live zebrafish larvae were analyzed at 6 days postfertilization (dpf) by transferring to 0.5% low melting point agarose containing embryo media with 0.003% PTU and 0.02% (w/v) Tricaine (Sigma-Aldrich, E10521). Larvae were positioned in agarose in a petri dish containing embryo media and 0.02% (w/v) tricaine to prevent drying out. Imaging of slices was performed using an Olympus FV1000 in conjunction with Olympus FluoView FV10-ASW software (RRID:SCR_014215). A 40X water objective was used for imaging. The excitation/emission wavelengths used for mito-GCaMP3 were 488/510 nm. Timelapse images of live larvae were collected with a z-depth of 2 µm and were collected every 20 minutes. Images of total eye mitochondrial clusters were also collected at a z-depth of 2 µm. For quantification of total mito-GCaMP3 fluorescence, images of whole larval eyes were collected, and a fixed ROI centered on the nasal region of the retina was used for quantification. This region near the ventronasal patch is comprised of the most mature cone photoreceptors.[126] For quantification of mislocalized mitochondria, laser power was increased to saturate signals and allow visualization of all mitochondria. Stacks of 50 µm in depth were collected across the entire eye for quantification and mitochondrial clusters were counted blinded (masked) to sample identity. Larval experiments were repeated across at least two cohorts of siblings, with images and quantification from a representative experiment.

Retinal slice imaging of GCaMP3 and mito-GCaMP3. Slices were prepared as described previously.[79,127] For GCaMP3 cytosolic clearance experiments, slides were preincubated in KRB containing 0 mM Ca^{2+} and 0.4 mM EGTA for 10 minutes. Images of single optical slices were collected every 2 seconds. A 5 mM $CaCl_2$ bolus (accounting for EGTA) was injected into the slice imaging chamber 30s after the initial timelapse collection to establish baseline fluorescence. Injection volume was 1 mL into the 4mL imaging chamber, mixed thoroughly. These experiments in the MCU-overexpressing fish were additionally performed in the presence of Ru360 (Millipore, 557440) at 100 µM, in which slices were incubated for 1 hr prior to incubation in 0 mM Ca^{2+} media. Retinas treated with Ru360 were maintained in Ru360 throughout timelapse experiments. Dying cells near the cut edge that were constitutively loaded with Ca^{2+} and cells that did not respond to Ca^{2+} were not included in analysis.

For mito-GCaMP3 timelapse experiments, z-stacks of 15, 2 µm slices were collected every 30 seconds. Retinal slices in modified KRB containing 2 mM $CaCl_2$ were first imaged for 5 minutes to establish baseline mito-GCaMP3 fluorescence. Next, the chamber was injected with ionomycin (Sigma, 407950) to a final concentration of 5 µM (prepared in DMSO, at a final concentration of 0.1%) for another 5 minutes of image collection. Finally, an excess of EGTA (5 mM) was injected to chelate the 2 mM Ca^{2+} present in solution and images were collected for another 5 minutes. Injection volume was 1 mL into the 4mL imaging chamber, mixed thoroughly. Dying cells containing fragmented mitochondrial clusters constitutively loaded with Ca^{2+} and clusters that did not respond to ionomycin were not included in analysis. Additionally, any clusters where the maximum fluorescence signal in the presence of ionomycin was completely saturated were excluded from analysis. Analysis was conducted blinded (masked) to sample identity.

The excitation/emission wavelengths used for both GCaMP3 and mito-GCaMP3 were 488/510 nm. Timelapses were analyzed using ImageJ + Fiji software (SCR_002285). Images were corrected for X-Y drift using the MultiStackReg plugin of ImageJ. For both cell body GCaMP3 and mito-GCaMP3 fluorescence ex vivo timelapses, fixed ROIs were used to quantify average fluorescence signal across the cluster/cell at every time point. Fluorescence of cytosolic GCaMP3 for timelapse analysis are reported as F/F_0, where F_0 is the baseline fluorescence. For mito-GCaMP3 fluorescence, the relative fluorescence at maximum was set to 100% for normalization. We used the equation $[Ca^{2+}] = K_D \times \frac{\theta}{1-\theta}$, where $\theta = \frac{F_0 - F_{min}}{F_{max} - F_{min}}$ to approximate $[Ca^{2+}]_{mito}$, where F_0 is the average "baseline" fluorescence, F_{max} is maximum fluorescence upon

ionomycin addition, and F_{min} is the baseline fluorescence upon EGTA addition. We approximated the K_D of GCaMP3 at 345 nM for the calculation.[86]

Electroretinograms (ERG). Zebrafish were briefly dark-adapted (~30min), before euthanasia by ice water immersion. Eyes were enucleated into Modified Salamander Ringer's solution(mM): NaCl 110, KCl 2.5, $CaCl_2$ 1.0, $MgCl_2$ 1.6, HEPES 10.0, Glucose 10.0, with pH adjusted to 7.8 with NaOH. The eyes were hemisected and retinas isolated from the eyecup. All procedures after the dark adaptation were performed under dim red light. To ensure *ex vivo* ERG signal was predominantly cone responses, dark adaption was limited to ~30 min to allow cone photopigment regeneration but not provide enough time for full rod photopigment regeneration. Furthermore, experiments were carried out during the day (between 11am-4pm) when rod contributions to retinal responses are at their lowest due to the circadian regulation of photoreceptor biology in the zebrafish retina. *Ex vivo* electroretinogram (ERG) recordings were performed as described previously.[128] Isolated retinas were mounted photoreceptor side up onto the specimen holder,[129] and perfused with Modified Salamander Ringer's solution, supplemented with 40µM DL-AP4 (Tocris Bioscience) and 40µM CNQX (Tocris Bioscience) to isolate the photoreceptor component of the ERG signal (A-wave). The rate of perfusion was ~5 mL/minute and the experiments were conducted at room temperature (~23 ^{o}C).

ERG signal was first amplified (100X) and low-pass filtered at 300 Hz by a differential amplifier (DP-311, Warner Instruments), and data was further amplified (10X) and acquired at 10KHz using an integrated amplifier/digitizer (IPA, Sutter Instrument, CA). A High-Power LED light source (Solis-3C, Thorlabs, Newton, NJ), with filter for red light (630 nm, FWHM bandwidth 69 nm, FF01-630/69-25, Semrock, Rochester, NY) and LED driver (DC2200, Thorlabs) were used to provide the flashes of light stimuli, durations ranged from 5-100ms. The SutterPatch software (SutterPatch v1.1.2, Sutter Instrument, CA) drove both stimulus generation and data acquisition via the IPA amplifier's analogue output and input, respectively. Light stimuli were calibrated before experiments using a calibrated photodiode (FDS100-CAL, Thorlabs, Newton, NJ) and flash intensities converted to photons/µm^2.

Data analysis, including statistical analysis and figure preparation, was performed with GraphPad v 8.00 (for Windows, GraphPad Software, CA, USA). Normalized responses were calculated for each retina by dividing the response amplitude data by the maximal amplitude measured at the peak/plateau of the response to the brightest flash. To quantify the gain of phototransduction activation, we fitted the Lamb-Pugh model to the initial leading edge of the

dim flash response for each retina, and compared the average amplification constant (A) between WT and OE siblings.[103]

Isotopic Labeling and Mass Spectrometry. Krebs-Ringer bicarbonate (KRB) buffer optimized for metabolic analysis was used in these experiments.[130] Zebrafish retinas were first dissected in KRB buffer containing U-^{12}C-glucose or U-^{12}C-glutamine at the same concentration they would be incubated in. After dissection, retinas were placed in dishes of pre-warmed KRB containing either U-^{13}C glucose (5 mM, Cambridge Isotopes, CLM-1396) or U-^{13}C glutamine (0.1 - 2 mM, Cambridge Isotopes, CLM-1822). Retinas were incubated in this solution for the specified time points at 28°C in a NAPCO Series 8000 WT CO_2 incubator (5% CO_2), then washed in ice-cold PBS and flash frozen in liquid nitrogen. Metabolites were extracted using ice-cold 80% MeOH and lyophilized. Two-step derivatization was performed by the addition of 20 mg/mL Methoxyamine HCl dissolved in pyridine, followed by *tert*-butyldimethylsilyl. Metabolites were analyzed on an Agilent 7890/5975C GC-MS as described extensively in previous work.[115,130–132] Metabolic flux experiments were repeated a minimum of twice, using three retinas from three different zebrafish for each condition in each experiment. Data shown are results from one representative experiment.

Electron microscopy and Richardson's staining. Adult zebrafish eyes were enucleated and a small incision was made in the cornea to allow fixative (4% glutaraldehyde in 0.1 M sodium cacodylate buffer, pH 7.2) to enter the eye. Tissues were stored at 4°C before postfixation in osmium ferrocyanide (2% osmium tetroxide/3% potassium ferrocyanide in buffer) for 1 hr, followed by incubation in 1% thiocarbohydrazide for 20 min. Samples were then incubated in 2% osmium tetroxide for 30 min at RT, and stained with 1% aqueous uranyl acetate overnight at 4°C. Samples were next stained en bloc with Walton's lead aspartate for 30 min at 60°C, dehydrated in a graded ethanol series, and embedded in Durcupan resin. Sections of tissue were cut at 60 nm thickness and imaged using a JEOL JEM-1230 transmission electron microscope or Zeiss Sigma VP scanning electron microscope. Samples of larval zebrafish eyes were imaged in conjunction with a Gatan 3View2XP ultamicrotome apparatus to generate stacks of EM images, which were aligned using TrakEM2 software (RRID:SCR_008954). Position in the eye for EM imaging was confirmed by cutting slices of tissue and staining with Richardson's stain.[133] These slices were imaged for histological analysis using a Nikon Eclipse

E1000 with a Nikon Plan Apo 100X/1.40 DIC lens. Nikon ACT-1 software was used for image capture. For quantification of mislocalized mitochondria, multiple sections were cut and imaged for each eye and the average number of mitochondria outside of the ellipsoid is reported for each eye. All counting was performed blinded (masked) to sample identity.

Enzyme histochemistry. To assay respiratory complex activity, we used similar methods to previous studies in retinal tissue.[134,135] Zebrafish retinas were isolated in PBS then immediately embedded into OCT cryomolds. These unfixed samples were cryosectioned at 12 µm thickness and assays were performed the same day. Slides were stained for 10 min at 37°C. To assay MTCO activity, sections were incubated in a positive reaction mixture (4 mM 3,3'-diaminobenzidine hydrochloride, 6 mg/mL reduced cytochrome c, and 5 IU/mL catalase in PBS, pH 7.0) or negative control (same mixture with 2.5 mM sodium azide). SDH activity was assayed by incubating sections in positive reaction mixture (13 mM sodium succinate, 1.5 mM nitro blue tetrazolium, 0.2 mM phenazine methosulphate, and 1.0 mM sodium azide in PBS, pH 7.0) or negative control (same mixture omitting sodium succinate). Sections were washed in PBS then dehydrated for 2 min each in an ethanol series (2x70%, 2x95%, 99.5%) then cleared in xylenes for 10 min before mounting with Permount (ThermoFisher) for imaging. All reagents were sourced from Sigma unless otherwise noted. Brightfield images of section were captured using a Nikon Eclipse E1000 light microscope with a 40X oil objective. Images were analyzed masked to sample identity using ImageJ software. Single mitochondrial clusters were selected to measure pixel intensity relative to background.

Oxygen consumption assays. Oxygen consumption as measured using a flow culture system.[136] Intact zebrafish retinas were loaded into chambers between layers of cytodex beads, with a total of 6 retinas per chamber. KRB buffer containing 5 mM glucose was used as perifusion buffer and continuously equilibrated with 5% CO_2, 21% O_2, balance N_2. Oxygen tension was measured by lifetime phosphorescence detection (Tau Theta, Inc) of the oxygen-sensitive dye platinum tetrapentafluorophenyl porphyrin (Frontier Science), which was painted on the inside of the perifusion chamber. Oxygen consumption rate was calculated as the flow rate times the difference between inflow and outflow levels of oxygen.

Statistics. Numerical results in text are reported as mean ± standard error of the mean unless otherwise stated. Statistical tests were performed using Graphpad Prism v 8.00 software. For statistical analysis, replicates (n) were always defined as biological replicates. Information on what constitutes n (e.g. larvae, retinas, cells) is listed in the figure legend of each experiment. Samples sizes were estimated based on previous experiments.[79,102,115] For data sets with sufficient n to analyze population distribution, tests for normality were administered (Anderson-Darling, D'Agostino & Pearson, Shapiro-Wilk, Kolmogorov-Smirnov). For data sets that did not pass a majority of normality tests, the median is instead reported along with the interquartile range (Q1 and Q3).

Acknowledgements

The majority of the work described in this chapter was published in Nature Cell Death and Differentiation. The other authors that contributed to this study were Celia M. Bisbach, Fatima Abbas, Daniel C. Brock, Whitney M. Cleghorn, Edward D. Parker, Benjamin H. Bauer, William Ge, Frans Vinberg, James B. Hurley & Susan E. Brockerhoff. Brian Robbings, Austin Roundtree, and Ian Sweet contributed to additional unpublished data. We thank the University of Washington ISCRM aquatics facility and the University of Utah CZAR for providing zebrafish husbandry, laboratory space, and equipment. Expansion of the CZAR is supported in part by NIH grant # 1G20OD018369-01. This work was supported by PHS NRSA T32GM007270 from NIGMS (RAH), NIH grants NEI EY026020 (JBH and SEB), NEI EY028645 (SEB), P30EY001730 (UW Vision Core), NIH EY014800 (John A. Moran Eye Center), and an Unrestricted Grant from Research to Prevent Blindness, New York, NY, to the Department of Ophthalmology & Visual Sciences, University of Utah.

Chapter 3: Mitochondrial Calcium Uniporter (MCU) deficiency reveals an alternate path for calcium update in photoreceptor mitochondria

Introduction

Maintaining proper intracellular Ca^{2+} homeostasis is essential for cellular function. Mitochondria have the ability to sequester Ca^{2+} via the Mitochondrial Calcium Uniporter complex (MCU).[47,48] Mitochondrial Ca^{2+} uptake via MCU can modulate both cytosolic and mitochondrial Ca^{2+} levels, meaning that Ca^{2+}-sensitive reactions that occur in both compartments can be affected by MCU activity. In the mitochondrial matrix, increasing Ca^{2+} can stimulate tricarboxylic (TCA) cycle dehydrogenases and enhance ATP production, although Ca^{2+} overload in the matrix can trigger cell death.[35,44] Ca^{2+} also regulates biochemistry in the cytosol and thus, mitochondrial Ca^{2+} uptake can influence cytosolic reactions. Since the specific roles of Ca^{2+} in the cytosol are diverse, the role of mitochondrial Ca^{2+} uptake can be cell-type specific.[116,137]

Photoreceptors, the light-sensitive neurons in the retina, rely on spatially distinct changes in cytosolic Ca^{2+} to regulate both phototransduction and neurotransmission. At the outer segment, intracellular Ca^{2+} changes in response to light stimulation and this is critical for timely shut-down of the phototransduction cascade and light adaptation.[138] At the synapse, changes in intracellular Ca^{2+} modulate vesicle release and neurotransmission.[77,78,114] The outer segment and synaptic Ca^{2+} pools that control these functions are separated by a cell body filled with a dense cluster of mitochondria, and evidence suggests that these mitochondria may help isolate these pools from each other. Mitochondria from zebrafish cones can prevent Ca^{2+} in the outer segment from reaching the rest of the cell and conversely, they can prevent Ca^{2+} in the synapse from reaching the outer segment.[79] Increasing mitochondrial Ca^{2+} uptake in zebrafish cones by overexpressing MCU also accelerates cytosolic Ca^{2+} clearance, which causes cones to recover from light exposure faster.[36]

Efficient uptake of Ca^{2+} into mitochondria could also enhance the ability of photoreceptors to meet their high energy demands. Darkness is the most energetically demanding state of the photoreceptor, and intracellular Ca^{2+} is at its highest levels in darkness.[73,139] If this Ca^{2+} were to enter mitochondria, it could enhance ATP production by stimulating TCA cycle dehydrogenases.[35] In line with this hypothesis, overexpressing MCU in zebrafish cones alters

the distribution of TCA cycle metabolites in a way which is consistent with enhanced activity of Ca^{2+}-sensitive dehydrogenases.[36]

These observations suggested to us that mitochondrial Ca^{2+} uptake could play an important role in modulating photoreceptor function. Given this, it is surprising that zebrafish cone photoreceptors express extremely low levels of MCU.[36] MCU has been widely thought to be the sole route of Ca^{2+} entry into mitochondria in eukaryotes, as loss of MCU completely inhibits mitochondrial Ca^{2+} uptake in skeletal muscle, liver, heart, brown adipose tissue, and a wide variety of cell lines.[61,140–143] Despite this, it is possible that certain specialized cell types might not rely solely on MCU for mitochondrial Ca^{2+} uptake, since it also has been observed that brain mitochondria lacking MCU expression do not have a complete loss of mitochondrial Ca^{2+} uptake.[144] Thus, the role that MCU plays in vertebrate photoreceptors remains an open question.

To resolve the role MCU-mediated mitochondrial Ca^{2+} uptake plays in modulating photoreceptor function, we evaluated the morphological, biochemical and physiological consequences of loss of MCU expression using both a global *mcu*$^{-/-}$ zebrafish model and a rod photoreceptor-specific *Mcu*$^{-/-}$ mouse model. Our study demonstrates that MCU is remarkably dispensable for photoreceptor function, which is consistent with our discoveries of very low levels of MCU expression and evidence for an additional mechanism for Ca^{2+} uptake into photoreceptor mitochondria.

Results

Mitochondrial Ca^{2+} uptake in cones from global *mcu*$^{-/-}$ zebrafish is diminished, but not ablated

Global *mcu*$^{-/-}$ zebrafish were generated using the strategy outlined previously.[118] A founder carrying a 12-nucleotide deletion in exon 5, which introduces a premature stop codon in exon 6 of *mcu* was used in this study (*mcu*^{w249}; notated as *mcu*$^{-/-}$, **Figure 3.1A**). We used a custom zebrafish-specific Mcu antibody to probe immunoblots of mitochondria isolated from retinas and brains of WT and global *mcu*$^{-/-}$ zebrafish.[36] Mcu expression is entirely ablated in global *mcu*$^{-/-}$ tissues (**Figure 3.1B**). Similar to the global *Mcu*$^{-/-}$ mouse model, a smaller than expected ratio of homozygous *mcu*$^{-/-}$ zebrafish survive to adulthood from crosses of *mcu*$^{+/-}$ parents (**Table 1**).[140,145] There are no obvious effects of Mcu-deficiency on retinal or photoreceptor morphology (**Figure 3.1C**).

To assess how mitochondrial Ca^{2+} uptake dynamics are altered in *mcu*$^{-/-}$ photoreceptors, we crossed *mcu*$^{-/-}$ zebrafish with zebrafish expressing the mitochondrially-targeted Ca^{2+} sensor GCaMP3 in cones (*gnat2*:mito-GCaMP3).[79] Eyes from live larvae were imaged and we found that there is no difference in basal mito-GCaMP3 fluorescence between WT and *mcu*$^{-/-}$ cones (**Figure 3.1D**). To determine if basal mitochondrial Ca^{2+} in mature cones is altered by loss of Mcu, we imaged ex vivo slices of WT and global *mcu*$^{-/-}$ *gnat2*:mito-GCaMP3 adult zebrafish retinas. We compared baseline mito-GCaMP3 fluorescence (F_0) to the maximum fluorescence (F_{max}, obtained by addition of ionomycin to media containing 2 mM Ca^{2+}) and minimum fluorescence (F_{min}, obtained by the addition of 5 mM EGTA to chelate Ca^{2+}). Similar to larvae, we found that baseline mito-GCaMP3 fluorescence was not significantly different in adult WT and *mcu*$^{-/-}$ zebrafish cones (**Figure 3.1E**). Using the previously reported K_D of 345 nM for the binding of Ca^{2+} to GCaMP3 and the equations $[Ca^{2+}] = K_D \times \frac{\theta}{1-\theta}$ and $\theta = \frac{F_0 - F_{min}}{F_{max} - F_{min}}$, we found WT cone mitochondria have a baseline free $[Ca^{2+}]_{mito}$ of 50.9 ± 3.2 nM and *mcu*$^{-/-}$ cone mitochondria have a baseline free $[Ca^{2+}]_{mito}$ of 48.9 ± 2.7 nM (**Figure 3.1F**) [86].

We next tested whether mitochondrial Ca^{2+} uptake is altered in cones from global *mcu*$^{-/-}$ fish using a strategy previously shown to increase intracellular and mitochondrial Ca^{2+} in photoreceptors [146]. We first incubated WT and global *mcu*$^{-/-}$ *gnat2*:mito-GCaMP3 retina slices with the Na^+/Ca^{2+} exchanger inhibitor KB-R7943 for 10 minutes, limiting clearance of outer segment Ca^{2+}. After this preincubation, baseline measurements of mito-GCaMP3 fluorescence

were taken. Next, slices were treated with the PDE inhibitor sildenafil, which triggers influx of Ca^{2+} into photoreceptors. In WT cones, mito-GCaMP3 fluorescence increases in response to this increase in intracellular Ca^{2+} (**Figure 3.1G,** black fill). In *mcu*$^{-/-}$ cones, average Ca^{2+} influx is decreased by 42.8 ± 9.0 % compared to WT at the endpoint of the timelapse (**Figure 3.1G,** red fill). This average decrease in mito-GCaMP3 fluorescence in *mcu*$^{-/-}$ cones comes from two populations of mitochondria: mitochondria that do not take up Ca^{2+} at all, and mitochondria that take up Ca^{2+} but have a lower fold change in maximum response than the WT. By taking the maximum fold-change of mtGCaMP3 from across all timepoints and excluding mitochondria that did not exhibit an increase in fluorescence, we determined that *mcu*$^{-/-}$ cone mitochondria had 69.1 ± 4.5 % maximum fluorescence change compared to WT siblings ($p<0.01$ using Welch's t-test). The two populations of mitochondria that do or do not respond to Ca^{2+} are apparent at the 15 minute time point (**Figure 3.1H)**.

To assess whether the residual Ca^{2+} uptake in some cone mitochondria could be attributed to an MCU-independent mechanism, we repeated this experiment in the presence of the MCU inhibitor Ru360. Ru360 treatment reduces uptake of Ca^{2+} into WT cone mitochondria. However, we did not detect significant differences between WT cones treated with Ru360, *mcu*$^{-/-}$ cones treated with Ru360, and untreated *mcu*$^{-/-}$ cones (**Figure 3.1G, 3.1H**). In these three conditions, there was a fraction of maximum GCaMP3 fluorescence that was not inhibited by Ru360 or loss of Mcu. Compared to WT, maximum responses were: WT + Ru360: 51.0 ± 2.9%, *mcu*$^{-/-}$: 69.1 ± 4.5%, *mcu*$^{-/-}$ + Ru360: 60.8 ± 3.8%. This indicates that while Mcu is responsible for a portion of mitochondrial Ca^{2+} uptake in cones, Ca^{2+} also can enter mitochondria through an alternate pathway.

	mcu$^{+/+}$	*mcu*$^{+/-}$	*mcu*$^{-/-}$
mcu$^{+/-}$ *Cross #1*	22	29	10
mcu$^{+/-}$ *Cross #2*	15	19	4
mcu$^{+/-}$ *Cross #3*	10	23	10
mcu$^{+/-}$ *Cross #4*	13	20	7
Total	**60**	**91**	**31**

Table 1: Genotyping results from four group crosses of *mcu*$^{+/-}$ zebrafish. A chi-square test determined that the observed *mcu*$^{+/+}$:*mcu*$^{+/-}$:*mcu*$^{-/-}$ ratio of 60:91:31 differed significantly from the expected 1:2:1 ratio (p=0.0098).

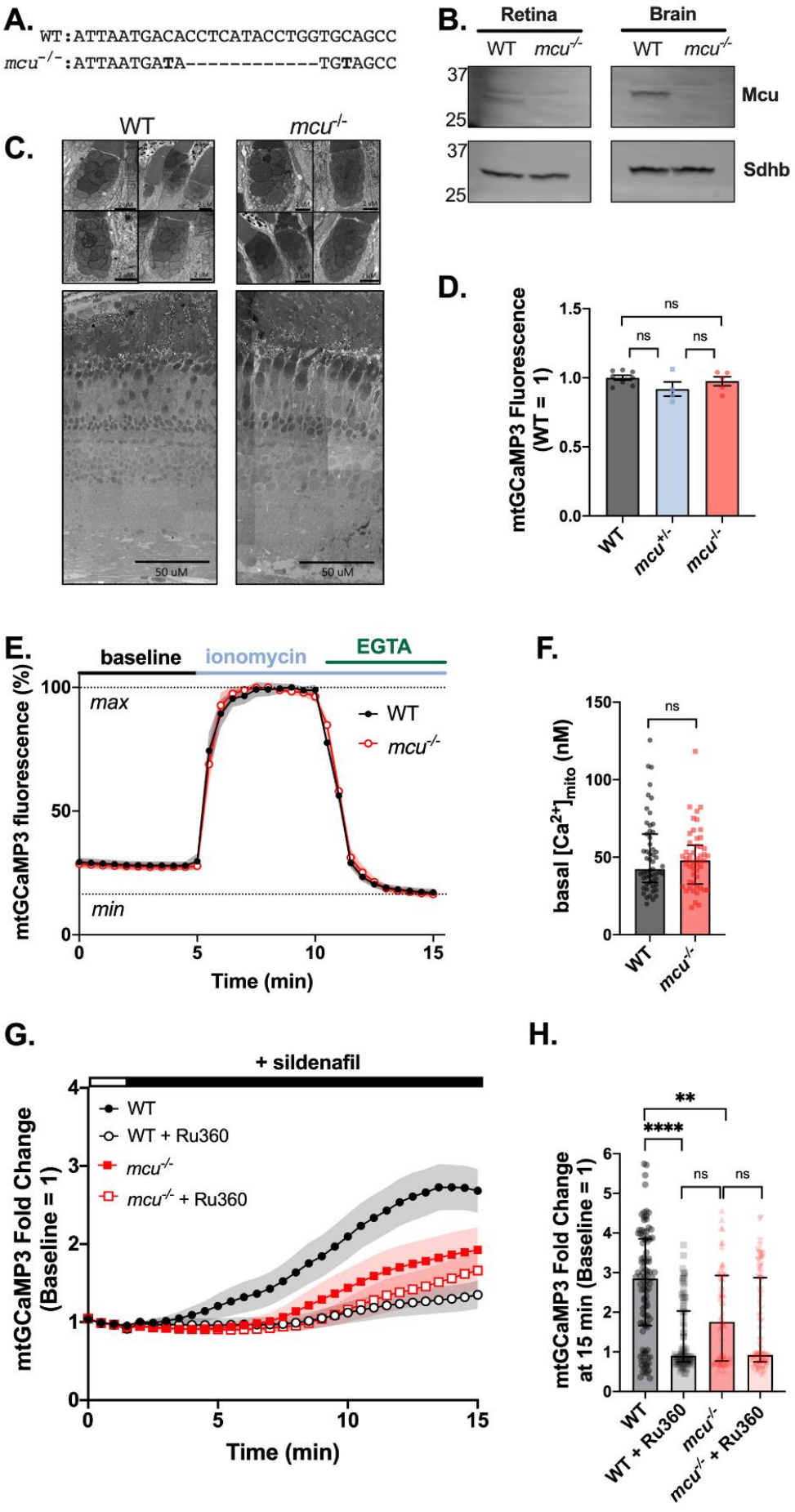
A.
WT:ATTAATGACACCTCATACCTGGTGCAGCC
mcu-/-:ATTAATGATA----------TGTAGCC
B.
Retina
Brain
WT
mcu-/-
WT
mcu-/-
37
25
Mcu
37
25
Sdhb
C.
WT
mcu-/-
50 uM
50 uM
D.
mtGCaMP3 Fluorescence (WT = 1)
ns
ns
ns
WT
mcu+/-
mcu-/-
E.
baseline
ionomycin
EGTA
max
min
WT
mcu-/-
mtGCaMP3 fluorescence (%)
Time (min)
F.
basal [Ca2+]mito (nM)
ns
WT
mcu-/-
G.
+ sildenafil
WT
WT + Ru360
mcu-/-
mcu-/- + Ru360
mtGCaMP3 Fold Change (Baseline = 1)
Time (min)
H.
mtGCaMP3 Fold Change at 15 min (Baseline = 1)
**
****
ns
ns
WT
WT + Ru360
mcu-/-
mcu-/- + Ru360

Figure 3.1: Mitochondrial Ca^{2+} uptake is decreased by global Mcu loss.

A. Alignment of a portion of exon 5 of zebrafish *mcu* showing WT (top) and CRISPR-generated *mcu*$^{-/-}$ (*mcu*^{w249}*;* bottom).

B. Western blot showing Mcu expression in retina and brain from global *mcu*$^{-/-}$ zebrafish. 20 µg of protein from mitochondrial lysate from 6 pooled retinas and 1 brain was analyzed. The custom Mcu antibody detects a faint non-specific band at a slightly higher molecular weight than Mcu.[36]

C. Scanning electron microscopy (SEM) images of WT and *mcu*$^{-/-}$ zebrafish cone mitochondria (top panel) and retinas (bottom panel) from 11-month old sibling fish. Retinal and mitochondrial morphology appear unchanged by loss of Mcu. n=8 retinas from WT and *mcu*$^{-/-}$ zebrafish were examined, representative images from 1 WT and 1 MCU$^{-/-}$ retina are shown.

D. Total cone mitochondrial fluorescence in *gnat2*:mito-GCaMP3 larval zebrafish eyes. The mean is reported with bars indicating standard error. n=8 WT fish, 4 *mcu*$^{+/-}$ fish, and 5 *mcu*$^{-/-}$ fish. ns = not significant using one-way ANOVA with Tukey's multiple comparisons test.

E. Relative mito-GCaMP3 fluorescence of cone mitochondrial clusters in adult retinal slices of WT or *mcu*$^{-/-}$ fish expressing *gnat2*:mito-GCaMP3. Baseline mitochondrial fluorescence was determined in KRB buffer containing 2 mM $CaCl_2$, then ionomycin (5 µM) was added to allow 2 mM Ca^{2+} entry into the mitochondria to saturate the probe. Next, EGTA (5 mM) was added to the solution (holding 5 µM ionomycin constant) to chelate Ca^{2+} and determine minimum mito-GCaMP3 fluorescence. The mean is reported and shaded region = 95% CI. n=55 mitochondrial clusters (3 fish) for WT and n=51 mitochondrial clusters (3 fish) for *mcu*$^{-/-}$.

F. Approximation of resting free $[Ca^{2+}]_{mito}$ in mitochondrial clusters shown in E. The equations $[Ca^{2+}] = K_D \times \frac{\theta}{1-\theta}$ and $\theta = \frac{F_0 - F_{min}}{F_{max} - F_{min}}$ were used with the previously reported K_D of GCaMP3 (345 nM) to calculate the value for each mitochondrial cluster [86]. The median is reported with bars indicating interquartile range. ns = not significant using Mann-Whitney test.

G. *gnat2*:mito-GCaMP3 retina slices preincubated with 100 µM KB-R7943 (10 minutes prior to imaging and white bar) then subjected to 25 µM sildenafil (black bar). For Ru360 treatment, retinal slices were preincubated for 1 hour in 10 µM Ru360 and then the same experiment was performed in the presence of 10 µM Ru360. Traces represent the mean fluorescence of individual mitochondrial clusters at each timepoint. Shaded region indicates 95% CI. n=86 WT mitochondria, n=64 *mcu*$^{-/-}$ mitochondria, n=86 WT + Ru360 mitochondria and n=85 *mcu*$^{-/-}$ + Ru360 mitochondria from 3 fish in each condition.

H. Comparison of mtGCaMP3 fluorescence of individual mitochondria at the 15 minute timepoint of data shown in G. The median is reported with bars indicating interquartile range. Each datapoint represents an individual mitochondrial cluster. *p<0.05 and ****p<0.0001 using Kruskal-Wallis test with Dunn's multiple comparisons test).

Retinas from *mcu*$^{-/-}$ zebrafish have normal metabolism and photoresponses

We next determined if the diminished ability of *mcu*$^{-/-}$ mitochondria to take up Ca^{2+} in cones might lead to metabolic or electrophysiological defects. To assess potential changes in metabolism, we measured total metabolite levels from freshly dissected dark-adapted retinas from *mcu*$^{-/-}$ zebrafish. We detected no changes in total metabolite levels in *mcu*$^{-/-}$ retinas, although α-ketoglutarate levels trend slightly but not significantly higher after loss of Mcu (**Figure 2A**). Previous studies of MCU$^{-/-}$ tissues describe an increase in the amount of phosphorylated pyruvate dehydrogenase (PDH), which is attributed to diminished activity of the Ca^{2+}-sensitive phosphatase PDP1c.[140,141,147–149] We assessed the P-PDH/PDH ratio found that it is not different between WT and *mcu*$^{-/-}$ retinas (**Figure 2B**). This result is consistent with the unaltered resting Ca^{2+} levels we observed in *mcu*$^{-/-}$ cones.

Photoreceptors rely on efficient clearance of cytosolic Ca^{2+} from the outer segment to stimulate recovery of the photoresponse.[80] Photoresponses of zebrafish cones that overexpress Mcu recover faster following a flash of light, suggesting that uptake of Ca^{2+} through Mcu could contribute to clearing outer segment Ca^{2+} in the time course of flash responses.[36,150] Our Ca^{2+} measurements suggest that at high outer segment Ca^{2+}, Mcu contributes to ~30-50% of mitochondrial Ca^{2+} uptake. Thus, loss of this fraction of Mcu-mediated Ca^{2+} sequestration could slow the recovery kinetics of the cone light responses. To test this, we measured both bright and dim flash responses from WT and *mcu*$^{-/-}$ cones using *ex vivo* electroretinography (ERG). Recovery kinetics are unaltered by Mcu deficiency (**Figures 2C, D**). Both the maximum amplitude and sensitivity of the response are unchanged by loss of Mcu expression (**Figures 2E** and **2F**, respectively).

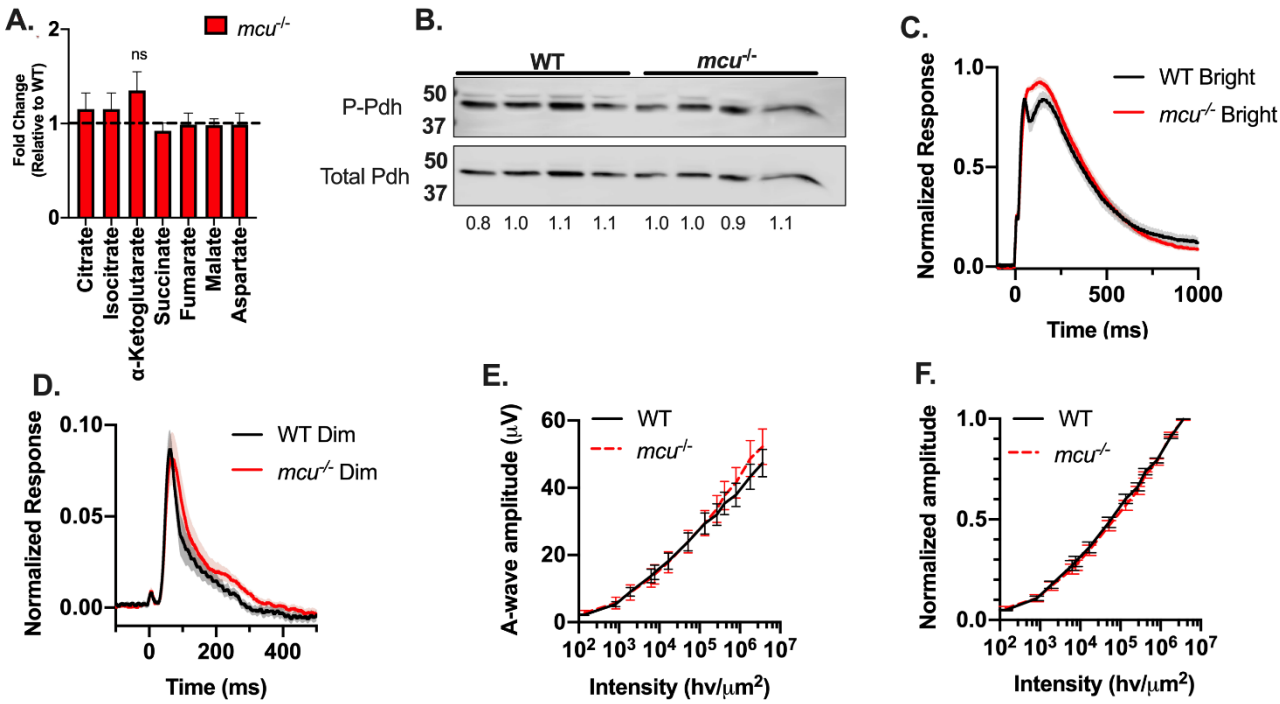

Figure 3.2: Retinas from global *mcu*$^{-/-}$ zebrafish have normal metabolism and photoresponses.

A. Total TCA cycle metabolite levels in *mcu*$^{-/-}$ zebrafish retinas relative to WT. Zebrafish were dark-adapted for 18h and retinas were dissected under red light. α-ketoglutarate levels trend higher in *mcu*$^{-/-}$ zebrafish retinas, although they are not significantly different than WT (1.4 ± 0.5-fold higher in *mcu*$^{-/-}$ retinas, p=0.09 using Welch's t-test, mean ± standard deviation is reported, n=6 WT and 6 *mcu*$^{-/-}$ retinas from 3 different fish each).

B. P-Pdh and total Pdh immunoblot from dark-adapted WT and global *mcu*$^{-/-}$ zebrafish retinas. 15 µg of protein was loaded in each lane. Quantification of the P-Pdh/Pdh ratio of each sample relative to the average WT P-Pdh/Pdh ratio is shown below each lane (n=4 WT and 4 *mcu*$^{-/-}$ retinas from 4 different fish each).

C. Ex vivo ERG a-wave responses from WT and *mcu*$^{-/-}$ zebrafish retinas. Cone responses were isolated using DL-AP4 (40 µM) and CNQX (40 µM) and normalized to R_{max} (the maximum response at the brightest light intensity). Bright flash stimulus intensity is 3,650,000 photons µm^{-2} and 2-23 ms in duration. The mean is reported and the shaded region indicates standard error (n=21 retinas from 12 WT fish and 21 retinas from 13 global *mcu*$^{-/-}$ fish).

D. Ex vivo ERG a-wave responses from WT and *mcu*$^{-/-}$ zebrafish retinas under dim flash stimulus under the same conditions as (C).

E. a-wave response amplitude data plotted as a function of stimulus intensity (photons µm^{-2}) of WT and global *mcu*$^{-/-}$ retinas from experiments shown in (C) and (D). Bars indicate standard error.

F. Normalized response amplitude data for experiments shown in (C) and (D) indicate that sensitivity is not changed in global *mcu*$^{-/-}$ cones (Bars indicate standard error)

Rod photoreceptors express low levels of MCU

We did not detect any metabolic or physiological consequences caused by Mcu deficiency in zebrafish retinas. However, phenotypes can vary significantly between chronic, induced, and tissue-specific *Mcu*$^{-/-}$ animal models.[116] For example, the cardiac phenotype from the global *Mcu* $^{-/-}$ mouse is surprisingly mild, while constitutive and inducible heart-specific *Mcu* knockdown models have both different and more severe phenotypes.[140,142,148,151,152] This indicates that some tissues have both the capacity and the necessity to adapt to chronic loss of MCU. Since we observed that a smaller than expected number of *mcu*$^{-/-}$ fish reach adulthood from *mcu*$^{+/-}$ crosses, it is possible that the *mcu*$^{-/-}$ fish that survived to adulthood adapted to loss of Mcu in some way. In order to ensure that the mild phenotypes we observed in global *mcu*$^{-/-}$ zebrafish retinas were truly due to the dispensable nature of MCU in photoreceptors and not due to adaptations made in response to chronic loss of MCU, we also generated a rod photoreceptor specific *Mcu*$^{-/-}$ mouse model in which MCU expression is lost only upon photoreceptor differentiation.

We blocked expression of MCU specifically in rod photoreceptors by crossing mice with loxP sites flanking exons 5 and 6 of *Mcu* (*Mcu*^{fl}) with mice expressing Cre-recombinase under control of a rod-specific opsin promoter (iCre-75) which is active once rods have differentiated.[153] Immunohistochemistry of adult *Mcu*^{fl} iCre-75 (annotated as Rod *Mcu*$^{-/-}$) retinas reveal that MCU expression is ablated in the rod photoreceptors (**Figure 3A,** arrow indicates the photoreceptor mitochondria layer). The photoreceptor layer in the mouse retina is composed mainly of rods, with a ~35:1 rod:cone ratio.[154] To determine if cones still express MCU in Rod *Mcu*$^{-/-}$ retinas, we co-stained WT and Rod *Mcu*$^{-/-}$ retinal slices with an MCU antibody and the cone marker peanut agglutinin (PNA) (**Figure 3B**). We observed MCU staining beneath each PNA-stained outer segment, indicating that cones retain MCU expression.

Cone photoreceptors from zebrafish retinas express very low levels of Mcu.[36] To determine if MCU expression in mouse rods is similarly low, we analyzed MCU expression in WT and Rod *Mcu*$^{-/-}$ retinas using immunoblot (**Figure 3C**). MCU expression is not significantly altered in Rod *Mcu*$^{-/-}$ retinas relative to WT, despite rods being by far the most abundant cell type in the mouse retina [154]. This indicates that MCU expression is extremely low in rods relative to other cell types in the retina. Overall retinal and photoreceptor morphology appears to be unaltered by loss of MCU expression in rods: we observed no defects in our immunohistochemistry images and scanning electron microscopy (SEM) analysis of Rod *Mcu*$^{-/-}$ retinas at 6-months old revealed no changes in retinal morphology (**Figure 3D**).

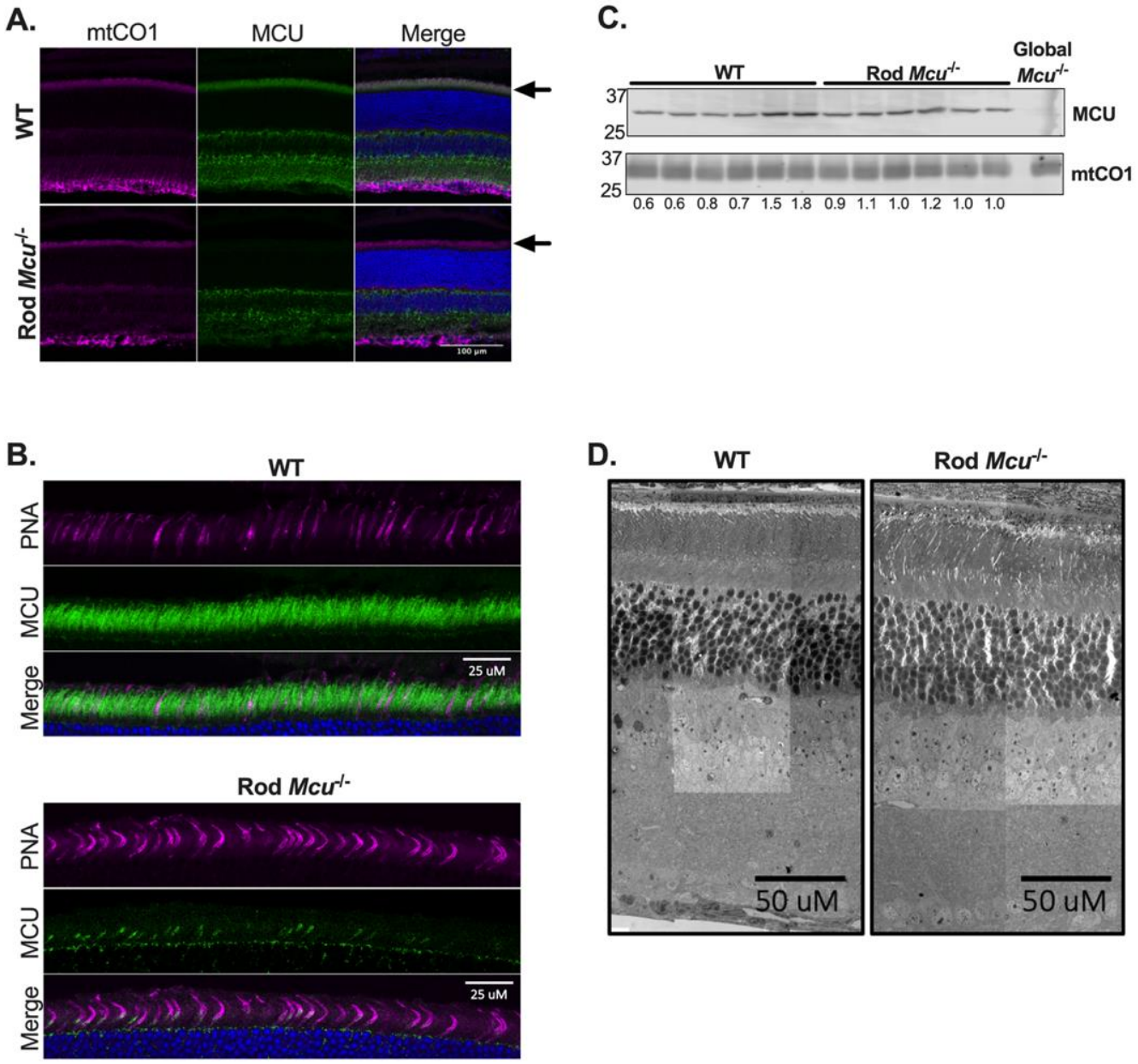

Figure 3.3: Rods express low levels of MCU.

A. Immunohistochemistry showing MCU expression in WT and Rod *Mcu*$^{-/-}$ retinas. mtCO1 (Mitochondrial Cytochrome Oxidase subunit 1) is used to label mitochondria. An arrow indicates the photoreceptor mitochondria layer.

B. Immunohistochemistry showing MCU expression and PNA-647 (staining cone outer segments). MCU is still expressed in cones from Rod *Mcu*$^{-/-}$ retinas.

C. Western blot showing MCU expression in whole retinas from Rod *Mcu*$^{-/-}$ mouse. 15 µg of retinal protein lysate was loaded in each lane. MCU expression is not significantly altered in Rod *Mcu*$^{-/-}$ retinas (1.02 ± 0.03 fold higher in Rod *Mcu*$^{-/-}$ retinas, mean ± standard deviation is reported, ns using Welch's t-test). Retinal lysate from a global *Mcu*$^{-/-}$ mouse is used as a control to show specificity of MCU antibody (far right lane). The MCU/mtCO1 ratio for each sample relative to WT average is shown under each lane (n=6 WT and 6 Rod *Mcu*$^{-/-}$ retinas from 3 animals each).

D. SEM images from 6-month old WT and Rod *Mcu*$^{-/-}$ retinas. (retinas from n=3 mice were imaged, representative images from 1 WT and 1 Rod *Mcu*$^{-/-}$ retina shown).

Rod *Mcu*$^{-/-}$ retinas accumulate α-ketoglutarate

Overexpressing MCU in zebrafish cone photoreceptors leads to changes in the steady-state concentrations of TCA cycle metabolites, likely due to increased Ca^{2+} binding lowering the K_m of α-ketoglutarate dehydrogenase (α-KGDH) and isocitrate dehydrogenase.[36] To test if the reduced mitochondrial Ca^{2+} uptake ability of *Mcu*$^{-/-}$ photoreceptors causes a subsequent increase in enzyme K_m, we used gas chromatography-mass spectrometry to evaluate the influence of MCU on metabolic flux in retinas. We incubated retinas from WT and Rod *Mcu*$^{-/-}$ light-adapted mice in 5 mM U-^{13}C-glucose for 0, 5, and 30 minutes and quantified accumulation of unlabeled and labeled metabolites using GC-MS (an isotopomer diagram is included in Figure **3.4A**). When we measured total metabolite levels at each time point, we observed that the TCA cycle metabolite α-ketoglutarate was consistently elevated in Rod *Mcu*$^{-/-}$ retinas (α-ketoglutarate levels are elevated 1.99 ± 1.09-fold at 0 minutes; 1.46 ± 0.36-fold 5 minutes, and 1.90 ± 0.77-fold at 15 minutes; mean ± standard deviation propagated to include variation of WT samples reported) (**Figure 3.5A**). Labeled α-ketoglutarate (m2 α-ketoglutarate made in the first round and m3 α-ketoglutarate made in the second round) also accumulate to slightly higher steady state levels in Rod *Mcu*$^{-/-}$ retinas (**Figure 3.5B, Supplemental Figure 3.4B**). Other metabolites do not accumulate consistently differently in Rod *Mcu*$^{-/-}$ retinas compared to WT. Since binding of Ca^{2+} lowers the K_m of α-KGDH, a possible explanation for this accumulation of α-ketoglutarate is that loss of MCU expression in rods has limited Ca^{2+} access to α-KGDH, raising the enzyme's K_m for α-ketoglutarate.[35,96] A higher K_m would increase the steady-state concentration of α-ketoglutarate required to maintain α-KGDH activity.

Energy demands are significantly higher in darkness, and intracellular Ca^{2+} levels in photoreceptors can increase 10- to 60-fold in darkness relative to light.[73,155,156] So, it is possible that MCU plays a larger role in modulating photoreceptor metabolism in darkness. We first determined how darkness normally alters steady-state metabolite levels by comparing metabolite abundance between light- and dark-adapted WT retinas (for dark-adapted retinas, mice were dark-adapted for 18h and retinas were dissected and snap-frozen under infrared light). In WT retinas, steady-state levels of many metabolites are slightly but significantly lower in darkness relative to light, with α-ketoglutarate and pyruvate levels being the most reduced (α-ketoglutarate: 0.61 ± 0.12-fold lower; pyruvate: 0.62 ± 0.23-fold lower; mean ± standard deviation propagated to include variation of "light" samples) (**Figure 3.5C)**. We repeated this comparison using light- and dark-adapted Rod *Mcu*$^{-/-}$ retinas. We observed the same trend in

that the steady-state levels of many metabolites are slightly but significantly lower in dark-adapted Rod *Mcu*$^{-/-}$ retinas compared to light-adapted Rod *Mcu*$^{-/-}$ retinas (**Figure 3.5D**). Similar to what was observed in WT retinas, both pyruvate and α-ketoglutarate levels are the most reduced in Rod *Mcu*$^{-/-}$ retinas (α-ketoglutarate: 0.71 ± 0.20-fold lower; pyruvate: 0.82 ± 0.15-fold lower; mean ± standard deviation propagated to include variation of "light" samples). When comparing the fold change in metabolite abundance in darkness relative to light, it first appeared as though the influence of darkness in Rod *Mcu*$^{-/-}$ retinas tended to be smaller than that of WT retinas. This would be expected if Ca^{2+} uptake via MCU mediated the change in metabolite pool size we observe in darkness relative to light. To test if this were true, we directly compared the fold change in steady-state metabolite levels in darkness and light between WT and Rod *Mcu*$^{-/-}$ retinas (**Figure 3.5E**). While the influence of darkness on pyruvate and α-ketoglutarate is slightly different between WT and Rod *Mcu*$^{-/-}$ retinas, we found that this difference is not statistically significant. This indicates that while MCU might play a small role in modulating steady-state metabolite levels in darkness, it is likely not the primary effector of change.

We next assessed if loss of MCU expression altered metabolic flux in dark-adapted retinas differently than in light-adapted retinas. WT and Rod *Mcu*$^{-/-}$ mice were dark-adapted for 18h and retinas were dissected, incubated in U-^{13}C-glucose, and snap-frozen all under infrared light. Once again, we found that steady-state α-ketoglutarate levels from freshly-dissected dark-adapted retinas are consistently higher in Rod *Mcu*$^{-/-}$ retinas compared to WT (α-ketoglutarate levels are elevated 1.56 ± 0.20-fold at 0 minutes, 1.93 ± 0.45-fold at 5 minutes, and 1.41 ± 0.17-fold at 30 minutes; mean ± standard deviation propagated to include variation of WT samples) (**Figure 3.5F**). We also observed a similar increase in Rod *Mcu*$^{-/-}$ m2 and m3 α-ketoglutarate levels throughout the time course of U-^{13}C-glucose incubation (**Figure 3.5G, Figure 3.4C**). Overall, we found that metabolic flux in dark-adapted Rod *Mcu*$^{-/-}$ retinas matches flux in dark-adapted WT retinas except for a consistent accumulation of α-ketoglutarate.

Finally, we determined if loss of MCU expression in rods might alter the P-PDH/PDH ratio. Our immunoblot analysis showed that the P-PDH/PDH ratio in light-adapted Rod *Mcu*$^{-/-}$ retinas was not different than in WT (**Supplemental Figure 4D**). Accordingly, we did not observe a decrease in citrate production in our isotopic labeling experiments in either light- or dark-adapted Rod *Mcu*$^{-/-}$ retinas.

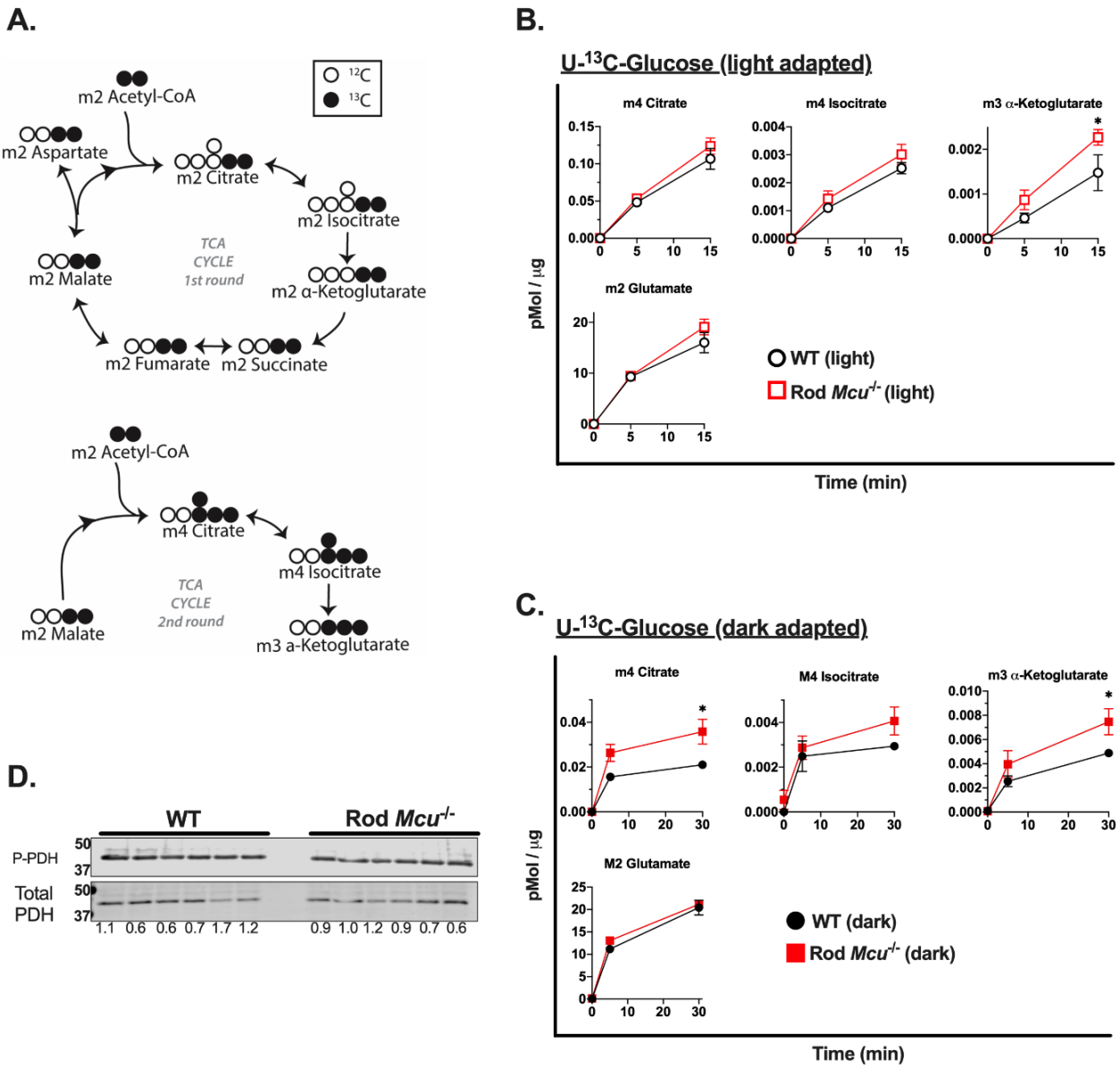

Figure 3.4: Loss of MCU leads to a buildup of α-ketoglutarate in Rod *Mcu*$^{-/-}$ retinas.

A. Isotopomer diagram showing labeling pattern of TCA cycle metabolites made by retinas supplied with U-13C-glucose.

B. Additional metabolites from the time course of light-adapted WT and Rod MCU$^{-/-}$ retinas incubated in U-^{13}C-glucose for 0, 5, and 15 minutes (n=3 WT and 3 Rod MCU$^{-/-}$ retinas per time point) (* = $p<0.05$ using Welch's t-test).

C. Additional metabolites from the time course of dark-adapted WT and Rod MCU$^{-/-}$ retinas incubated in U-^{13}C-glucose for 0, 5, and 15 minutes (n=3 WT and 3 Rod MCU$^{-/-}$ retinas per time point) (* = $p<0.05$ using Welch's t-test).

D. Western blot of WT and Rod MCU$^{-/-}$ retinas probed with PDH E1a antibody and a phospho-PDH antibody. The P-PDH/PDH ratio is 0.89 (+/- 0.42)-fold lower in Rod MCU$^{-/-}$ retinas (ns). Quantification of the P-PDH/PDH ratio of each sample relative to the average WT P-PDH/PDH ratio is shown below each lane (n=6 WT and 6 Rod MCU$^{-/-}$ retinas from 3 animals each).

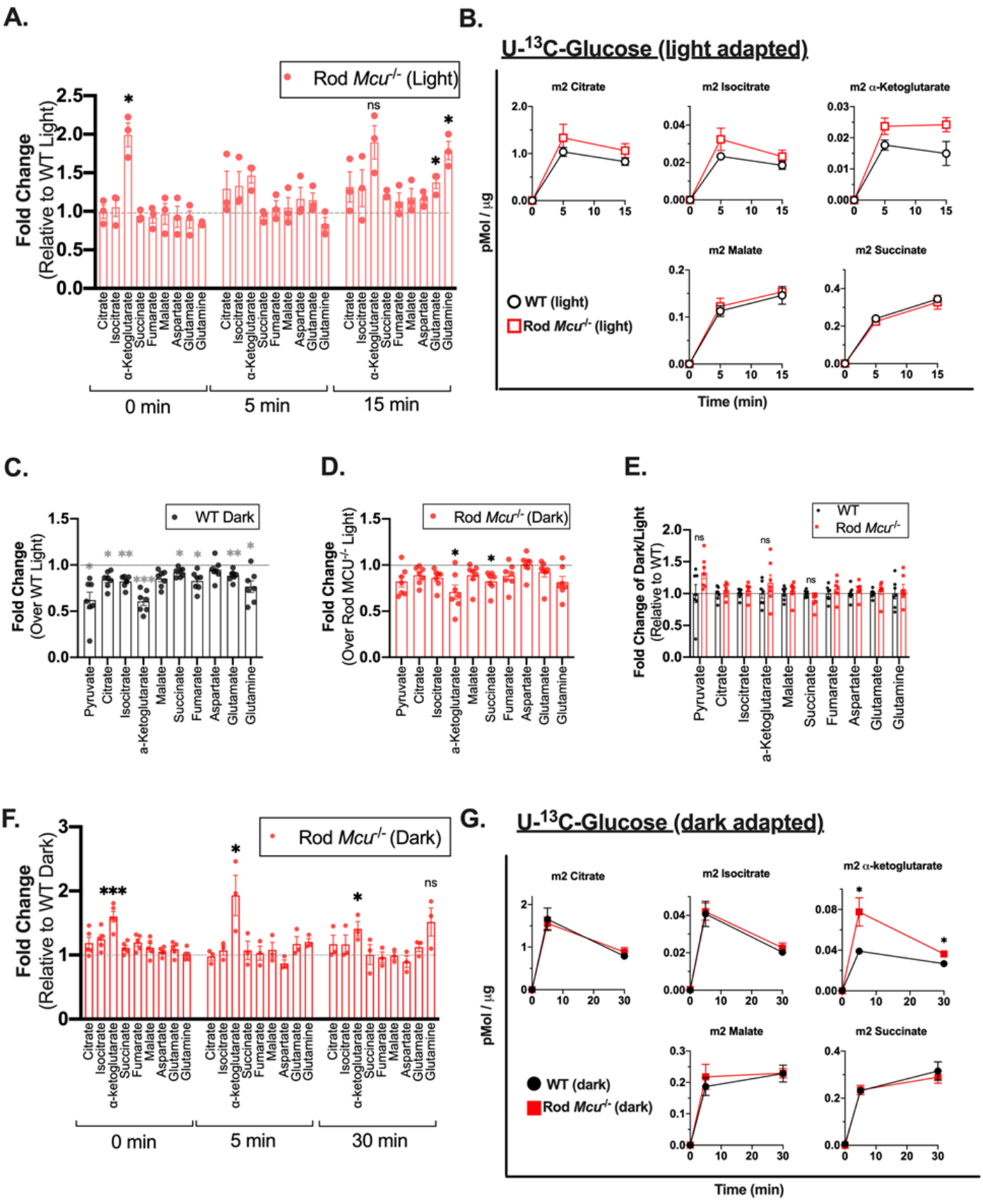
A.
Rod Mcu-/- (Light)
Fold Change
(Relative to WT Light)
Citrate
Isocitrate
α-Ketoglutarate
Succinate
Fumarate
Malate
Aspartate
Glutamate
Glutamine
0 min
5 min
15 min
B.
U-13C-Glucose (light adapted)
m2 Citrate
m2 Isocitrate
m2 α-Ketoglutarate
m2 Malate
m2 Succinate
pMol / µg
WT (light)
Rod Mcu-/- (light)
Time (min)
C.
WT Dark
Fold Change
(Over WT Light)
Pyruvate
Citrate
Isocitrate
a-Ketoglutarate
Malate
Succinate
Fumarate
Aspartate
Glutamate
Glutamine
D.
Rod Mcu-/- (Dark)
Fold Change
(Over Rod MCU-/- Light)
E.
WT
Rod Mcu-/-
Fold Change of Dark/Light
(Relative to WT)
F.
Rod Mcu-/- (Dark)
Fold Change
(Relative to WT Dark)
0 min
5 min
30 min
G.
U-13C-Glucose (dark adapted)
m2 Citrate
m2 Isocitrate
m2 α-ketoglutarate
m2 Malate
m2 Succinate
pMol / µg
WT (dark)
Rod Mcu-/- (dark)
Time (min)

Figure 3.5: Buildup of α-ketoglutarate in Rod *Mcu*$^{-/-}$ retinas is independent of light state.

A. Total metabolite levels in light-adapted Rod *Mcu*$^{-/-}$ retinas relative to WT (n=3 WT and 3 Rod *Mcu*$^{-/-}$ retinas per time point. Each time point used retinas from 3 different animals. *** indicates p<0.001 using Welch's t-test).

B. Time course of labeled metabolite accumulation in light-adapted WT and Rod *Mcu*$^{-/-}$ retinas incubated in U-^{13}C-glucose for 0, 5, and 15 minutes (n=3 WT and 3 Rod *Mcu*$^{-/-}$ retinas per time point. Each time point used retinas from 3 different mice. * indicates p<0.05 using Welch's t-test).

C. Total metabolite levels in dark-adapted WT retinas relative to light-adapted WT retinas (n=5 light adapted retinas and 7 dark adapted retinas, each from four different mice. * indicates p<0.05, ** indicates p<0.01, *** indicates p<0.001 using Welch's t-test).

D. Total metabolite levels in dark-adapted Rod *Mcu*$^{-/-}$ retinas relative to light-adapted Rod *Mcu*$^{-/-}$ retinas (n=6 light adapted retinas and 7 dark adapted retinas, each from four different mice. * indicates p<0.05 using Welch's t-test).

E. Change in metabolite abundance between darkness and light in Rod *Mcu*$^{-/-}$ retinas relative to WT retinas from Figures 4C and 4D. (n=5 light adapted WT retinas, 7 dark adapted WT retinas, 6 light-adapted Rod *Mcu*$^{-/-}$ retinas, and 7 light-adapted Rod *Mcu*$^{-/-}$ retinas, all ns using Welch's t-test).

F. Total metabolite levels in dark-adapted Rod *Mcu*$^{-/-}$ retinas relative to WT (n=4 WT and 5 Rod *Mcu*$^{-/-}$ retinas for t=0, n=3 WT and 3 Rod *Mcu*$^{-/-}$ retinas for t=5 and t=30. Each time point used retinas from at least 3 different animals. * indicates p<0.05, *** indicates p<0.001 using Welch's t-test).

G. Time course of dark-adapted WT and Rod *Mcu*$^{-/-}$ retinas incubated in U-^{13}C-glucose for 0, 5, and 30 minutes (n=3 WT and 3 Rod *Mcu*$^{-/-}$ retinas per time point. Each time point used retinas from 3 different animals. * indicates p<0.05 using Welch's t-test).

MCU-deficiency does not influence mouse rod photoresponses

We determined how much MCU normally contributes to the rod photoresponse recovery by recording *ex vivo* transretinal ERG responses from Rod *Mcu*$^{-/-}$ mice and WT controls in scotopic conditions (dim light). Dark-adapted flash responses of *Mcu*$^{-/-}$ rods are slightly but not significantly larger than controls (**Figure 3.6 A, B, and C**). The normalized flash response family plots superimposed over each other, indicating that the intensity to produce half-maximum response (a measure of sensitivity) of *Mcu*$^{-/-}$ rods is not significantly different from controls (**Figure 3.6 C, *inset***). A summary of the response parameters in the control and *Mcu*$^{-/-}$ rods is given in **Table 1**. There are no notable differences in the time to peak (T_p), integration time (T_{int}), and recovery time constant τ_{rec} of the flash response.

We next tested if Ca^{2+} sequestering through MCU affects light adaptation of rods. When illuminated, photoreceptors must adapt to the light exposure in order to retain the ability to respond. Ca^{2+} levels in the outer segment of photoreceptors modulate the activity of several proteins to mediate this light adaptation.[157–159] To test if Ca^{2+} sequestering through MCU has an effect on light adaptation of rods, we exposed retinas to a series of background light steps of

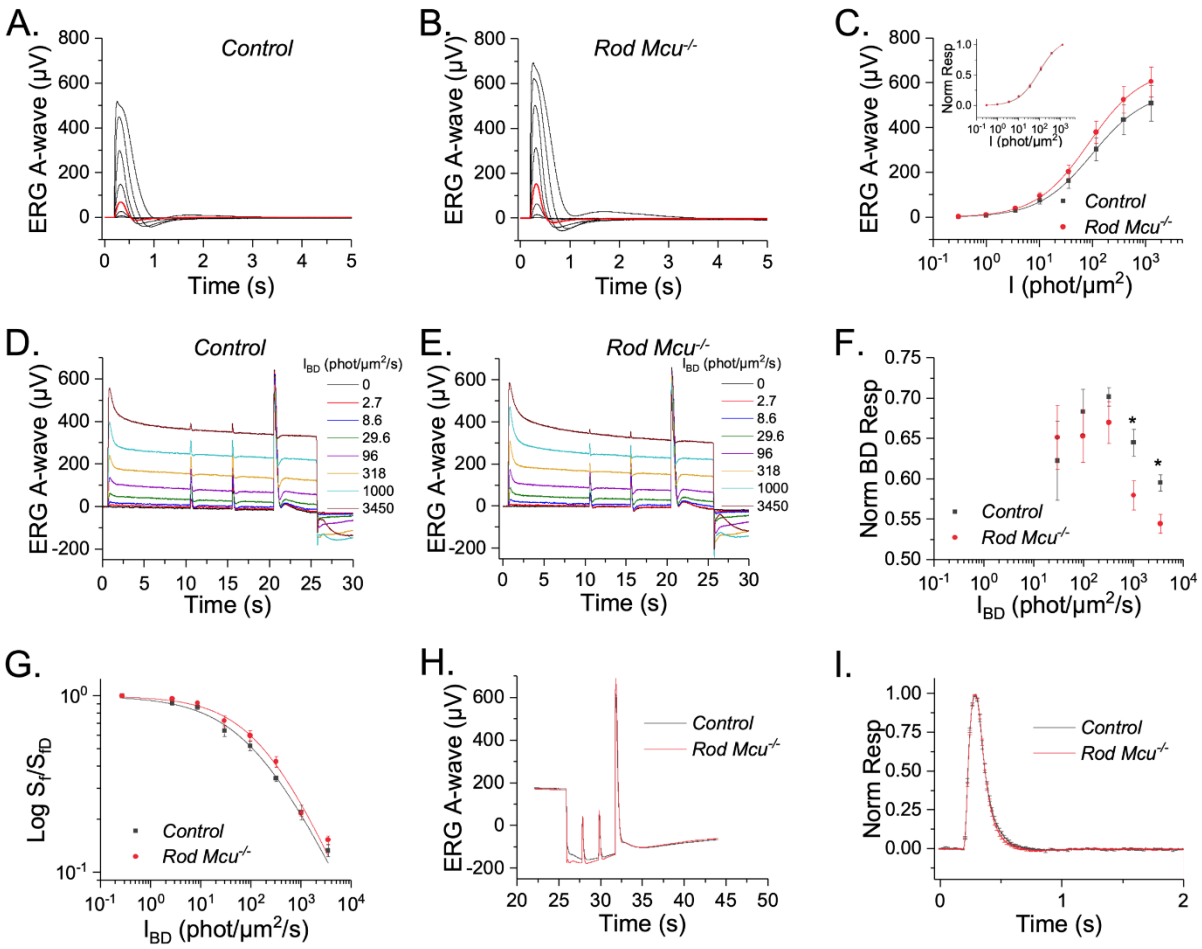

Figure 3.6: Mouse rods lacking Ca^{2+} uptake through MCU exhibit normal photoresponse

A, B. Flash response families of dark adapted *iCre*$^{+}$ (control; A) and *Mcu*$^{f/f}$ *iCre*$^{+}$ (Rod *Mcu*$^{-/-}$; B) mice from transretinal ERG recordings. Scotopic a-wave responses were recorded by a series of test flashes (1ms in duration) with intensities (in photons/μm^2) 0.3, 1, 3.5, 10.2 (red traces), 35.4, 117, 385, 1270.

C. Averaged rod responses (Mean ± SEM) from control (black) and Rod *Mcu*$^{-/-}$ mice (red) plotted as a function of flash intensity show only a marginal ($p>0.05$) difference in the response amplitude between these groups ($n=10$ for each). The solid lines represent curves fitted to the intensity response using the Naka-Rushton Function, $R/R_{max} = I/(I + I_{1/2})$. (Inset) Normalized intensity response curves showing no difference in sensitivity between control (black) and Rod *Mcu*$^{-/-}$ (red) mice.

D, E. ERG responses to steps of incremental background illumination of control (D) and Rod *Mcu*$^{-/-}$ mice (E) with subsequent responses to dim and saturating light flashes ($n=8$ for each).

F. The background light response at plateau, normalized to the peak of the initial background response, as a function of background light intensity. The plateau response for the two brightest backgrounds was significantly lower for the Rod *Mcu*$^{-/-}$ responses compared to these from controls ($n=8$ for each).

G. Light-adapted sensitivity, normalized to the corresponding dark-adapted value, plotted as a function of background light intensity. Solid lines represent curves fitted to the response plots using the Weber Fechner function. ($n=8$ for each).

H. Rod sensitivity during subsequent dark adaptation was estimated from ERG responses to dim flashes recorded at 2 s and 4 s after turning off a step of background light; averaged traces for control (black; $n=8$) and Rod *Mcu*$^{-/-}$ (red; $n=12$) retinas are shown. No notable differences in the kinetics of the dim flash response between control and *Mcu*$^{-/-}$ rods at both 2 s and 4 s time points for the two brightest background steps (1000 and 3450 photons/μm^2/s) were evident.

I. A representative plot for the flash responses recorded at 4s after turning off the highest background (3450 photons/μm^2/s) shows identical kinetics between control ($n=8$) and Rod *Mcu*$^{-/-}$ ($n=12$) responses.

increasing intensity. The peak response to background light of *Mcu*$^{-/-}$ rods was comparable to controls (**Figure 3.6D and E**). Notably, the background response plateau of *Mcu*$^{-/-}$ rods was lower than the controls and was significant for the two highest background light steps tested (**Figure 3.6F**). However, the light adapted sensitivity (S_f) remained largely unaffected in Rod *Mcu*$^{-/-}$ compared to the controls across all background light levels tested (**Figure 3.6G**).

MCU activity is controlled by multiple regulatory proteins that confer cooperativity to the channel so that it can robustly respond to changes in cytoplasmic Ca^{2+} [60,160]. In the previous experiments, all responses were in either the completely dark-adapted state or in steady-state light adaptation, with cytoplasmic Ca^{2+} being stable at high or low concentrations, respectively. We next examined if MCU modulates responses when photoreceptor intracellular Ca^{2+} levels are rapidly changing and when Ca^{2+} flux through MCU may be changing more dynamically. To do this, we presented test flashes to the retinas that were in the process of dark adapting. After turning off the background light, two test flashes were presented at 2 and 4 seconds, followed by a saturating light flash (**Figure 5H**). This allowed us to assess both flash response kinetics (**Figure 5I**) and sensitivity (**Table 2**). Both parameters were unaltered by the rod MCU deficiency.

	R_{max} (μV)	$I_{1/2}$ (phot/μm^2)	S_{fD} (μV/phot/μm^2)	t_p (ms)	t_{int} (ms)	τ_{rec} (ms)	I_o^* (phot/μm^2/s)	n^*
Control *(N=8)*	508 ± 79	101 ± 8	0.014 ± 0.001	136 ± 5	359 ± 16	65 ± 4	116 ± 17	0.61 ± 0.06
Rod **Mcu**$^{-/-}$ *(N=8)*	605 ± 67	100 ± 18	0.015 ± 0.001	141 ± 6	331 ± 18	65 ± 3	194 ± 37	0.69 ± 0.04
p value	0.36	0.94	0.63	0.50	0.28	0.96	0.08	0.3

Table 1: Dim Flash Response Sensitivity and Kinetics Parameters.

R_{max}, saturated response amplitude measured at the plateau; $I_{1/2}$, intensity required to produce half of the saturated response; S_{fD}, dark adapted sensitivity; t_p, time to peak of a dim flash response; t_{int}, integration time of the response; τ_{rec}, recovery time constant during response shut off; I_o, intensity required to decay the sensitivity to one half.

	S_f/S_{fD} (μV/phot/μm^2), I_{BD} (1000 Phot/μm^2), 2s	S_f/S_{fD} (μV/phot/μm^2), I_{BD} (1000 Phot/μm^2), 4s	S_f/S_{fD} (μV/phot/μm^2), I_{BD} (3450 Phot/μm^2), 2s	S_f/S_{fD} (μV/phot/μm^2), I_{BD} (3450 Phot/μm^2), 4s
Control *(N=8)*	1.2 ± 0.1	1.3 ± 0.1	0.96 ± 0.05	1.1 ± 0.04
***Rod* Mcu$^{-/-}$** *(N=12)*	1.3 ± 0.1	1.4 ± 0.1	0.9 ± 0.05	1.2 ± 0.06
p value	0.46	0.45	0.66	0.73

Table 2. Normalized sensitivity at 2s and 4s time points after turning off the background light step. S_f/S_{fD}, Normalized fractional sensitivity; I_{BD} , Intensity of the background illumination

MCU-mediated mitochondrial Ca^{2+} uptake does not contribute to the small photoresponse seen in *Nckx1*$^{-/-}$ mice

The rod Na^+/Ca^{2+}, K^+ exchanger (NCKX1) is the only known route for Ca^{2+} clearance from the outer segment plasma membrane, and it is thought to be the driver of Ca^{2+} clearance from this compartment. Since MCU expression in mouse rods is extremely low, its contribution to cytosolic Ca^{2+} clearance may be small compared to that of NCKX1. To unmask any possible modulation of the rod photoresponse by MCU, we investigated the effect of MCU loss on the rod photoresponse in mice lacking NCKX1. NCKX1-deficiency compromises Ca^{2+} extrusion in the rod outer segments and it delays photoresponse recovery following a flash stimulus.[150] If the residual Ca^{2+} extrusion in NCKX1-deficient rods is mediated by MCU, then it would be expected that the subsequent deletion of MCU would further suppress or completely block Ca^{2+} extrusion, causing a further delay in photoresponse recovery and suppressing light adaptation.

We recorded transretinal ERG responses from *Nckx1*$^{-/-}$ control and *Nckx1*$^{-/-}$ Rod *Mcu*$^{-/-}$ mice (**Figure 3.7A and B**). The responses of *Nckx1*$^{-/-}$ *Mcu* $^{-/-}$ double knockout rods are significantly smaller compared to *Nckx1*$^{-/-}$ controls (**Figure 3.7C**). However, the sensitivity and kinetics of the flash response are comparable in *Nckx1*$^{-/-}$ *Mcu* $^{-/-}$ rods and control *Nckx1*$^{-/-}$ rods (**Figure 3.7C inset and D**, respectively). This indicates that Ca^{2+} sequestration by MCU does not modulate the rod photoresponse recovery even in the absence of the dominant NCKX1 Ca^{2+} extrusion mechanism. Table 3 summarizes the rod response properties of *Nckx1*$^{-/-}$ controls and *Nckx1*$^{-/-}$

Rod *Mcu*$^{-/-}$ mice. Overall, these results indicate that Ca^{2+} uptake mediated by MCU does not significantly influence the rod photoresponse.

	R_{max} (μV)	$I_{1/2}$ (phot/μm^2)	S_{fD} (μV/phot/μm^2)	t_p (ms)	T_{int} (ms)	τ_{rec} (ms)
Nckx1*$^{-/-}$ *Control *(N=10)*	19 ± 2	22.8 ± 1.4	0.02605 ± 0.001	312.9 ± 19	1564 ± 83	441.3 ± 52
***Nckx1*$^{-/-}$ *Rod* Mcu$^{-/-}$** *(N=9)*	9.7 ± 1	23.2 ± 2	0.02555 ± 0.002	367.7 ± 24	1687 ± 81	501 ± 103
p value	0.0005	0.87	0.86	0.09	0.3	0.6

Table 3: Dim Flash Response Sensitivity and Kinetics Parameters.

R_{max}, saturated response amplitude measured at the plateau; $I_{1/2}$, intensity required to produce half of the saturated response; S_{fD}, dark adapted sensitivity; t_p, time to peak of a dim flash response; t_{int}, integration time of the response; τ_{rec}, recovery time constant during response shut off

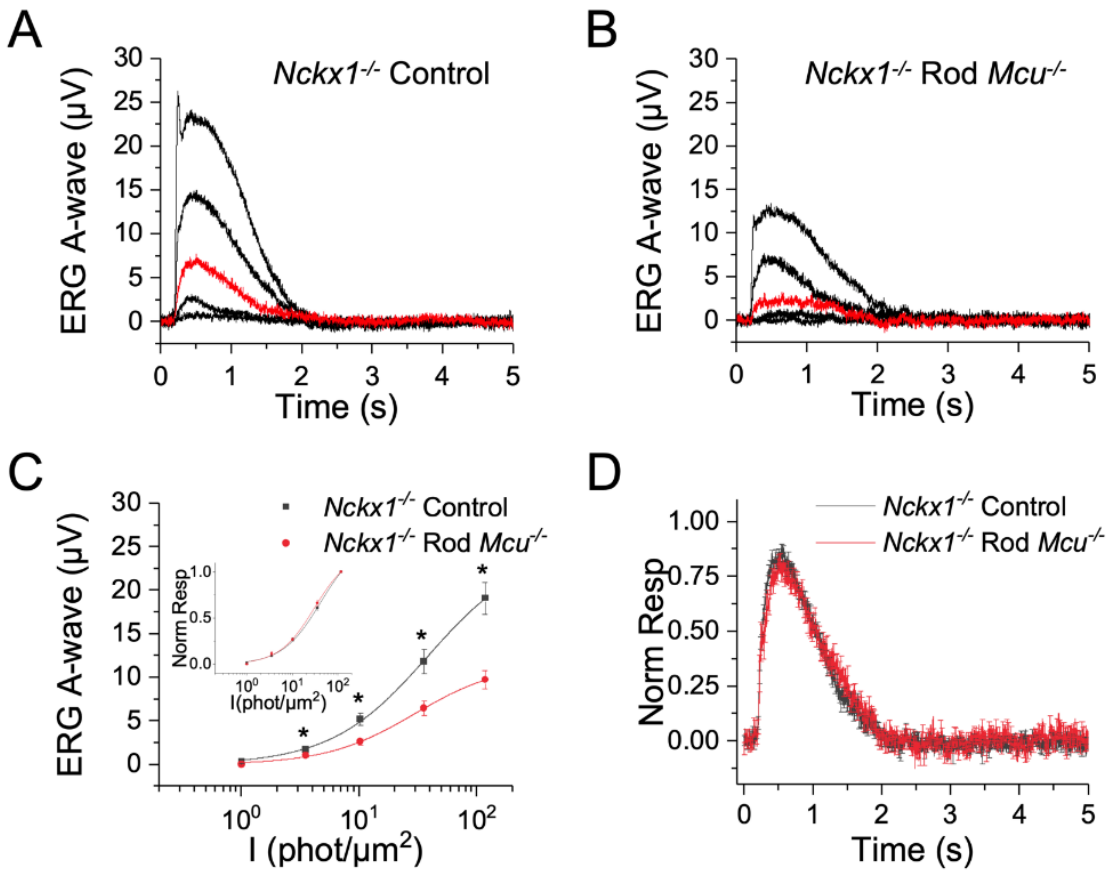

Figure 3.7: MCU-mediated mitochondrial Ca^{2+} uptake does not modulate the photoresponses in Nckx1$^{-/-}$ mice

A, B) Flash response families of dark adapted *Nckx1*$^{-/-}$ iCre^{+} (*Nckx1*$^{-/-}$ control; A) and *Nckx1*$^{-/-}$ *Mcu*$^{f/f}$ iCre^{+} double knockout (*Nckx1*$^{-/-}$ Rod *Mcu*$^{-/-}$; B) mice from transretinal ERG recordings. Scotopic a-wave responses were recorded by a series of test flashes (1 ms in duration) with intensities (in photons/μm^2) 1, 3.5, 10.2 (red traces), 35.4, 117.

C. Averaged rod responses (Mean ± SEM) from *Nckx1*$^{-/-}$ control (black; n=10) and *Nckx1*$^{-/-}$ Rod *Mcu*$^{-/-}$ mice (red; n=9) plotted as a function of flash intensity show a substantial reduction of the response amplitude in the double knockouts as compared to the controls. However, the sensitivity of the rods (estimated their normalized intensity response functions; Inset) remained unchanged between *Nckx1*$^{-/-}$ control (black) and *Nckx1*$^{-/-}$ Rod *Mcu*$^{-/-}$ (red) mice.

D. The kinetics of the dim flash response were not affected in the *Nckx1*$^{-/-}$ Rod *Mcu*$^{-/-}$ mice (n=9); red trace) as compared to *Nckx1*$^{-/-}$ controls (n=10; black trace).

Discussion

Photoreceptors have abundant mitochondria in the compartment of the cell between the nucleus and the outer segment that can influence cytosolic Ca^{2+} pools.[146] Photoreceptors also depend on Ca^{2+} homeostasis for proper function and viability.[78,114] Despite this, we find that loss of the presumptive primary Ca^{2+} channel for mitochondrial Ca^{2+} uptake (MCU) is tolerated surprisingly well by photoreceptors. MCU-deficient photoreceptors appear healthy, their TCA cycle activity is largely unaltered, and the photoresponse is preserved. In cones from global *mcu*$^{-/-}$ zebrafish, Ca^{2+} uptake is reduced in a significant population of mitochondria. However, some mitochondria still take up Ca^{2+} in the absence of MCU. Consistent with this result, we found that both WT and *mcu*$^{-/-}$ retinas have a population of cone mitochondria which still take up Ca^{2+} even in the presence of the MCU inhibitor Ru360. This is similar to what has been observed in non-synaptic brain mitochondria isolated from *Mcu*$^{-/-}$ mice, in which uptake of Ca^{2+} into mitochondria was not blocked but instead occurred at a slower rate compared to controls.[144] This suggests that neuronal tissue like retina and brain might have an alternative mitochondrial Ca^{2+} uptake pathway. While alternative mitochondrial Ca^{2+} uptake pathways have been proposed, they remain understudied since the discovery of MCU.[161–165] The finding that cone photoreceptor mitochondria can take up Ca^{2+} in the absence of MCU better contextualizes the observed low expression of MCU in photoreceptors. Photoreceptors may maintain low MCU expression in favor of this alternative uptake pathway. Overall, the subtlety of phenotypes exhibited by *Mcu*$^{-/-}$ photoreceptors, coupled with the observation that these cells express very low levels of MCU, indicate that MCU is remarkably dispensable for photoreceptor function.

Rod *Mcu*$^{-/-}$ mouse retinas are metabolically quite normal and exhibit only a mild accumulation of α-ketoglutarate (**Figure 3.4 and 3.5**). We also observed that α-ketoglutarate trended towards accumulating to higher levels in retinas from *mcu*$^{-/-}$ zebrafish **(Figure 3.2A**). α-ketoglutarate participates in multiple mitochondrial and cytosolic reactions, making it difficult to pinpoint the exact reaction that is altered by loss of MCU in rods which leads to this accumulation. This is not the first time an accumulation of α-ketoglutarate has been observed to accompany MCU loss, as a similar accumulation of α-ketoglutarate occurs in *Mcu*$^{-/-}$ fibroblasts. These fibroblasts have defects in glucose metabolism upstream of α-ketoglutarate, and the accumulated α-ketoglutarate was attributed to upregulated glutaminolysis.[166] However, *Mcu*$^{-/-}$ photoreceptors exhibit no defects in glucose metabolism upstream of α-ketoglutarate and we see no evidence

for altered synthesis of glutamate or glutamine in retinas supplied with U-^{13}C-glucose, which suggests a different mechanism is responsible.

An alternative possibility is that α-ketoglutarate levels increase after loss of MCU due to decreased Ca^{2+} stimulation of α-KGDH. When α-KGDH is bound to Ca^{2+}, its K_m for α-ketoglutarate is lowered.[35,96] We previously observed that increased matrix Ca^{2+} in zebrafish cone photoreceptors lowers the steady-state concentration of α-ketoglutarate, presumably because less substrate is needed to activate α-KGDH due to its lowered K_m [36]. Since steady-state α-ketoglutarate levels increase in MCU-deficient retinas, it is reasonable to hypothesize that the opposite occurs: more substrate is needed to activate α-KGDH due to its increased K_m when one route of Ca^{2+} entry into the matrix (MCU) is shut down (**Figure 3.5**). However, our measurements of matrix Ca^{2+} show that the overall basal matrix Ca^{2+} levels are unaltered in cone mitochondria lacking MCU (**Figure 3.1E and 3.1F**). We suggest the following possible explanations for elevated α-ketoglutarate levels in the absence of a detectable change in matrix Ca^{2+}:

1) matrix Ca^{2+} levels are decreased in rods lacking MCU but not in cones from global *mcu*$^{-/-}$ zebrafish

2) loss of MCU results in subtle changes in matrix Ca^{2+} microdomains which influence α-KGDH activity but that we are unable to detect using our imaging methods

3) α-ketoglutarate levels are affected by an unknown, matrix Ca^{2+}-independent process.

Mcu$^{-/-}$ rods exhibit a normal photoresponse with no change in the sensitivity and kinetics of the flash response and light adaptation (**Figure 3.6**). Since mitochondrial Ca^{2+} uptake via MCU is regulated cooperatively by several regulatory proteins, we also investigated if MCU might play a role in modulating the photoresponse only when intracellular Ca^{2+} levels are more rapidly changing, such as when photoreceptors are adapting to background light or during the subsequent recovery back to their dark adapted state. However, *Mcu*$^{-/-}$ rods did not display a change in photoresponse parameters even while dark adapting following exposure to background light. This lack of phenotype may reflect the extremely low expression of MCU in mouse rods relative to the more dominant Ca^{2+} clearance pathways such as NCKX1.

To determine if MCU might play a small role in clearing Ca^{2+} that is difficult to detect in the presence of other Ca^{2+} clearance pathways, we compared photoresponses of single knockout *Nckx1*$^{-/-}$ mice and double knockout *Nckx1*$^{-/-}$ Rod *Mcu*$^{-/-}$ mice. *Nckx1*$^{-/-}$ mice maintain a small photoresponse and are remarkably slow to degenerate, which indicates that they are able to clear a small amount of outer segment Ca^{2+} through a not yet understood pathway.[150] We hypothesized that if the small photoresponse observed in *Nckx1*$^{-/-}$ mice were due to Ca^{2+} sequestering via MCU, that this response would be ablated in the double knockout *Nckx1*$^{-/-}$ Rod *Mcu*$^{-/-}$ mice. However, the sensitivity, flash response kinetics and even light adaptation were unchanged in *Nckx1*$^{-/-}$ Rod *Mcu*$^{-/-}$ mice compared to *Nckx1*$^{-/-}$ controls, which indicates that mitochondrial Ca^{2+} uptake via MCU does not contribute substantially to outer segment Ca^{2+} clearance or photoresponse recovery (**Figure 3.6**). It remains a possibility that mitochondrial Ca^{2+} uptake through an alternative pathway contributes to the small photoresponse that is seen in *Nckx1*$^{-/-}$ Rod *Mcu*$^{-/-}$ mice. We did observe a reduction in the flash response amplitude in *Nckx1*$^{-/-}$ Rod *Mcu*$^{-/-}$ as compared to Nckx1$^{-/-}$ rods. The reason for this remains unclear, although it could be due to a possible degeneration in the double knockout retinas. Overall, we find that MCU does not play a significant role in Ca^{2+} feedback mechanisms during the photoresponse.

Maintaining intracellular Ca^{2+} homeostasis is vital for many cell types, including photoreceptors. While most cells are thought to buffer mitochondrial Ca^{2+} solely through MCU, we find that both rod and cone photoreceptors have limited MCU expression. In the absence of MCU, cone mitochondrial Ca^{2+} uptake is diminished but not entirely ablated. We found that this fraction of MCU-mediated mitochondrial Ca^{2+} uptake has a very limited effect on modulating metabolism and no role in modulating metabolic output and the photoresponse. This does not mean that mitochondria do not play a role in modulating photoreceptor function by buffering intracellular Ca^{2+}, since it is possible that the fraction of mitochondrial Ca^{2+} uptake which is retained by photoreceptors lacking MCU is sufficient to regulate metabolism and modulate phototransduction. However, we can conclude that MCU does not facilitate Ca^{2+} regulation of these processes. We find that MCU is surprisingly dispensable for photoreceptor function, possibly in favor of an alternative mitochondrial Ca^{2+} uptake pathway.

Acknowledgements

This chapter represents work that is currently under review at *eLife*. The co-authors on this work are Celia M. Bisbach (lead author), Deepak Poria, Whitney M. Cleghorn, Fatima Abbas, Frans Vinberg, Vladimir J. Kefalov, James B. Hurley, and Susan E. Brockerhoff. We would like to thank Stanley Kim from the South Lake Union Aquatics Core for assisting in maintaining our zebrafish colony. Work in the lab of S.B. was funded by NIH grants EY026020 and EY028645. Work in the lab of J.B.H. was funded by NIH grants EY06641 and EY017863. Work in the lab of V.J.K. was funded by NIH grants EY027387 and EY026675; EY02687 to Washington University, Department of Ophthalmology and Visual Sciences, and by Research to Prevent Blindness. C.M.B. received funding from the NIH grant F31EY031165.

Materials and Methods

Animal care. Mice were maintained and used in accordance with the guidelines of experimental protocols approved by the Institutional Animal Care and Use Committees of Washington University in St. Louis and the University of Washington in Seattle. At Washington University in St. Louis, mice were kept under a 12h light/dark cycle and given free access to food and water. At the University of Washington, mice were housed in the UW Medicine SLU 3.1 vivarium, where they experienced a 6AM-9PM (fall-winter) and 7AM-9PM (spring-summer) light/dark cycle and had free access to food and water. In figures 3 and 4, "WT" animals are *Mcu*$^{fl/fl}$ iCre- littermates. In figure 5, "Control" animals are iCre+ mice in which *Mcu* is not floxxed. In figure 6, "Control" animals are *Nckx1*$^{-/-}$ single knockouts. In figures 5 and 6, the control and experimental mice were obtained from separate lines derived from common parents. iCre-75 mice were a gift from the lab of Ching Kang (Jason) Chen.[153] MCU^{fl} mice (B6;129S-*Mcu*$^{tm1.1Jmol}$/J) were obtained from Jackson Labs. The *Nckx1*$^{-/-}$ mice used in this study were generated as described in a previous publication.[150] Mice were maintained on a C57BL/6J background. Mice used for histology were 6 and 11 months of age (6 months of age is shown in Figure 1), and mice used for metabolic analysis were between 5-9 months of age. Mice used for ERG analysis were 6 to 8 weeks of age. Equal numbers of male and female mice were used in this study.

Zebrafish were maintained and used in accordance with the guidelines of experimental protocols approved by the University of Washington in Seattle and University of Utah Institutional Animal Care and Use Committees. All fish used in this analysis were maintained in the University of Washington South Lake Union aquatics facility or the Centralized Zebrafish Animal Resource (CZAR) at the University of Utah at 27.5°C on a 14/10 h light/dark cycle and were maintained in the $Roy^{-/-}$ genetic background. All wild-type fish (WT) used in analysis were age-matched siblings to CRISPR-generated *mcu*$^{-/-}$ zebrafish. Fish used for slice preparation were between 7 and 11 months of age. Fish used for metabolic analysis were 11 months of age, fish used in ERG analysis were 7 months of age, and fish used for retinal morphology analysis were 11 months of age. Equal numbers of male and female fish were used.

Immunoblotting. Protein was extracted by homogenizing in RIPA buffer (150 mM NaCl, 1.0% Triton X-100, 0.5% sodium deoxycholate, 0.1% SDS, 50 mM Tris, pH 8.0) and run on 14% polyacrylamide gels. After running, gels were transferred onto PVDF membranes (Millipore, IPFL00010) and briefly washed with PBS. Primary antibodies were diluted in blocking buffer (LI-COR, 927-40000) and incubated overnight on blots at 4°C. Membranes were washed twice with PBS containing 0.1% Tween-20 and once with PBS, then incubated with secondary antibodies diluted 1:5000 in blocking buffer for 1 hr at RT and washed again before imaging. Membranes were imaged and bands were quantified using the LI-COR Odyssey CLx Imaging System (RRID:SCR_014579). Primary antibodies used: PDH E1 subunit (Abcam Cat# ab110334, RRID:AB_10866116), P-PDH (EMD Millipore Cat# ABS204, RRID:AB_11205754), mtCO1 (Abcam Cat# ab14705, RRID:AB_2084810), SDHB (Abcam Cat# ab14714, RRID:AB_301432), and Cell Signaling MCU (Cell Signaling Technology Cat# 14997, RRID:AB_2721812), custom MCU antibody (ref 36). All primary antibodies were used at 1:1000, with the exception of the custom MCU antibody which was used at 1:100. Secondary antibodies used: IRDye 800CW donkey anti-rabbit IgG (H + L) (LI-COR Biosciences, 925-32213, RRID: AB_2715510); IRDye 680RD donkey anti-mouse IgG (H + L) (LI-COR Biosciences, 925-32212, RRID: AB_2716622); IRDye 680RD donkey anti-rabbit IgG (H + L) (LI-COR Biosciences, 925-68073, RRID: AB_2716687); IRDye 800CW goat anti-mouse IgG (H + L) (LI-COR Biosciences, 925-32210, RRID: AB_2687825).

Immunohistochemistry. For best immunohistochemistry results, mice were perfused with fixative according published methods.[167] Briefly, PBS was placed in a 37°C water bath and all fixative tubing was flushed repeatedly with PBS to clear any bubbles. Mice were anaesthetized using 270 mg/kg of nebutol. Mice were taped to a dissection board and open-heart surgery was

performed in order to insert the perfusion needle into the left ventricle. The right atrium was snipped, and PBS was perfused through the mouse using a peristaltic pump until the outflow was clear. Then, room temperature 4% PFA (prepared from 16% PFA diluted in PBS) was perfused through the mouse. After fixation, eyes were carefully cut out with curved dissection scissors, the sclera was cut off, and eyes were stored in 4% PFA for 2 hours. Eyes were then rinsed with PBS, and moved through a sucrose gradient of 5%, 10%, 20%, and 30% sucrose (eyes were transferred to increasing concentrations of sucrose each time they sank to the bottom of the tube). Eyes were embedded in O.C.T. compound and 20 µm sections were cut using a Leica cryostat. For immunostaining, sections were rehydrated with PBS for 10 minutes and blocked in Normal Goat Serum (NGS) for 1h. Primary antibodies were diluted in NGS and incubated on sections overnight at 4°C in a humidified chamber. Sections were washed three times with PBS, and secondary antibodies were diluted in PBS and incubated on sections for 1h at room temperature. Sections were washed 3x with PBS, with the middle wash containing 5uM Hoechst nuclear stain diluted in PBS (Hoechst 33342, Trihydrochloride, Trihydrate stain (ThermoFischer, H3570). Slides were mounted using Fluoromount (Southern Biotech Cat#:0100-01) and imaged using an Olympus FV1000 Confocal microscope. Antibodies and stains used were: mtCO1 1:500 (Abcam Cat# ab14705, RRID:AB_2084810); MCU 1:2000 (Cell Signaling Technology Cat# 14997, RRID:AB_2721812); PNA 1:200 (after suspending at a concentration of 1 mg/mL in H20) (Lectin PNA Alexa Fluor 647 conjugate, ThermoFischer Cat# L32460); Goat anti-Rabbit IgG (H+L) Alexa Fluor 633 (Thermo Fisher Scientific, Cat# A-21070, RRID AB_2535731; Goat Anti-Mouse IgG H&L Alexa Fluor 488 (Abcam, ab150113, RRID:AB_2576208).

Isotopic Labeling. Krebs-Ringer bicarbonate (KRB) buffer (98.5 mM NaCl, 4.9 mM KCl, 1.2 mM KH_2PO_4 1.2 mM $MGSO_4$-$7H_2O$, 20 mM HEPES, 2.6 mM CaCl-$2H_2O$, 25.9 mM $NaHCO_3$) optimized for isotopic labeling experiments in retinas was used in these experiments. Mice were euthanized by awake cervical dislocation and eyes were rapidly enucleated into a dish of Hank's Buffered Salt Solution (HBSS; Gibco, Cat#: 14025-076). Zebrafish were euthanized using an ice bath and eyes were removed and placed in a dish of KRB + 5mM U-13C Glucose. For flux measurements, retinas were placed in pre-warmed KRB containing D-[U-^{13}C]-glucose (Cambridge Isotope Laboratories, CLM-1396). Retinas were incubated for the specified time points at 37°C (mouse) or 28°C (fish) at 5% CO_2 and room oxygen, then washed twice in ice-cold PBS and flash frozen in liquid nitrogen. For mouse dark-adapted experiments, mice were dark-adapted for a minimum of 18 hours. Samples were collected exactly as above, but in

complete darkness under an infrared light using night vision goggles. For zebrafish dark-adapted experiments, zebrafish were dark adapted for 18 hours and samples were collected under dim red light.

Mass Spectrometry Sample Preparation. Metabolites were extracted from retinas using ice-cold 80% MeOH. 150 µL extraction buffer was added to each sample and tissue was disrupted by sonication. Samples were then spun at maximum speed, the supernatant transferred to a new tube, and the pellet saved for protein quantification. The supernatant was lyophilized at room-temp until dry. Extracted metabolites were derivatized using a two-step process: 1) 10 µL of 20 mg/mL Methoxyamine HCl (Sigma, Cat#: 226904) dissolved in pyridine (Sigma, Cat#: 270970) was added and samples were incubated at 37°C for 90 minutes, then 2) 10 µL of *tert*-butyldimethylsilyl-N-methyltrifluoroacetamide (Sigma, Cat#: 394882) was added and samples were incubated at 70°C for 90 minutes. Metabolites were analyzed on an Agilent 7890/5975C GC-MS using selected-ion monitoring methods described in previous work.[115] Peaks were manually integrated using MSD ChemStation software (Agilent), and correction for natural isotope abundance was performed using Isocor software.[168] Raw signals for each metabolite were converted to molar amounts using metabolite standard curves which were run alongside each experiment. Molar amounts were normalized to the total amount of protein (determined using a BCA assay) for each sample to determine the molar amount per µg of cellular protein.

Live larval imaging of mito-GCaMP3. Larvae were maintained in embryo media containing 0.0003% 1-phenyl 2-thiourea (PTU, Sigma-Aldrich P7629) starting at 20 h postfertilization for confocal imaging. Larvae were analyzed at 6 days postfertilization (dpf) by embedding in 0.5% low melting point agarose containing embryo media with 0.02% (w/v) Tricaine (Sigma-Aldrich, E10521). The agarose was submerged in embryo media containing 0.0003% PTU and 0.02% (w/v) tricaine. Imaging was performed using an Olympus FV1000 with a 40x water objective in conjunction with Olympus FluoView FV10-ASW software (RRID:SCR_014215). The excitation/emission wavelengths used for mito-GCaMP3 were 488/510 nm. Images of total eye mitochondrial clusters were collected at a z-depth of 2 µm, and blinded quantification was performed using ImageJ + Fiji software (SCR_002285).

Retinal slice imaging of GCaMP3 and mito-GCaMP3. Slices were prepared as described previously.[146] For basal mito-GCaMP3 determination, 15 z-slices of 2 µm thickness were collected every 30 s. Retinas were incubated in KRB (containing 2 mM $CaCl_2$) for 5 min, then the chamber was injected with ionomycin (Sigma, 407950) to a final concentration of 5 µM

(prepared in DMSO, final concentration of 0.1%) for another 5 min of image collection. An excess of EGTA (5 mM) was then injected and images were collected for another 5 min. For mitochondrial Ca^{2+} uptake experiments, retinas were incubated in KRB containing KB-R7943 (100 µM) for 10 minutes. After this preincubation, baseline measurements of mito-GCaMP3 fluorescence were taken for 3 frames (30 seconds each) before treatment with sildenafil (25 µM) for a total of 15minutes of imaging.

For analysis of both experiments, any mitochondrial clusters where the maximum fluorescence signal was completely saturated were excluded. Analysis was conducted blinded (masked) to sample identity. The excitation/emission wavelengths used for mito-GCaMP3 were 488/510 nm. Timelapses were analyzed using ImageJ + Fiji software (SCR_002285) and were corrected for X-Y drift using the MultiStackReg plugin of ImageJ. Fixed ROIs were used to quantify average fluorescence signal across the mitochondrial cluster at every time point. To determine baseline Ca^{2+}, we used the equation $[Ca^{2+}] = K_D \times \frac{\theta}{1-\theta}$, where $\theta = \frac{F_0 - F_{min}}{F_{max} - F_{min}}$ to approximate $[Ca^{2+}]_{mito}$. F_0 is the average basal fluorescence, F_{max} is maximum fluorescence upon ionomycin addition, and F_{min} is the baseline fluorescence upon EGTA addition. We used an approximation for the K_D of GCaMP based on other published experiments (345 nM) in the calculation.[86]

Mouse Electrophysiology. Mice were dark adapted overnight prior to the day of experiment and were euthanized by CO_2 incubation. Eyes were enucleated under dim red light immediately after euthanasia followed by dissection under infrared illumination. The retinas were gently detached from posterior eye cups and were stored in dark in a dish containing oxygenated Ames medium at room temperature until recording. Recordings were conducted using previously described methods.[128] The retinas were mounted photoreceptors facing up in a closed chamber and were continuously superfused with oxygenated Ames medium (Sigma) at a flow rate of 3-5 ml/minute. For isolating the a-wave of ERG, 50µM DL-AP_4 (Tocris) and 100µM $BaCl_2$ (Sigma) were included in the Ames medium. The recording chamber was maintained at 35-36°C and retinas were allowed to adapt to the chamber temperature for at least 15 minutes before experiments. Ex-vivo transretinal ERG recordings were made in scotopic conditions by presenting light flashes produced by LEDs (Thor Labs). The ERG signals were amplified using a differential amplifier (Warner Instruments), low-pass filtered at 300Hz (Krohn Hite Corp.), digitized using digidata 1440 (Molecular Devices), and were recorded at a sampling frequency of 10kHz using pClamp 10 software.

Zebrafish Electrophysiology. Zebrafish were approximately 7 months of age for all electrophysiology experiments. Zebrafish were briefly dark adapted (~30 min), before euthanasia by ice water immersion. Eyes were enucleated into Modified Salamander Ringer's solution (110 mM NaC, 2.5 mM KCl, 1.0 mM CaCl2, 1.6 mM MgCl2, 10.0 mM HEPES, 10.0 mM Glucose) with pH adjusted to 7.8 with NaOH. The eyes were hemisected and retinas isolated from the eyecup. All procedures after the dark adaptation were performed under dim red light. To ensure ex vivo ERG signal was pre- dominantly cone responses, dark adaption was limited to ~30 min to allow cone photopigment regeneration but not provide enough time for full rod photopigment regeneration, and experiments were carried out during the day (between 11AM and 4PM) when rod contributions to retinal responses are at their lowest due to the circadian regulation of photoreceptor biology in the zebrafish retina. *Ex vivo* ERG recordings were performed as described previously.[128,129] Isolated retinas were mounted photoreceptor side up onto the specimen holder and perfused with Modified Salamander Ringer's solution, supplemented with 40 µM DL-AP4 (Tocris Bioscience) and 40 µM CNQX (Tocris Bioscience) to isolate the photoreceptor component of the ERG signal (a-wave). The rate of perfusion was ~5 mL/min and the experiments were conducted at room temperature (~23°C). ERG signal was first amplified (100×) and low-pass filtered at 300 Hz by a differential amplifier (DP-311, Warner Instruments), and data was further amplified (10×) and acquired at 10KHz using an integrated amplifier/digitizer (IPA, Sutter Instrument, CA). A High Power LED light source (Solis-3C, Thorlabs, Newton, NJ), with filter for red light (630 nm, FWHM bandwidth 69 nm, FF01-630/69-25, Semrock, Rochester, NY) and LED driver (DC2200, Thorlabs) were used to provide the flashes of light stimuli, durations ranged from 5 to 100 ms. The SutterPatch soft- ware (SutterPatch v1.1.2, Sutter Instrument, CA) drove both stimulus generation and data acquisition via the IPA amplifier's analogue output and input, respectively. Light stimuli were calibrated before experiments using a calibrated photodiode (FDS100-CAL, Thorlabs, Newton, NJ) and flash intensities converted to photons/µm^2. Data analysis, including statistical analysis and figure preparation, was performed with GraphPad v 8.00 (for Windows, GraphPad Software, CA, USA). Normalized responses were calculated for each retina by dividing the response amplitude data by the maximal amplitude measured at the peak/plateau of the response to the brightest flash. To quantify the gain of phototransduction activation, we fitted the Lamb–Pugh model to the initial leading edge of the dim flash response for each retina, and compared the average amplification constant (A) between WT and *mcu*$^{-/-}$ siblings.[169]

Chapter 4: Chronic mitochondrial stress triggers mitochondrial movement in photoreceptors

Introduction

Mitochondria are necessary for eukaryotic life. They supply essential metabolic intermediates and ATP, modulate cellular signals including Ca^{2+} and reactive oxygen species (ROS), and control the cellular activation of apoptosis. Accordingly, it is imperative for a cell to protect its mitochondria from damage or stress throughout its lifetime. Dysfunctional mitochondria are associated with a range of diseases that affect a variety of tissues, including neurodegenerative diseases, cardiovascular diseases, and diabetes.[4,5,7]

The causes of mitochondrial stress and dysfunction are numerous.[12] Excessive mitochondrial matrix Ca^{2+} causes mitochondrial swelling and can lead directly to cell death via opening of the mitochondrial permeability transition pore.[44] Accumulation of mitochondrial DNA (mtDNA) mutations and inability to transcribe and translate mtDNA impairs function of the electron transport chain, compromising ATP production and mitochondrial membrane potential.[170] The bioenergetic state of a cell is also an important determinant of mitochondrial stress, as both deficiency and surplus of mitochondrial fuels are associated with mitochondrial dysfunction.[171] In many mitochondrial stressors, damage to mitochondria is mediated ROS that the mitochondria themselves generate.[41,172,173] While low levels of ROS are thought to be an important cellular signal that allows cells to adapt to environmental changes, chronically high levels of ROS can damage mitochondrial DNA, proteins, and lipids.[174,175]

Mitochondrial stress is often associated with a loss of motility. Excess ROS can trigger an arrest of mitochondrial movement in hippocampal neurons and skeletal muscle.[18,19] Increases in mitochondrial matrix Ca^{2+} are also associated with movement arrest in hippocampal neurons.[20] When mitochondrial membrane potential is lost, mitochondrial movement is compromised because the recruitment of Parkin to mitochondria targets transport proteins for degradation.[21,22]

However, mitochondrial movement is not always blocked in response to stress. Mild, chronic stress in neurons has been shown to induce release of the mitochondrial anchoring protein syntaphilin, enhancing the movement of damaged mitochondria.[23,176] Syntaphilin isoforms are primarily expressed in neural tissue, but have been detected in some cancers where a similar phenomenon is observed in response to stress.[177] Additionally, collapse of the mitochondrial

network around the nucleus (perinuclear clustering) has been observed in response to hypoxia and inhibition of the proteasome.[24,25]

Most neurons are especially sensitive to mitochondrial stress, as they rely on trafficking of synaptic mitochondria to regulate synaptic function and provide ATP where it is needed. Mutations in ubiquitously-expressed mitochondrial transport machinery selectively lead to neurological diseases in humans and mitochondrial dysfunction is associated with neurodegenerative diseases.[178,179] Photoreceptors are specialized neurons in the eye that respond to light and contain a unique type of mitochondrial network. Mitochondria in photoreceptors are highly concentrated in the ellipsoid region of the cell, where they can occupy up to 85% of the space.[67] Despite their abundant mitochondria with specific localization, photoreceptors appear to be much more resistant to mitochondrial stress than other neurons.[36,64]

We sought to understand what processes support photoreceptor survival upon mitochondrial stress. We previously observed that mitochondria damaged by Ca^{2+} stress moved away from the ellipsoid region of zebrafish cone photoreceptors, where they are thought to exclusively reside.[36,104] In this study, we demonstrate that this process is active in healthy cones and exacerbated across multiple models of chronic mitochondrial stress. Mislocalized mitochondria are more likely to be recycled in lysosomes than their ellipsoidal counterparts. Furthermore, mitochondria from the cones can leave the cones entirely and are present in lysosomes of the inner retina. The research described in this chapter highlights the unique adaptations of photoreceptor neurons to mitochondrial stress, characterizes selective mitochondrial trafficking in cones, and provides a framework for understanding the long-term survival of cones in response to mitochondrial insults.

Results

Healthy cone photoreceptors contain a small fraction of mislocalized mitochondria

To visualize mitochondria in living zebrafish cones, we generated a transgenic zebrafish line with a cone-specific mitochondrial tag using zebrafish transducin promoter (gnat2) upstream of the Su9 mitochondrial localization sequence tagged with the fluorescent protein mKate2. We crossed this model with the *crx*:mCFP zebrafish line (which marks membranes of rods, cones, and bipolar cells in zebrafish with CFP) to visualize any mislocalized mitochondria in WT

photoreceptors.[180] We found that mislocalized mitochondria in healthy photoreceptors are small (<2 μm) and rare at 6 days of age, but reproducibly present **(Figure 4.1A)**. Mislocalized mitochondria were equally likely to be observed in the cell body and synapse of the cones; surprisingly, they were also observed outside of the photoreceptors entirely **(Figure 4.1B)**. These were mostly located in the outer plexiform layer, just outside the photoreceptor synapses, but were also in the inner nuclear layer and beyond **(Figure 4.1C)**. We confirmed the presence of non-ellipsoid mitochondria in healthy cones using electron microscopy and determined that 2.1 ± 0.7 % of mitochondria in healthy photoreceptors are outside of the ellipsoid **(Figure 4.1D)**. Notably, all mitochondria observed outside of the ellipsoid had an abnormal appearance, with significantly less cristae and electron density **(Figure 4.1E)**.

Mitochondrial stress triggers mitochondrial movement in cones

We observed that all mitochondria outside of the ellipsoid in WT photoreceptors have an abnormal appearance, suggesting these mitochondria are stressed. All of the mislocalized mitochondria in a cone model for Ca^{2+} stress also had abnormal morphology.[36] Together, these observations led us to hypothesize that mitochondrial movement in zebrafish cones was an intrinsic response of photoreceptors to mitochondrial stress. We sought to determine if other mitochondrial stressors besides Ca^{2+} could trigger movement of mitochondria away from the cone ellipsoid.

We focused our study on chronic mitochondrial stressors, as adaptive mechanisms for chronic and acute mitochondrial stress differ and chronic stress more closely mimics the pathophysiology of neurodegenerative diseases. We first tested chloramphenicol (CAP), an antibiotic that targets the mitochondrial ribosome and inhibits translation of mRNA derived from mtDNA. Application of CAP in zebrafish larvae from 2 to 6 days of age has been shown to compromise mitochondrial health and function.[181] Indeed, incubation of zebrafish larvae in CAP increased the number of mislocalized cone mitochondria in a dose-dependent manner (**Figure 4.2A**). Mislocalized mitochondria in CAP-treated fish often have an elongated appearance, and elongated mitochondria are more abundant than in untreated fish (**Figure 4.2B**). We examined the dynamics of the mislocalized mitochondria in CAP-treated fish and found that rather than migrating unidirectionally away from the ellipsoid, mitochondria often oscillated away from and towards the ellipsoid (**Figure 4.2C**). However, we noted that chronic incubation with CAP significantly compromised zebrafish survival (consistent with ref. 181) and sought another way to induce mitochondrial stress in cones.

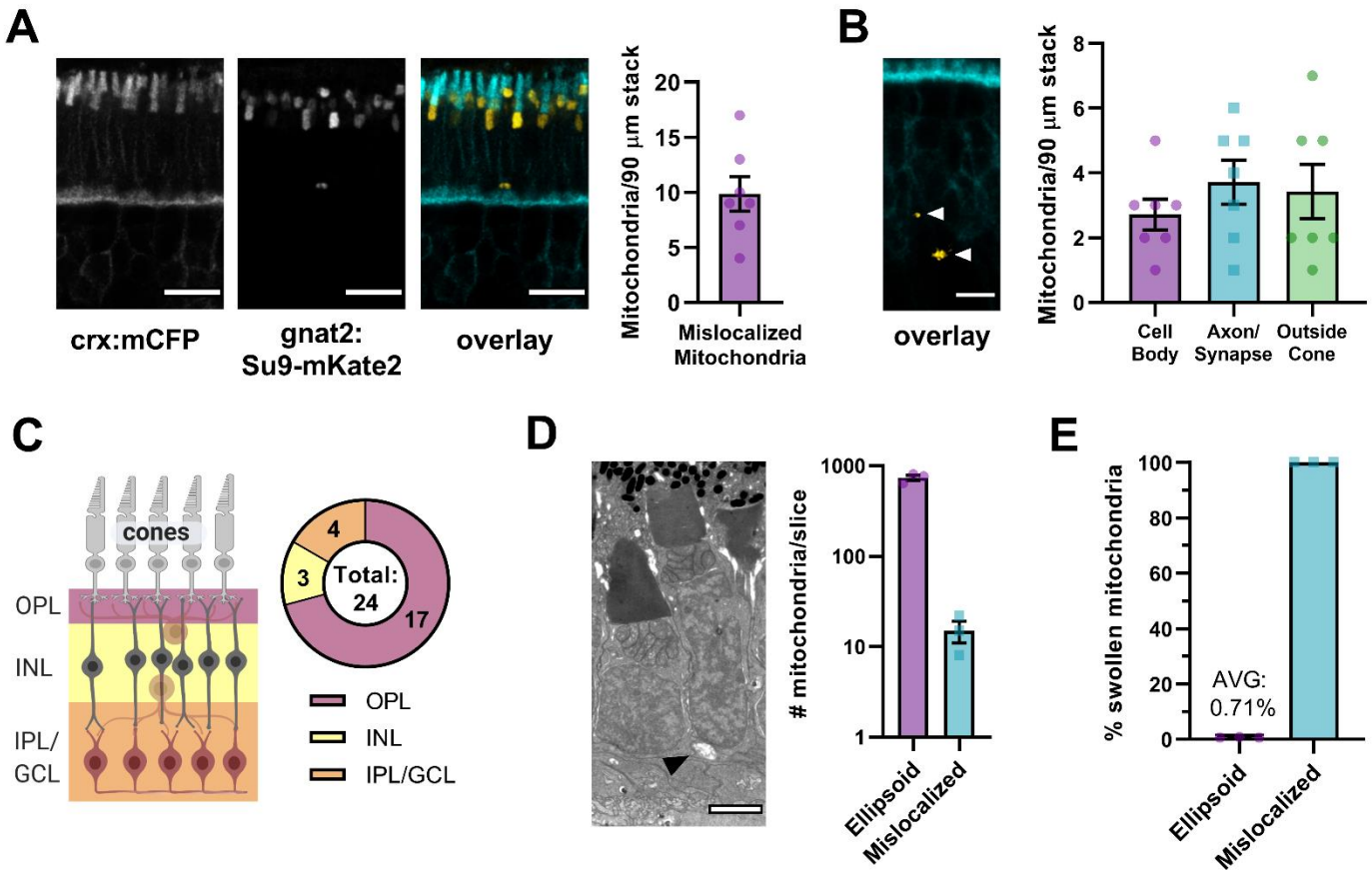

Figure 4.1: Mitochondria are observed rarely outside of the ellipsoid of normal cones.

A. Larvae expressing *crx*:mCFP (marking membranes of photoreceptors and bipolar cells) and *gnat2*:Su9-mKate2 (marking cone mitochondria) at 6 days of age, scale bar = 10 µm. Mitochondria can occasionally be found outside of the ellipsoid region (arrow), quantified as # per 100 µm x 100 µm x 90 µm volume. N=7 fish. Mean reported, bars = standard error.

B. Mislocalized mitochondria (from n=7 fish quantified in A) sorted by region in the cell. Mitochondria were not more likely to be in the synapse or cell body, and a significant portion were found outside of the cone cell layer. No significant differences were observed using one-way ANOVA. Mean reported, bars = standard error.

C. Most mitochondria outside of the cones were observed in the outer plexiform layer (OPL), but some were also observed in the inner nuclear layer (INL) and further in the retina (inner plexiform layer = IPL and ganglion cell layer = GCL). Numbers represent all pooled mitochondria found outside the cone region from n=7 fish.

D. Electron micrograph of a swollen, mislocalized mitochondria in 6-day-old larval cones (black arrow, scale bar = 2 µm). Electron micrographs were collected across the eye at the optic nerve, and all mitochondria across the stitched images were quantified (graph on right, n=3 fish). Ellipsoid mitochondria comprise most mitochondria in a healthy retina. Mean reported, bars = standard error.

E. Percentage of mitochondria with the electron-lucent, swollen phenotype by region from slices quantified in D. This phenotype is observed only in a small percentage of ellipsoid mitochondria but is observed in all mislocalized mitochondria. Mean reported, bars = standard error.

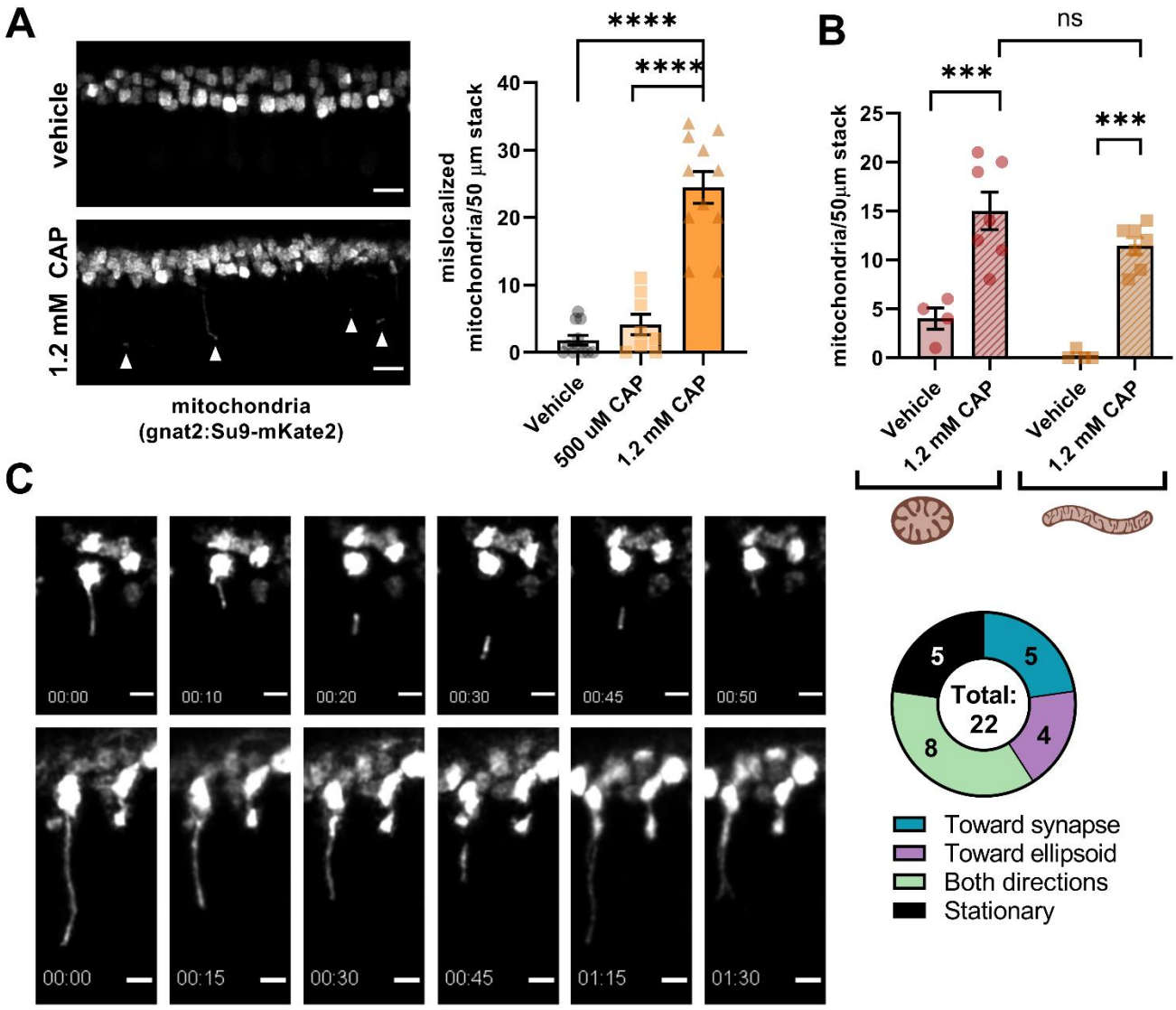

Figure 4.2: Inhibition of mitochondrial translation increases mitochondrial mislocalization in cones.

A. Mitochondrially-targeted *gnat2*:Su9-mKate2 in vehicle-treated (1.2% ethanol) and 1.2 mM chloramphenicol-treated (CAP) larvae after treatment from 3dpf-6dpf. Overall cone mitochondrial morphology is perturbed in CAP-treated fish, and mitochondria are observed outside of the ellipsoid region. Scale bar = 5 µm. ****p<0.0001 using one-way ANOVA followed by Tukey's test for multiple comparisons. Mean reported, bars = standard error.

B. Number of mislocalized mitochondria with rounded or elongated morphology assessed by gnat2:Su9-mKate2 fluorescence. A large increase in both rounded and elongated mitochondria is observed upon CAP-treatment. ***p<0.001 using two-way ANOVA followed by Tukey's test for multiple comparisons. A large increase in both rounded and elongated mitochondria is observed upon CAP-treatment. Mean reported, bars = standard error.

C. Mislocalized mitochondria can oscillate both away and toward the ellipsoid in CAP-treated fish. Gnat2:Su9-mKate2 is shown, scale bar = 2 µm. Mitochondria pooled from 2hr timelapses of two fish, imaging every 5 min.

Zebrafish are ectotherms, and thus sensitive to temperature changes in their environment. Cold exposure in zebrafish larvae increases generation of ROS in larval zebrafish brain, with markers of oxidative damage increasing after just 24 hours of incubation.[182] We incubated larval zebrafish at 16°C for 24 and 48 hours and found that increasing time at cold temperatures correlates with increased numbers of mislocalized cone mitochondria (**Figure 4.3A**). Unlike CAP-treated cone mitochondria, mitochondria in cold-treated fish are more likely to be rounded than elongated (**Figure 4.3B**).

We next crossed *gnat2*:Su9-mKate2 fish with *crx*:mCFP fish to better resolve the subcellular localization of mitochondria outside of the ellipsoid region. Mitochondria were primarily observed in the cell body and axon/synapse of cones, but a significant portion were still outside of the cone cells (**Figure 4.3C, D**). While there are more mitochondria outside of the cones in cold-treated fish than those raised at 28°C, mitochondria outside the cone represented a smaller fraction of the total mislocalized mitochondria (15.8 ± 2.8%, see **Figure 4.3C**). We examined the distribution of these mitochondria and found that while the number of cone mitochondria in the OPL (nearest cone synapses) tracked similarly between WT and cold-treated larvae, the number deeper in the retina (in the OPL/GCL) was significantly increased (**Figure 4.3E**).

In cones from fish raised at normal temperature, the mitochondria that are outside of the ellipsoid appear abnormal (**Figure 4.1D**).[36] Similarly, mislocalized mitochondria observed upon cold exposure have a swollen, electron-lucent phenotype consistent with mitochondrial stress (**Figure 4.3G**).

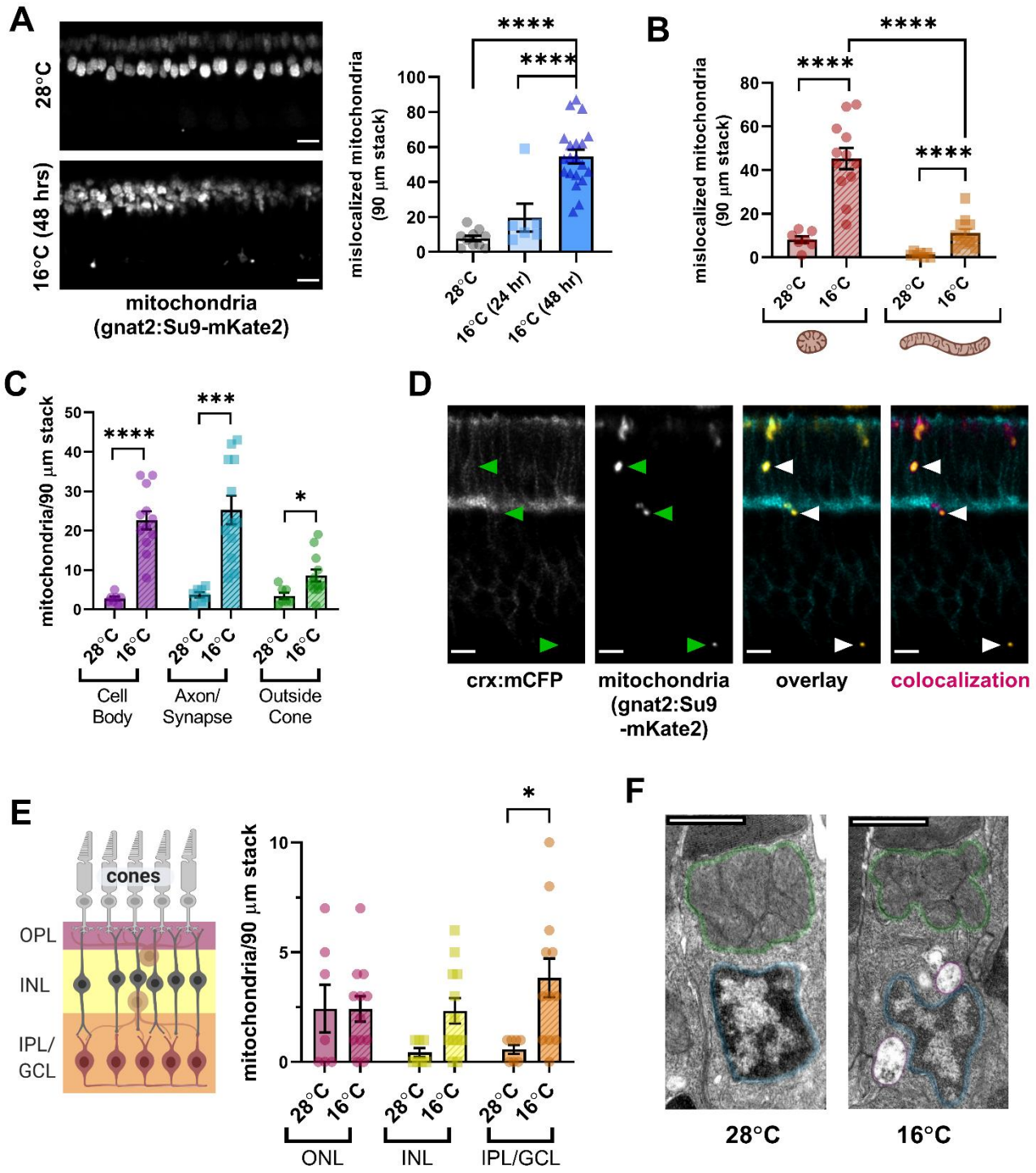

Figure 4.3: Cold exposure increases mitochondrial mislocalization in cones.

A. Mitochondrially-targeted *gnat2*:Su9-mKate2 in fish raised in 28°C until 6dpf, 16°C from 4dpf-6dpf, and 16°C from 5dpf-6dpf. General cone mitochondrial morphology is disturbed upon cold exposure, and mitochondria are observed outside of the ellipsoid region. Scale bar = 5 µm. ****p<0.0001 using one-way ANOVA followed by Tukey's test for multiple comparisons. Mean reported, bars = standard error.

B. Number of mislocalized mitochondria with rounded or elongated morphology assessed by *gnat2*:Su9-mKate2 fluorescence. Upon cold-exposure, more mislocalized mitochondria had rounded morphology than elongated morphology. ****p<0.0001 using two-way ANOVA followed by Tukey's test for multiple comparisons. Mean reported, bars = standard error.

Figure 4.3 continued: Cold exposure increases mitochondrial mislocalization in cones.

C. Mislocalized mitochondria quantified in B sorted by region of the cell. Mitochondria in all regions were increased upon cold exposure. ****p<0.0001, ***p<0.001, *p<0.05 using T-tests with the Holm-Sidak correction for multiple comparisons. Mean reported, bars = standard error.

D. Mislocalized mitochondria in cold-exposed (16°C, 48 hrs) fish expressing crx:mCFP (neural membranes) and *gnat2*:Su9-mKate2 (cone mitochondria). Co-localization of crx:mCFP and gnat2:Su9-mKate2 is highlighted in magenta. Mitochondria can be found inside cones, at the synapse, just outside the synapse in the OPL, and further in the retina.

E. Mitochondria found outside the cones were binned by region of the retina (outer plexiform layer=OPL, inner nuclear layer=INL, inner plexiform layer = IPL, and ganglion cell layer = GCL). Mitochondria observed furthest in the retina were most increase upon cold exposure. *p<0.05 using T-tests with the Holm-Sidak correction for multiple comparisons. Mean reported, bars = standard error.

F. Electron micrograph of 28°C and 16°C (48 hrs) cones (scale bar = 2 µm). The ellipsoid mitochondrial cluster is highlighted in green, the nucleus is highlighted in blue, and mislocalized mitochondria are highlighted in magenta.

Mislocalized mitochondria are preferentially recycled in lysosomes

Selective trafficking of abnormal mitochondria away from the ellipsoid could facilitate their recycling in lysosomes. To assess if mislocalized mitochondria were more likely to be in lysosomes, we incubated cold-exposed *gnat2*:Su9-mKate2 fish in Lysotracker Green and found that lysosomal puncta associate with a higher percentage of mislocalized mitochondria than ellipsoid mitochondria (**Figure 4.4A**). The characteristic abundance of lysosomes and synaptic vesicles at the cone synaptic layer allowed us to sort mitochondria by their location, and we found mitochondria outside of the photoreceptor layer are most likely to colocalize with lysosomes (**Figure 4.4B**). Relatively few mislocalized mitochondria in cell bodies were positive for lysotracker (14.5 ± 6.2%), but those observed had robust co-localization (**Figure 4.4C**). Cone mitochondria outside of the photoreceptor layer also colocalized well with lysotracker (**Figure 4.5D**). Specific co-localization of mitochondria near the cone synapse was more difficult to strictly assess at our available resolution due to the large number of lysosomes and acidic synaptic vesicles already present in that region (**Figure 4.6E**).

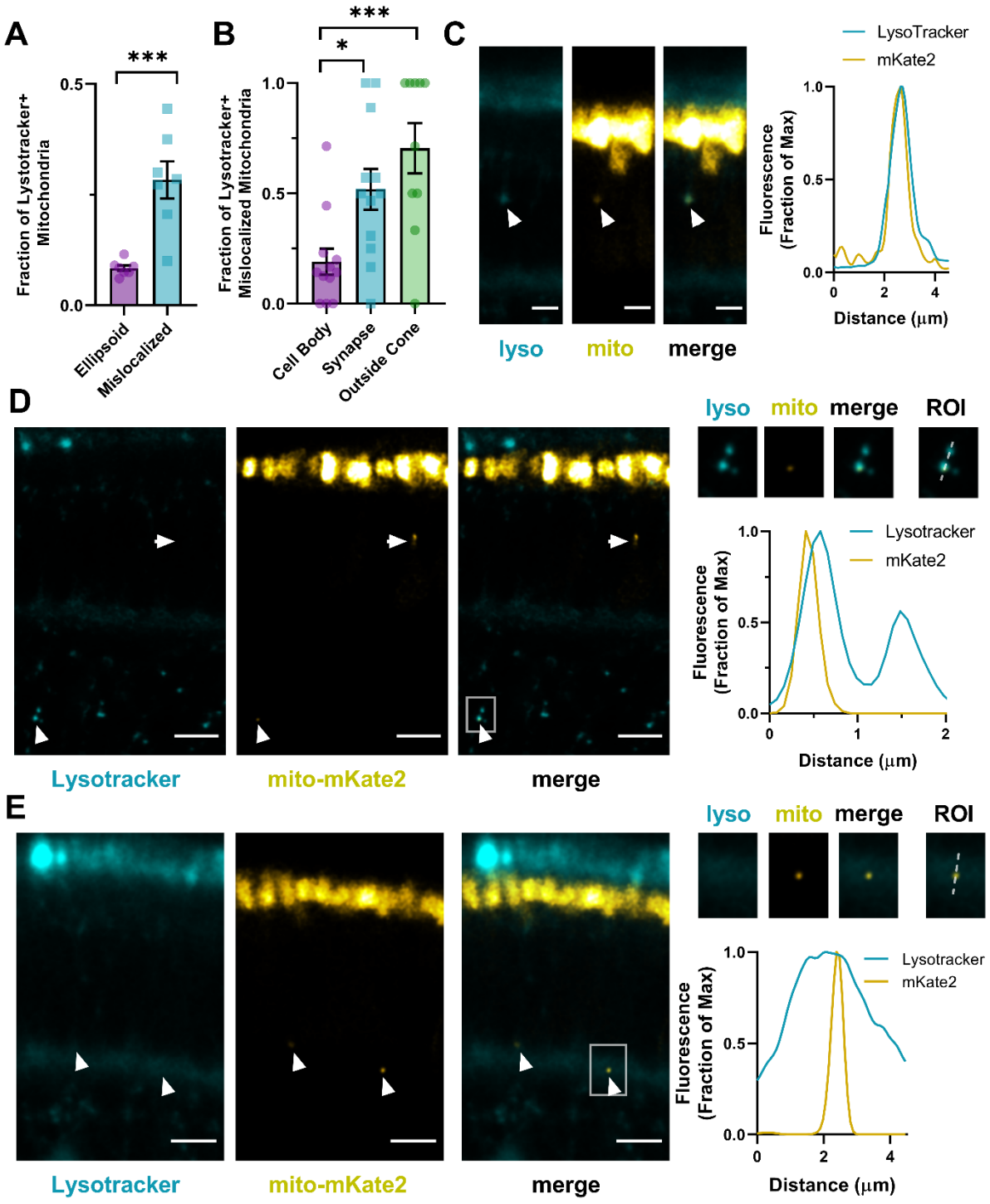

Figure 4.4: Mislocalized mitochondria are preferentially recycled in lysosomes.

A. Cold-exposed *gnat2*:Su9-mKate2 fish were incubated in LysoTracker Green (10 μM) for two hours, then imaged. Mislocalized mitochondria and ellipsoid mitochondrial clusters were marked as positive for lysotracker if any puncta were present on the mitochondria. A larger fraction of mislocalized mitochondria colocalized with LysoTracker (n=7 fish). All mitochondria were quantified from 50 μm stack. **p<0.01 using a paired t-test.

B. Fraction of mislocalized mitochondria (from A) that colocalized with LysoTracker, sorted by region of the cell. A higher fraction of mitochondria outside of cones were associated with lysosomes than those inside the cell. *p<0.05 using a one-way ANOVA with Tukey's test for multiple comparisons.

Figure 4.4 continued: Mislocalized mitochondria are preferentially recycled in lysosomes.

C. Left: Mislocalized cone mitochondria in cell body colocalizing with LysoTracker Green. Scale bar = 2 µm. Right: Line ROI through the puncta, max fluorescence normalized to 1.

D. Left: Mislocalized cone mitochondria (white arrows) both negative (cell body) and positive (outside cone) for LysoTracker Green. Scale bar = 5 µm. Right: Line ROI in boxed region, max fluorescence normalized to 1.

E. Left: Mislocalized mitochondria in cell body colocalizing with LysoTracker Green. The abundance of lysosomes at the cone synapses made specific colocalization in this region less clear. Scale bar = 2 µm. Right: Line ROI through the puncta, max fluorescence normalized to 1.

Discussion

A reasonable strategy for repairing or recycling damaged mitochondria would be to partition them away from the healthy mitochondrial population. In this study we show that abnormal mitochondria are selectively trafficked away from their usual localization in healthy cones and that this movement is enhanced in cones experiencing chronic mitochondrial stress. These trafficked mitochondria are preferentially recycled in lysosomes and can additionally be exported out of the photoreceptor layer. Our results highlight the unique mitochondrial adaptations of photoreceptors that may enable their long-term survival in response to mitochondrial stress.

We previously documented a role of Ca^{2+}-induced stress in stimulating movement of abnormal mitochondria in cones. We now show that other mitochondrial stressors, inhibition of mitochondrial ribosome activity and cold-exposure, can also elicit this movement. Even in a healthy cone neuron, a small fraction of the mitochondria can be found outside of the ellipsoid, and these were always observed to have abnormal morphology by electron microscopy. These observations suggest that mitochondrial trafficking away from the ellipsoid of cones is a common response to multiple types of mitochondrial stress and even a feature of normal cone function. Supporting this, studies of mitophagy in mouse retinas suggest that mitophagy is selectively enriched outside of the cone ellipsoids.[28,183]

Trafficking of mitochondria away from the ellipsoid is independent of a specific type of morphological change. Different stressors trigger divergent effects on mitochondrial morphology. Mitochondrial swelling is often induced by Ca^{2+} overload due to osmotic effects.[2,87,88] Fragmentation of mitochondria can be induced by oxidative stress and energetic stress.[18,184–186] Hyperfusion of the mitochondrial network can be induced in response to nutrient deprivation.[187] Mitochondria outside the ellipsoid in healthy cones and cold-exposed cones are much more likely to have a rounded appearance, while CAP-treated cones contain more elongated mitochondria. Even when damaged mitochondria swell to huge sizes in response to Ca^{2+} stress they can be actively shuttled away from the ellipsoid region, even displacing the nucleus to do so.[36]

A surprising finding of this study was the observation of cone mitochondria outside of the photoreceptor layer. Cones appear to be able to export mitochondria from the synapse region and into the outer plexiform layer. Exporting of mitochondria from intact cells is observed in other systems. In C. elegans neurons, mitochondria can be exported in huge vesicles called

exophers.[33] Additionally, extracellular respiratory-competent mitochondria have been observed in the bloodstream of healthy patients.[188] Our study and these observations underscore the need for closer study of cell-to-cell mitochondria transfer.

It is possible that the appearance of cone mitochondria outside the photoreceptor layer could be the result of cone death, as cone morphology is somewhat compromised in mitochondrial stress models (see outer segment length in **Figure 4.1A** compared to **Figure 4.3D**). Apoptotic bodies of cones in the pde6c^{w59} mutant are transported through the OPL and removed from the retina.[189] However, we have observed mitochondria that appear to be exiting from a cone synapse of a morphologically normal photoreceptor (**Figure 4.3D**). We also have observed cone mitochondria outside the photoreceptor layer in healthy retinas. Additional studies will be required to determine if dying cone cell bodies are the source of mitochondrial fluorescence in the inner retina.

In this study we found that mislocalized cone mitochondria are more likely to be found in lysosomes, especially mitochondria found outside of the cones. Lysosomes are the eventual "endpoint" of mitochondrial recycling, but more investigation is needed to understand how mitophagy occurs in photoreceptors. Mitochondrial depolarization is the most characterized initiators of mitophagy, and the proteins PINK1 and Parkin facilitate cellular recognition of depolarized mitochondria and recruitment of autophagosomal complexes to them. However, this is most often observed in models of acute mitochondrial stress. Mitochondrial depolarization is not strictly required for autophagosomal recruitment. Stressors such as nutrient deprivation facilitate autophagosomal recruitment to mitochondria with intact membrane potential, and mice lacking PINK1 appear to have uncompromised basal mitophagy.[27,107] There is no universal mechanism for initiation of mitochondrial recycling. Future work regarding mitochondrial stress in cones should use markers such as LC3 and TMRM to determine if mislocalized mitochondria are being phagocytosed by the cone machinery and if membrane depolarization is required for this to occur.

Overall, our results show that cones selectively traffic abnormal mitochondrial away from the cone ellipsoid. This process occurs in healthy cones and is exacerbated upon chronic mitochondrial stress. Mitochondria away from the ellipsoid are more likely to be recycled in lysosomes and can even be exported out of the cone cells. Our findings demonstrate a generalizable response of cones to mitochondrial stress that may underlie their remarkable survival when their mitochondria are compromised. Future investigations should focus on the mechanisms underlying this movement, the methods by which mitochondria are exported from

cones, and the other retina cells that may be ultimately responsible for clearing damaged cone mitochondria.

Materials and Methods

Zebrafish husbandry and transgenic models. Experiments with zebrafish were authorized by the University of Washington and University of Utah Institutional Animal Care and Use Committees. All fish used in this analysis were maintained in the University of Washington South Lake Union aquatics facility 28C on a 14 h/10 h light/dark cycle. All fish were in the $Roy^{-/-}$ genetic background. All fish used in the analysis were 6 days of age unless otherwise noted. Formal methods of randomization were not used.

The Tg(crx:mCFP) transgenic zebrafish line has been described previously.[180] Gateway cloning was used to assemble plasmids to generate the Tg(gnat2:Su9-mKate2) line. pDONR P2R-P3-mKate2 was a gift from Anna Planas & Tomas Santalucia (Addgene plasmid # 48345 ; http://n2t.net/addgene:48345 ; RRID:Addgene_48345).[190] Both entry vectors containing the promoter for cone transducin and the mitochondrial localization sequence for subunit 9 of ATP synthase were generated in-house.[117] Larvae mosaic for the transgene were raised to adulthood to identify founder carriers. Progeny from a single F_0 founder was used for analysis in this study.

Live imaging of zebrafish larvae. Larvae were maintained in embryo media containing 0.003% 1-phenyl 2-thiourea (PTU, Sigma-Aldrich P7629) starting at 20 hours post-fertilization, and kept in PTU for imaging. Live zebrafish larvae were imaged at 6 days postfertilization (dpf) by transferring to 1.0% low melting point agarose containing embryo media with 0.003% PTU and 0.02% (w/v) Tricaine (Sigma-Aldrich, E10521). After positioning in agarose and allowing it to solidify, larvae were covered in embryo media containing 0.003% PTU and 0.02% (w/v) tricaine. For lysosomal staining, 6 dpf larvae were incubated in Lysotracker Green DND-26 (Invitrogen L7526) for 2 hours, followed by three washes in embryo media prior to imaging. Imaging was performed using a Leica LSP8 confocal microscope with a 40X water objective. Leica LAS-X software (RRID:SCR_013673) with Lightning processing was used to acquire images. The z-depth for imaging was set at 1 µm. For timelapse imaging, stacks were acquired every 5 minutes for a total of 25 frames (2 hours). Images were processed using ImageJ + Fiji software ((SCR_002285). All counting of mislocalized mitochondria was performed while

blinded (masked) to sample identity. Larval experiments were repeated across at least two cohorts of siblings, with images from a representative experiment.

Transmission electron microscopy. Larval zebrafish were euthanized in an ice water bath and then incubated in 4% glutaraldehyde in 0.1 M sodium cacodylate buffer (pH 7.2) at 25 °C for 1 hour. Fixed larvae were stored overnight at 4°C, then post-fixed in osmium ferrocyanide (2% osmium tetroxide/3% potassium ferrocyanide in buffer) for 1 hr. Samples were then incubated in 1% thiocarbohydrazide for 20 min at 25 °C, in 2% osmium tetroxide for 30 min at 25 °C, and stained with 1% aqueous uranyl acetate overnight at 4°C. Samples were next stained *en bloc* with Walton's lead aspartate for 30 min at 60°C, dehydrated in a graded ethanol series, and embedded in Durcupan resin. Sections of tissue were cut at 60 nm thickness and imaged using a JEOL JEM-1230 transmission electron microscope. For quantification of mislocalized/electron-lucent mitochondria, montages of micrographs across the retina at the optic nerve were compiled for each individual fish.

Statistical Analysis. Numerical results are reported in the text as mean ± standard error of the mean unless otherwise stated. Graphpad Prism v 8.00 software was used to perform statistical tests and to generate graphs. For statistical analysis, replicates (n) were always defined as biological replicates. Information on what constitutes n (e.g. larvae, mitochondria) is listed in the figure legend of each experiment.

Acknowledgements

This chapter represents work that has not yet been published. The other authors that contributed to this study were Kaitlyn Rutter, James B. Hurley, and Susan E. Brockerhoff. We thank the University of Washington ISCRM aquatics facility for providing zebrafish husbandry and laboratory space. This work was supported by PHS NRSA T32GM007270 from NIGMS (RAH) and NIH grant NEI EY026020 (JBH and SEB).

Chapter 5: Conclusions and Future Directions

These studies aimed to characterize the mitochondrial calcium uniporter (MCU) complex in photoreceptors, specialized neurons that rely on Ca^{2+} signaling for function and have extraordinarily high ATP demands. By genetically manipulating the amount of MCU protein, we were able to uncover the role of MCU in healthy photoreceptors and characterize the responses of photoreceptors to mitochondrial stress. In sum, this dissertation has demonstrated the following:

1) Photoreceptors have relatively little mitochondrial Ca^{2+} influx via MCU

2) Photoreceptors have an alternative mode of mitochondrial Ca^{2+} uptake

3) Mitochondria can influence recovery of the photoresponse

4) Changing mitochondrial Ca^{2+} modulates the activity of α-KGDH and IDH in photoreceptors

5) Photoreceptors are remarkably resistant to mitochondrial stress

6) Mitochondrial stress triggers migration of mitochondria out of the photoreceptor ellipsoid, recycling of mitochondria in lysosomes, and potential export into other retinal cells

MCU complex in photoreceptors

Conclusions 1 & 2.

We have demonstrated that expression of the pore-forming protein of the MCU complex is exceptionally low in cones and rods compared to other neural tissues (**Figure 2.1, Figure 3.3**). Accordingly, uptake of Ca^{2+} through MCU compromises only ~40% of total mitochondrial Ca^{2+} uptake even when cytosolic Ca^{2+} is at very high levels in cones (**Figure 3.1**). While this low amount of cone MCU can certainly mediate some mitochondrial Ca^{2+} entry, another unknown mechanism is likely the primary mode of Ca^{2+} entry into cone mitochondria. If this is the case, the MCU complex in photoreceptors may act more as a “fail-safe” in exceptional circumstances, while alternative entry modes predominate in normal photoreceptor activity. One such extreme example is MCU activity when photoreceptors are in the dark state or when other Ca^{2+} extrusion mechanisms are compromised (**Figure 3.1G,H**).

Other candidates for Ca^{2+} entry have been described but are not as well-characterized as MCU. The prevailing view has been that MCU is primarily responsible for mitochondrial Ca^{2+} influx. However, the viability of MCU KO mice and zebrafish suggests that there is an alternative uptake mechanism.[140] Letm1 is a Ca^{2+}/H^{+} exchanger on the inner mitochondrial membrane that links Ca^{2+} influx and efflux to electron transport chain activity and mitochondrial pH.[191] Letm1 appears to act as a Ca^{2+} extrusion mechanism, but it also is capable of Ca^{2+} influx. Notably, Ca^{2+} influx via Letm1 would require protons to be transported against their concentration gradient under normal ETC activity. It is possible that this channel mediates some of the increase in ATP production upon mitochondrial Ca^{2+} uptake, as Letm1-mediated Ca^{2+} influx/H^{+} efflux would drive ATP synthase. There also is evidence that mitochondrial ryanodine receptors may exist, but they have only been reported in cardiac cells and neurons and have yet to be unambiguously identified.[192,193] Another attractive candidate is the mitochondrial Na^{+}/Ca^{2+} exchanger, which is associated with Ca^{2+} efflux but can run in reverse to promote Ca^{2+} entry into mitochondria.[163] A possible advantage of relying on these other mechanisms for Ca^{2+} transport is that it would link mitochondrial Ca^{2+} influx to factors other than cytosolic Ca^{2+} levels. The mitochondrial Na^{+}/Ca^{2+} exchanger would couple Ca^{2+} entry to cytosolic Na^{+}, which fluctuates in photoreceptors in response to light. Letm1 would tie Ca^{2+} entry to mitochondrial pH and ATP production; Letm1 has even been shown to be upregulated in cancer tissue, which is highly glycolytic like photoreceptors.[194]

Despite photoreceptors' low MCU activity and expression, the complex does appear dynamic and regulated. Transcript levels of the MCU modulators in retina were like that of the brain, including the neuronal Ca^{2+} uptake enhancer MICU3. When mitochondrial Ca^{2+} is constitutively elevated in the cone MCU overexpression model, retinas adapt by decreasing transcript levels of the MCU enhancer MICU3. Transcript abundance of MICU1 and MICU3 are highest in the retina and brain (**Figure 2.1C**), implying that even if few MCU complexes are formed these complexes allow cooperative and efficient uptake when cytosolic Ca^{2+} reaches high levels.[53,60]

Mitochondria and phototransduction

Conclusion 3.

The proximity of photoreceptor mitochondria to the base of the outer segment raises the possibility that mitochondria can serve as an additional mode of Ca^{2+} clearance from this region of the cell. Ca^{2+} clearance in the outer segment is essential for photoresponse recovery and

adaptation to light, and it is accomplished primarily by plasma membrane Na^+/Ca^{2+}, K^+ exchangers.[80] Surprisingly, both rods and cones lacking these exchangers are able to light-adapt, suggesting an additional pathway by which Ca^{2+} can be cleared from the outer segment.[75,150] The work in this dissertation raises mitochondria as a possible candidate for this residual response. Increasing Ca^{2+} uptake capacity of cone mitochondria via MCU overexpression increases the rate of cytosolic Ca^{2+} clearance and accelerates the recovery kinetics in response to light (**Figure 2.8, Figure 2.9**). Thus, we have demonstrated that photoreceptor mitochondria can directly shape the photoresponse by modulating intracellular Ca^{2+}.

However, we did not observe slower recovery of the photoresponse upon loss of MCU in rods. Recovery kinetics and light adaptation were unaltered, even when outer segment clearance from the rod Na^+/Ca^{2+}, K^+ exchanger was lost (**Figure 3.2, Figure 3.6, Figure 3.7**). Interpretation of this result is complicated by the existence of alternate pathways of mitochondrial Ca^{2+} uptake in photoreceptors (**Figure 3.1**). While MCU activity may not regulate Ca^{2+} clearance from the outer segment, this could still be accomplished by the unknown, alternative mode(s) of Ca^{2+} entry. There is evidence that mitochondria contribute to photorecovery in normal photoreceptors, as delayed rod photoresponse recovery is observed in human patients with malfunctioning mitochondria.[113]

Mitochondrial Ca^{2+} and photoreceptor metabolism

Conclusion 4.

The activity of pyruvate dehydrogenase (PDH), isocitrate dehydrogenase (IDH), and α-ketoglutarate dehydrogenase (α-KGDH) are sensitive to Ca^{2+}.[35]
Ca^{2+} binds directly to IDH and α-KGDH, but regulates PDH by altering the activity of its phosphatase.[195] While the Ca^{2+} sensitivity of these enzymes has been definitively demonstrated *in vitro*, previous studies in tissue relied on indirect readouts such as O_2 consumption or production of $ATP/FADH_2$.[37–39] In MCU-overexpressing cones, which have higher basal $[Ca^{2+}]_{mito}$, IDH and α-KGDH are more active *in vivo*. We showed that the primary effect of Ca^{2+} is modification of the reactant and product pool sizes, consistent with *in vitro* data that Ca^{2+} binding lowers the K_m of these enzymes (**Figure 2.5**). To our knowledge this is the first study to show directly that the K_m of these enzymes can be lowered by Ca^{2+} binding *in vivo*. In contrast, PDH activity and phosphorylation state were unaffected (**Figure 2.6**).

Photoreceptors experience the highest levels of intracellular Ca^{2+} in darkness, when O_2 consumption and ATP demand are highest, leading many to speculate that Ca^{2+} could play an important role in stimulating TCA cycle activity.[73,114] Evaluation of this hypothesis is complicated by our observation that photoreceptors have alternate pathways for mitochondrial Ca^{2+} uptake. When rods are deficient in MCU, there is a mild accumulation of α-ketoglutarate and isocitrate, consistent with a higher K_m of both IDH and α-KGDH (**Figure 3.4, Figure 3.5**). This is the opposite of the pattern observed in retinas containing MCU-overexpressing cones (**Figure 2.5**). We evaluated the role of Ca^{2+} in this phenotype by examining dark-adapted retinas, which have higher intracellular Ca^{2+} in photoreceptors. We observed only a mild accumulation of a-ketoglutarate in darkness (**Figure 3.5**). IDH may be unaffected because it requires ADP binding for Ca^{2+} to decrease its K_m, and free ADP is scarce in the high-energy state of darkness. However, we expected that darkness would increase the relative α-ketoglutarate accumulation in WT vs rod $MCU^{-/-}$ retinas. We did not observe this, so we cannot rule out that the accumulation of α-ketoglutarate is Ca^{2+}-independent.

Ultimately, the experiments in this dissertation demonstrate that MCU complex activity can alter photoreceptor metabolism, but this role in WT photoreceptors is relatively minor. This is consistent with its low expression in rods and cones. Unlike other tissues that use increased MCU activity to meet higher energetic demands, MCU does not appreciably mediate increased TCA activity in the energetically-demanding state of darkness.[195] However, it is possible that this occurs in photoreceptors independently of MCU. The alternative pathway(s) for Ca^{2+} to enter photoreceptor mitochondria must be identified before the relationship between mitochondrial metabolism and the light/dark state of photoreceptors can be fully understood.

Photoreceptor responses to mitochondrial stress

Conclusions 5 & 6.

The studies presented here demonstrate the extraordinary capacity of photoreceptors to handle multiple types of mitochondrial stress. In the case of mitochondrial Ca^{2+} stress, mitochondrial morphological phenotypes associated with cell death occur as early as 5 days of age but do not lead to widespread cone photoreceptor loss until 10 months of age (**Figure 2.4**). Inhibition of mtDNA translation by CAP treatment significantly compromises fish survival and morphology of the heart and spine, but cones appear relatively intact (**Figure 4.2**).[181]

Photoreceptors are likely uniquely equipped to handle mitochondrial dysfunction. Upon aging, photoreceptors in human retinas accumulate abnormal mitochondria and have a higher rate of mtDNA deletions compared to neurons in the inner retina, so they may have a greater imperative to tolerate mitochondrial stress to maintain function.[106,196] In patients with Leber's hereditary optic neuropathy, characterized by mtDNA mutations, widespread mitochondrial perturbations and cell death are observed in other retinal neurons and the nearby ocular muscle but the photoreceptors are relatively unaffected.[197,198] Many other mitochondrial diseases do not significantly compromise photoreceptor health despite affecting neurons in the central nervous system and other retinal cells.[199]

The adaptations of photoreceptors to chronic mitochondrial stress may hint at the underlying mechanisms behind their survival. Nearly all mitochondria are localized to the ellipsoid in healthy cones, but the few that are outside of it have an abnormal, electron-lucent appearance (**Figure 4.1**). Upon mitochondrial stress more cone mitochondria migrate outside of the ellipsoid region, and these also display abnormal morphology (**Figure 2.10**, **Figure 4.2**, **Figure 4.3**). Across all models assessed, abnormal mitochondria are selectively trafficked while healthy mitochondria remain in the ellipsoid (**Figure 2.10**, **Figure 4.1**). These findings fit well with existing literature in mouse models: lysosomal mitochondria are enriched in the outer nuclear layer of mouse retinas, and mitochondria have been observed near the outer limiting membrane in a rod-specific KO of the transcription factor Nrf1 that regulates mitochondrial DNA transcription and replication.[107,183,200]

What is the purpose of this movement? We initially hypothesized that it may be protect against Ca^{2+}-induced apoptosis, as mitochondria in the ellipsoid are adjacent to the outer segment where Ca^{2+} reaches very high levels in darkness. However, the generalizability of this phenomenon across mitochondrial stressors suggests that it may hold other benefits for the cell. This idea is supported by the observation that trafficking of mitochondria appears to be an active process. Upon mitochondrial Ca^{2+} stress, mitochondria move towards the synapse, with the large, swollen mitochondria displacing the nucleus to do so (**Figure 2.10**). Inhibition of mtDNA translation also induces less directed but nevertheless dynamic movement of mislocalized mitochondria (**Figure 4.2**). We next hypothesized that the active partitioning of abnormal mitochondria may facilitate their recycling. Indeed, we found that mitochondria outside of the ellipsoid region of cones are more likely to co-localize with lysosomes (**Figure 4.4**). Active transport of damaged mitochondria to facilitate their recycling is unique among neurons –

mitophagy is often associated with a cessation of mitochondrial movement.[20–22] However, recent studies have uncovered the mitochondrial docking protein syntaphilin, which is released from synaptic mitochondria upon chronic stress to allow them to move back to the cell body.[23,176] It is also possible that unidentified proteins are involved in the unique mitochondrial movement in photoreceptors.

Finally, we were surprised to find cone mitochondria outside of the photoreceptor layer entirely, even in healthy retinas (**Figure 4.1, Figure 4.3**). This could be due to cone cell death, as cone apoptotic bodies can be transported through the outer plexiform layer and removed from the retina.[189] However, we sometimes observed mitochondria exiting the synapse region in the absence of morphologically dying cones (**Figure 4.3D**). This suggests that the presence of cone mitochondria outside of cone cells is not solely the result of dying cones being recycled by retinal glia, but export of mitochondrial material. If damaged mitochondria are indeed exported out of cones, this would not be without precedent. Retinal ganglion cells can extrude their own mitochondria for degradation by astrocytes, and neurons in C. elegans can extrude large vesicles of mitochondria upon cellular and mitochondrial stress.[32,33]

Future Directions

While MCU may be the primary pathway for Ca^{2+} entry into mitochondria in many cells, photoreceptors limit MCU in favor of another, as yet unidentified pathway. Future work should ascertain the identity of this pathway, which could be the action of multiple mitochondrial channels. The mitochondrial Na^{+}/Ca^{2+} exchanger is an attractive candidate to test, as specific inhibitors are available.[201] Letm1 is also another promising candidate. Knockdown of Letm1 via siRNA impairs Ca^{2+} transport into the mitochondria of Flp-In-293 cells, and a mouse genetic knockout of Letm1 (the mitochondrial Ca^{2+}/H^{+} antiporter) is available. While $Letm1^{-/-}$ mice aren't viable and only some $Letm1^{+/-}$ mice survive, the surviving heterozygotes have impaired ATP production specifically in neuronal tissue and PDH activity is also compromised.[202] Photoreceptor neurons may depend on Letm1 for mitochondrial Ca^{2+} uptake similar to brain tissue. Identification of the primary mode of Ca^{2+} import into photoreceptor mitochondria is essential to determine the role mitochondrial Ca^{2+} plays in normal photoreceptor responses to light and metabolic regulation.

Cold stress induces robust mitochondrial mislocalization without compromising fish survival; we hypothesize that the mitochondrial stress upon cold exposure is increased ROS production as previously reported.[182] However, the link between cold-exposure and ROS should be more clearly determined for cones. Use of the cell permeable ROS dye CM-H_2DCFDA and antibody detection of the lipid peroxidation product 4-HNE would facilitate this.[203,204] Additionally, ROS production specifically in cones could be induced by expression of the construct KillerRed, which produces radicals and hydrogen peroxide upon light exposure in the 540-580 nm range.[205] Expression of mitochondrially-targeted KillerRed would provide a specific and tunable mitochondrial stress in cones.[206] This could allow induction of ROS that is sufficient to trigger mitochondrial movement without compromising the health of cones. Furthermore, because this would be cone specific, it would also remove stress in other retinal cells as a confounding factor.

While this study has extensively documented mitochondrial movement in photoreceptors as a response to stress, the mechanism by which they move is unknown. Generally, mitochondrial movement in a cell is enabled by the cytoskeleton. Mitochondria move along microtubules via adaptor proteins (MIRO1/2, TRAK1/2) that anchor mitochondria to the microtubule motors kinesin and dynein.[207] This is thought to be the primary mode of mitochondrial transport in cells.[208] Mitochondria can also associate with actin filaments, which may function as anchors preventing trafficking along microtubules or serve as a platform for mitochondrial movement themselves.[209,210] Treating zebrafish with inhibitors of both actin and microtubule polymerization could elucidate how these mitochondria are traveling in response to stress. A reasonable hypothesis is that mitochondria in the ellipsoid region of cones are docked to actin, and release of this docking is what allows them to move along microtubules. This is an even more attractive hypothesis given recent research on the docking protein syntaphilin, which is released in response to chronic mitochondrial stress to allow mitochondria to move.[23,211] Evaluating syntaphilin expression in photoreceptors, and genetically manipulating its expression would be particularly enlightening.

Finally, the potential export of damaged mitochondria from photoreceptors should be investigated further. First, cell death should be assessed via PI-staining or acridine orange to see if mitochondria outside the photoreceptor layer are localized to apoptotic cells. Reconstructions via 3D-scanning block-face electron microscopy would allow better resolution of any mitochondria that may be exiting photoreceptors. Additionally, correlative fluorescent and electron microscopy has previously been implemented to analyze zebrafish retinas.[212] This

would allow identification of cone mitochondrial structures (using the *gnat2*:Su9-mKate2 fish) at high resolution in electron micrographs, making their identification unambiguous. In retinal ganglion axons, exported mitochondria are taken up by glia in the optic nerve head of the brain.[32] Zebrafish lines with fluorescently-labelled retinal microglia (*Tg(mpeg1:EGFP)*, Zebrafish International Resource Center) and retinal Müller glia (*Tg(gfap:tdTomato)*, Janelia Research Campus) are available in-house and will be used to determine the fate of exported cone mitochondria in the retina.

Summary and Impact

Photoreceptors are specialized neurons that are subject to a lifetime of stressors, including light damage, high ATP demand, and large Ca^{2+} fluctuations. We have shown that photoreceptors are remarkably resistant to mitochondrial stress and have unique adaptations that may support this survival. Photoreceptors respond to a variety of chronic mitochondrial stressors by selectively trafficking damaged mitochondria away from their normal localization in the ellipsoid. These mislocalized mitochondria are more likely to be engulfed in lysosomes than their counterparts in the ellipsoid and may even be exported out of cones entirely. This work has revealed the unique responses of photoreceptors to mitochondrial stress and motivates study into intercellular transport of mitochondria in the retina. Furthermore, the distinct localization of mitochondria in zebrafish cones makes them an attractive model for future study of the mechanisms underlying selective sorting and trafficking of damaged mitochondria that could apply to other cell types.

This work has also demonstrated another feature of photoreceptors: despite their dependence on Ca^{2+} homeostasis for function and health, they do not rely on MCU. We demonstrate that another pathway for Ca^{2+} uptake into mitochondria exists in photoreceptors. While we have shown that mitochondrial Ca^{2+} uptake can alter photoreceptor metabolism and the response to light, this does not appear to be mediated by the MCU complex. These studies have identified a cell type where MCU is not the predominant mode of mitochondrial Ca^{2+} entry. Photoreceptors may not be unique in this respect, and further research into these alternate modes of mitochondrial Ca^{2+} uptake are necessary to fully understand the role of mitochondrial Ca^{2+} in cellular homeostasis.

References

1. Chandel, N. S. *Navigating Metabolism*. (Cold Spring Harbor Laboratory Press, 2015).
2. Rasola, A. & Bernardi, P. *Mitochondrial permeability transition in Ca2+-dependent apoptosis and necrosis*. *Cell Calcium* **50**, 222–233 (2011).
3. Luft, R., Ikkos, D., Palmieri, G., Ernstert, L. & Afzelius, B. *A CASE OF SEVERE HYPERMETABOLISM OF NONTHYROID ORIGIN A DEFECT IN THE MAINTENANCE OF MITOCHONDRIAL RE-SPIRATORY CONTROL: A CORRELATED CLINICAL, BIO-CHEMICAL, AND MORPHOLOGICAL STUDY*. *Journal of Clinical Investigation* **41**, (1962).
4. Lowell, B. B. & Shulman, G. I. Mitochondrial dysfunction and type 2 diabetes. *Science* **307**, 384–387 (2005).
5. Bua, E. A., McKiernan, S. H., Wanagat, J., McKenzie, D. & Aiken, J. M. Mitochondrial abnormalities are more frequent in muscles undergoing sarcopenia. *J. Appl. Physiol.* **92**, 2617–2624 (2002).
6. Wang, X. *et al.* Oxidative stress and mitochondrial dysfunction in Alzheimer's disease. *Biochimica et Biophysica Acta - Molecular Basis of Disease* **1842**, 1240–1247 (2014).
7. Ballinger, S. W. Mitochondrial dysfunction in cardiovascular disease. *Free Radical Biology and Medicine* **38**, 1278–1295 (2005).
8. Wallace, D. C. A Mitochondrial Paradigm of Metabolic and Degenerative Diseases, Aging, and Cancer: A Dawn for Evolutionary Medicine. *Annu. Rev. Genet.* **39**, 359–407 (2005).
9. Pieczenik, S. R. & Neustadt, J. Mitochondrial dysfunction and molecular pathways of disease. *Exp. Mol. Pathol.* **83**, 84–92 (2007).
10. Sun, N., Youle, R. J. & Finkel, T. The Mitochondrial Basis of Aging. *Molecular Cell* **61**, 654–666 (2016).
11. Youle, R. J. & Van Der Bliek, A. M. Mitochondrial fission, fusion, and stress. *Science* **337**, 1062–1065 (2012).
12. Eisner, V., Picard, M. & Hajnóczky, G. Mitochondrial dynamics in adaptive and maladaptive cellular stress responses. *Nature Cell Biology* **20**, 755–765 (2018).
13. Starkov, A. A. The role of mitochondria in reactive oxygen species metabolism and signaling. in *Annals of the New York Academy of Sciences* **1147**, 37–52 (Blackwell Publishing Inc., 2008).
14. Pellegrino, M. W., Nargund, A. M. & Haynes, C. M. Signaling the mitochondrial unfolded protein response. *Biochimica et Biophysica Acta - Molecular Cell Research* **1833**, 410–416 (2013).
15. Lewis, M. R. & Lewis, W. H. Mitochondria (and other cytoplasmic structures) in tissue cultures. *Am. J. Anat.* **17**, 339–401 (1915).
16. Nakada, K. *et al.* Inter-mitochondrial complementation: Mitochondria-specific system preventing mice from expression of disease phenotypes by mutant mtDNA. *Nat. Med.* **7**, 934–940 (2001).
17. Twig, G., Hyde, B. & Shirihai, O. S. Mitochondrial fusion, fission and autophagy as a quality control axis: The bioenergetic view. *Biochimica et Biophysica Acta - Bioenergetics* **1777**, 1092–1097 (2008).
18. Iqbal, S. & Hood, D. A. Oxidative stress-induced mitochondrial fragmentation and movement in skeletal muscle myoblasts. **306**, (2014).
19. Debattisti, V., Gerencser, A. A., Saotome, M., Das, S. & Hajnóczky, G. ROS Control Mitochondrial

Motility through p38 and the Motor Adaptor Miro/Trak. *Cell Rep.* **21**, 1667–1680 (2017).

20. Chang, K. T., Niescier, R. F. & Min, K.-T. Mitochondrial matrix Ca2+ as an intrinsic signal regulating mitochondrial motility in axons. *Proc. Natl. Acad. Sci. U. S. A.* **108**, 15456–61 (2011).

21. Cai, Q., Zakaria, H. M., Simone, A. & Sheng, Z.-H. Spatial Parkin Translocation and Degradation of Damaged Mitochondria via Mitophagy in Live Cortical Neurons. *Curr. Biol.* **22**, 545–552 (2012).

22. Wang, X. *et al.* PINK1 and Parkin Target Miro for Phosphorylation and Degradation to Arrest Mitochondrial Motility. *Cell* **147**, 893–906 (2011).

23. Lin, M.-Y. Y. *et al.* Releasing Syntaphilin Removes Stressed Mitochondria from Axons Independent of Mitophagy under Pathophysiological Conditions. *Neuron* **94**, 595-610.e6 (2017).

24. O'Mealey, G. B. *et al.* A PGAM5-KEAP1-Nrf2 complex is required for stress-induced mitochondrial retrograde trafficking. *J. Cell Sci.* **130**, 3467–3480 (2017).

25. Al-Mehdi, A. B. *et al.* Perinuclear mitochondrial clustering creates an oxidant-rich nuclear domain required for hypoxia-induced transcription. *Sci. Signal.* **5**, ra47–ra47 (2012).

26. Jin, S. M. & Youle, R. J. PINK1-and Parkin-mediated mitophagy at a glance. *J. Cell Sci.* **125**, 795–799 (2012).

27. Kim, I., Rodriguez-Enriquez, S. & Lemasters, J. J. *Selective degradation of mitochondria by mitophagy*. *Archives of Biochemistry and Biophysics* **462**, 245–253 (Academic Press, 2007).

28. Mcwilliams, T. G. *et al.* Short Article Basal Mitophagy Occurs Independently of PINK1 in Mouse Tissues of High Metabolic Demand Short Article Basal Mitophagy Occurs Independently of PINK1 in Mouse Tissues of High Metabolic Demand. 439–449 (2018). doi:10.1016/j.cmet.2017.12.008

29. Rustom, A., Saffrich, R., Markovic, I., Walther, P. & Gerdes, H. H. Nanotubular Highways for Intercellular Organelle Transport. *Science (80-.).* **303**, 1007–1010 (2004).

30. Torralba, D., Baixauli, F. & Sánchez-Madrid, F. Mitochondria know no boundaries: Mechanisms and functions of intercellular mitochondrial transfer. *Frontiers in Cell and Developmental Biology* **4**, 107 (2016).

31. Hayakawa, K. *et al.* Transfer of mitochondria from astrocytes to neurons after stroke. *Nature* **535**, 551–555 (2016).

32. Davis, C. O. *et al.* Transcellular degradation of axonal mitochondria. *Proc. Natl. Acad. Sci. U. S. A.* **111**, 9633–8 (2014).

33. Melentijevic, I. *et al.* C. elegans neurons jettison protein aggregates and mitochondria under neurotoxic stress. *Nature* (2017). doi:10.1038/nature21362

34. Lyamzaev, K. G. *et al.* Novel mechanism of elimination of malfunctioning mitochondria (mitoptosis): Formation of mitoptotic bodies and extrusion of mitochondrial material from the cell. *Biochim. Biophys. Acta - Bioenerg.* **1777**, 817–825 (2008).

35. Denton, R. M. Regulation of mitochondrial dehydrogenases by calcium ions. *Biochim. Biophys. Acta - Bioenerg.* **1787**, 1309–1316 (2009).

36. Hutto, R. A. *et al.* Increasing Ca2+ in photoreceptor mitochondria alters metabolites, accelerates photoresponse recovery, and reveals adaptations to mitochondrial stress. *Cell Death Differ.* **27**, 1067–1085 (2020).

37. Balaban, R. S. The role of Ca2+ signaling in the coordination of mitochondrial ATP production with cardiac work. *Biochim. Biophys. Acta - Bioenerg.* **1787**, 1334–1341 (2009).

38. Hajnóczky, G., Robb-Gaspers, L. D., Seitz, M. B. & Thomas, A. P. Decoding of cytosolic calcium oscillations in the mitochondria. *Cell* **82**, 415–424 (1995).

39. Jouaville, L. S., Pinton, P., Bastianutto, C., Rutter, G. A. & Rizzuto, R. Regulation of mitochondrial ATP synthesis by calcium: evidence for a long-term metabolic priming. *Proc. Natl. Acad. Sci. U. S. A.* **96**, 13807–12 (1999).

40. Glancy, B. & Balaban, R. S. Role of Mitochondrial Ca $^{2+}$ in the Regulation of Cellular Energetics. *Biochemistry* **51**, 2959–2973 (2012).

41. Feissner, R. F., Skalska, J., Gaum, W. E. & Sheu, S. S. Crosstalk signaling between mitochondrial Ca2+ and ROS. *Front. Biosci.* **14**, 1197–1218 (2009).

42. McCarron, J. G., Olson, M. L. & Chalmers, S. Mitochondrial regulation of cytosolic Ca 2+ signals in smooth muscle. *Pflugers Archiv European Journal of Physiology* **464**, 51–62 (2012).

43. Medler, K. & Gleason, E. L. Mitochondrial Ca $^{2+}$ Buffering Regulates Synaptic Transmission Between Retinal Amacrine Cells. *J. Neurophysiol.* **87**, 1426–1439 (2002).

44. Baumgartner, H. K. *et al.* Calcium elevation in mitochondria is the main Ca2+ requirement for mitochondrial permeability transition pore (mPTP) opening. *J. Biol. Chem.* **284**, 20796–20803 (2009).

45. Shoshan-Barmatz, V. & Gincel, D. The Voltage-Dependent Anion Channel: Characterization, Modulation, and Role in Mitochondrial Function in Cell Life and Death. *Cell Biochem. Biophys.* **39**, 279–292 (2003).

46. Deluca, H. F. & Engstrom, G. W. Calcium uptake by rat kidney mitochondria. *Proc. Natl. Acad. Sci. U. S. A.* **47**, (1961).

47. Baughman, J. M. *et al.* Integrative genomics identifies MCU as an essential component of the mitochondrial calcium uniporter. *Nature* **476**, 341–345 (2011).

48. De Stefani, D., Raffaello, A., Teardo, E., Szabò, I. & Rizzuto, R. A forty-kilodalton protein of the inner membrane is the mitochondrial calcium uniporter. *Nature* **476**, 336–40 (2011).

49. De Stefani, D., Patron, M. & Rizzuto, R. Structure and function of the mitochondrial calcium uniporter complex. *Biochim. Biophys. Acta - Mol. Cell Res.* **1853**, 2006–2011 (2015).

50. Perocchi, F. *et al.* MICU1 encodes a mitochondrial EF hand protein required for Ca(2+) uptake. *Nature* **467**, 291–6 (2010).

51. Plovanich, M. *et al.* MICU2, a Paralog of MICU1, Resides within the Mitochondrial Uniporter Complex to Regulate Calcium Handling. *PLoS One* **8**, e55785 (2013).

52. Sancak, Y. *et al.* EMRE is an essential component of the mitochondrial calcium uniporter complex. *Science* **342**, 1379–82 (2013).

53. Patron, M., Granatiero, V., Espino, J., Rizzuto, R. & De Stefani, D. MICU3 is a tissue-specific enhancer of mitochondrial calcium uptake. *Cell Death Differ.* **26**, 179–195 (2018).

54. Chaudhuri, D., Artiga, D. J., Abiria, S. A. & Clapham, D. E. Mitochondrial calcium uniporter regulator 1 (MCUR1) regulates the calcium threshold for the mitochondrial permeability transition. *Proc. Natl. Acad. Sci. U. S. A.* **113**, E1872-80 (2016).

55. Hoffman, N. E. *et al.* SLC25A23 augments mitochondrial Ca2+ uptake, interacts with MCU, and induces oxidative stress-mediated cell death. *Mol. Biol. Cell* **25**, 936–947 (2014).

56. Nieminen, A.-L. *et al.* Mitoferrin-2 (MFRN2) Regulates the Electrogenic Mitochondrial Calcium Uniporter and Interacts Physically with MCU. *Biophys. J.* **106**, 581a-582a (2014).

57. Paupe, V., Prudent, J., Dassa, E. P., Rendon, O. Z. & Shoubridge, E. A. *CCDC90A (MCUR1) Is a Cytochrome c Oxidase Assembly Factor and Not a Regulator of the Mitochondrial Calcium Uniporter*. *Cell Metabolism* **21**, (2015).

58. Tomar, D. *et al.* MCUR1 Is a Scaffold Factor for the MCU Complex Function and Promotes Mitochondrial Bioenergetics. *Cell Rep.* **0**, 833–844 (2016).

59. Zeng, F. *et al.* RIPK1 Binds MCU to Mediate Induction of Mitochondrial Ca $^{2+}$ Uptake and Promotes Colorectal Oncogenesis. *Cancer Res.* **78**, 2876–2885 (2018).

60. Paillard, M. *et al.* Tissue-Specific Mitochondrial Decoding of Cytoplasmic Ca 2+ Signals Is Controlled by the Stoichiometry of MICU1/2 and MCU. *Cell Rep.* **18**, 2291–2300 (2017).

61. Gherardi, G. *et al.* Loss of mitochondrial calcium uniporter rewires skeletal muscle metabolism and substrate preference. *Cell Death Differ.* **26**, 362–381 (2018).

62. Mammucari, C. *et al.* The Mitochondrial Calcium Uniporter Controls Skeletal Muscle Trophism In Vivo. *Cell Rep.* **10**, 1269–1279 (2015).

63. Qiu, J. *et al.* Mitochondrial calcium uniporter Mcu controls excitotoxicity and is transcriptionally repressed by neuroprotective nuclear calcium signals. *Nat. Commun.* **4**, 360–364 (2013).

64. Granatiero, V., Pacifici, M., Raffaello, A., De Stefani, D. & Rizzuto, R. Overexpression of Mitochondrial Calcium Uniporter Causes Neuronal Death. (2019). doi:10.1155/2019/1681254

65. Soman, S. K., Bazała, M., Keatinge, M., Bandmann, O. & Kuznicki, J. Restriction of mitochondrial calcium overload by mcu inactivation renders a neuroprotective effect in zebrafish models of Parkinson's disease. *Biol. Open* **8**, (2019).

66. Tom Dieck, S. & Brandstätter, J. H. Ribbon synapses of the retina. *Cell and Tissue Research* **326**, 339–346 (2006).

67. Hoang, Q. V., Linsenmeier, R. A., Chung, C. K. & Curcio, C. A. Photoreceptor inner segments in monkey and human retina: Mitochondrial density, optics, and regional variation. *Vis. Neurosci.* **19**, 395–407 (2002).

68. Stone, J., van Driel, D., Valter, K., Rees, S. & Provis, J. The locations of mitochondria in mammalian photoreceptors: Relation to retinal vasculature. *Brain Res.* **1189**, 58–69 (2008).

69. Ishikawa, T. & Yamada, E. Atypical mitochondria in the ellipsoid of the photoreceptor cells of vertebrate retinas. *Invest. Ophthalmol.* **8**, 302–316 (1969).

70. Masuda, T., Wada, Y. & Kawamura, S. ES1 is a mitochondrial enlarging factor contributing to form mega-mitochondria in zebrafish cones. *Sci. Rep.* **6**, 22360 (2016).

71. Nakatani, K. & Yau, K.-W. W. Calcium and light adaptation in retinal rods and cones. *Nature* **334**, 69–71 (1988).

72. Barnes, S. & Kelly, M. E. M. Calcium channels at the photoreceptor synapse. *Adv. Exp. Med. Biol.* **514**, 465–76 (2002).

73. Okawa, H., Sampath, A. P., Laughlin, S. B. & Fain, G. L. ATP Consumption by Mammalian Rod Photoreceptors in Darkness and in Light. *Curr. Biol.* **18**, 1917–1921 (2008).

74. Fain, G. L. Why photoreceptors die (and why they don't). *BioEssays* **28**, 344–354 (2006).

75. Vinberg, F. *et al.* The Na+/Ca2+, K+ exchanger NCKX4 is required for efficient cone-mediated vision. *Elife* **6**, (2017).

76. Križaj, D. Calcium stores in vertebrate photoreceptors. *Adv. Exp. Med. Biol.* **740**, 873–89 (2012).

77. Krizaj, D. & Copenhagen, D. R. Compartmentalization of Calcium Extrusion Mechanisms in the Outer and Inner Segments of Photoreceptors. *Neuron* **21**, 249–256 (1998).

78. Szikra, T. & Krizaj, D. Intracellular organelles and calcium homeostasis in rods and cones. *Vis. Neurosci.* **24**, 733–43 (2007).

79. Giarmarco, M. M., Cleghorn, W. M., Sloat, S. R., Hurley, J. B. & Brockerhoff, S. E. Mitochondria maintain distinct Ca2+ pools in cone photoreceptors. *J. Neurosci.* **37**, 2061–2072 (2017).

80. Vinberg, F., Chen, J. & Kefalov, V. J. Regulation of calcium homeostasis in the outer segments of rod and cone photoreceptors. *Prog. Retin. Eye Res.* **67**, 87–101 (2018).

81. He, L., Poblenz, A. T., Medrano, C. J. & Fox, D. A. Lead and Calcium Produce Rod Photoreceptor Cell Apoptosis by Opening the Mitochondrial Permeability Transition Pore*. *J. Biol. Chem.* **275**, 12175–12184 (2000).

82. Griffiths, E. J. & Rutter, G. A. Mitochondrial calcium as a key regulator of mitochondrial ATP production in mammalian cells. *Biochim. Biophys. Acta - Bioenerg.* **1787**, 1324–1333 (2009).

83. Stearns, G., Evangelista, M., Fadool, J. M. & Brockerhoff, S. E. A Mutation in the Cone-Specific pde6 Gene Causes Rapid Cone Photoreceptor Degeneration in Zebrafish. *J. Neurosci.* **27**, 13866–13874 (2007).

84. Winkler, B. S., Starnes, C. A., Twardy, B. S., Brault, D. & Taylor, R. C. Nuclear Magnetic Resonance and Biochemical Measurements of Glucose Utilization in the Cone-Dominant Ground Squirrel Retina AND. *Invest. Ophthalmol. Vis. Sci.* **49**, 4613–4619 (2008).

85. Kim, J. H. *et al.* High Cleavage Efficiency of a 2A Peptide Derived from Porcine Teschovirus-1 in Human Cell Lines, Zebrafish and Mice. *PLoS One* **6**, e18556 (2011).

86. Chen, Y. *et al.* Structural insight into enhanced calcium indicator GCaMP3 and GCaMPJ to promote further improvement. *Protein Cell* **4**, 299–309 (2013).

87. Zoratti, M. & Szabò, I. The mitochondrial permeability transition. *Biochim. Biophys. Acta - Rev. Biomembr.* **1241**, 139–176 (1995).

88. Elustondo, P. A. *et al.* Mitochondrial permeability transition pore induction is linked to formation of the complex of ATPase C-subunit, polyhydroxybutyrate and inorganic polyphosphate. *Cell Death Discov.* **2**, 16070 (2016).

89. Mammucari, C. *et al.* The Mitochondrial Calcium Uniporter Controls Skeletal Muscle Trophism In Vivo. *Cell Rep.* **10**, 1269–1279 (2015).

90. Liu, J. C. *et al. MICU1 Serves as a Molecular Gatekeeper to Prevent In Vivo Mitochondrial Calcium Overload*. *Cell Reports* **16**, (2016).

91. Beatrice, M. C., Stiers, D. L. & Pfeiffer, D. R. Increased permeability of mitochondria during Ca2+ release induced by t-butyl hydroperoxide or oxalacetate. The effect of ruthenium red. *J. Biol. Chem.* **257**, 7161–7171 (1982).

92. Vercesi, A. E., Ferraz, V. L., Macedo, D. V. & Fiskum, G. Ca2+-dependent NAD(P)+-induced alterations of rat liver and hepatoma mitochondrial membrane permeability. *Biochem. Biophys. Res. Commun.* **154**, 934–941 (1988).

93. Frank, S. *et al.* The Role of Dynamin-Related Protein 1, a Mediator of Mitochondrial Fission, in Apoptosis. *Dev. Cell* **1**, 515–525 (2001).

94. Lee, Y.-J., Jeong, S.-Y., Karbowski, M., Smith, C. L. & Youle, R. J. Roles of the Mammalian Mitochondrial Fission and Fusion Mediators Fis1, Drp1, and Opa1 in Apoptosis. *Mol. Biol. Cell* **15**, 5001–5011 (2004).

95. Youle, R. J. & Karbowski, M. Mitochondrial fission in apoptosis. *Nat. Rev. Mol. Cell Biol.* **6**, 657–663 (2005).

96. McCormack, J. G. & Denton, R. M. The effects of calcium ions and adenine nucleotides on the activity of pig heart 2-oxoglutarate dehydrogenase complex. *Biochem. J.* **180**, (1979).

97. Denton, R. M., Randle, P. J. & Martin, B. R. Stimulation by calcium ions of pyruvate dehydrogenase phosphate phosphatase. *Biochem. J.* **128**, 161–3 (1972).

98. Paillard, M. *et al.* MICU1 Interacts with the D-Ring of the MCU Pore to Control Its Ca2+ Flux and Sensitivity to Ru360. *Mol. Cell* **72**, 1–8 (2018).

99. Makino, C. L. *et al.* Recoverin Regulates Light-dependent Phosphodiesterase Activity in Retinal Rods. *J. Gen. Physiol.* **123**, 729–741 (2004).

100. Mendez, A. *et al.* Role of guanylate cyclase-activating proteins (GCAPs) in setting the flash sensitivity of rod photoreceptors. *Proc. Natl. Acad. Sci.* **98**, 9948–9953 (2001).

101. Sakurai, K., Chen, J. & Kefalov, V. J. Role of guanylyl cyclase modulation in mouse cone phototransduction. *J. Neurosci.* **31**, 7991–8000 (2011).

102. Sakurai, K., Chen, J., Khani, S. C. & Kefalov, V. J. Regulation of Mammalian Cone Phototransduction by Recoverin and Rhodopsin Kinase. *J. Biol. Chem.* **290**, 9239–9250 (2015).

103. Lamb, T. D. & Pugh, E. N. J. A quantitative account of the activation steps involved in phototransduction in amphibian photoreceptors. *J. Physiol.* **449**, 719–758 (1992).

104. Tarboush, R., Chapman, G. B. & Connaughton, V. P. Ultrastructure of the distal retina of the adult zebrafish, Danio rerio. *Tissue Cell* **44**, 264–279 (2012).

105. Ma, E. Y. *et al.* Loss of Pde6 reduces cell body Ca(2+) transients within photoreceptors. *Cell Death Dis.* **4**, e797 (2013).

106. Nag, T. C. & Wadhwa, S. Immunolocalisation pattern of complex IV in ageing human retina: Correlation with mitochondrial ultrastructure. *Mitochondrion* **31**, 20–32 (2016).

107. McWilliams, T. G. *et al.* Basal Mitophagy Occurs Independently of PINK1 in Mouse Tissues of High Metabolic Demand. *Cell Metab.* **27**, 439-449. (2018).

108. Barnhart, E. L. Mechanics of mitochondrial motility in neurons. *Curr. Opin. Cell Biol.* **38**, 90–99 (2016).

109. MacAskill, A. F. *et al.* Miro1 Is a Calcium Sensor for Glutamate Receptor-Dependent Localization of Mitochondria at Synapses. *Neuron* **61**, 541–555 (2009).

110. Wang, X. & Schwarz, T. L. The Mechanism of Ca2+-Dependent Regulation of Kinesin-Mediated Mitochondrial Motility. *Cell* **136**, 163–174 (2009).

111. Calkins, M. J. & Reddy, P. H. Amyloid beta impairs mitochondrial anterograde transport and degenerates synapses in Alzheimer's disease neurons. *Biochim. Biophys. Acta - Mol. Basis Dis.* **1812**, 507–513 (2011).

112. Vinberg, F. & Kefalov, V. J. Investigating the Ca2+-dependent and Ca2+-independent mechanisms for mammalian cone light adaptation. *Sci. Rep.* **8**, 15864 (2018).

113. Cooper, L. L. *et al.* Rod Photoreceptor Function in Children With Mitochondrial Disorders. *Arch. Ophthalmol.* **120**, 1055–1062 (2002).

114. Krizaj, D. & Copenhagen, D. R. Calcium regulation in photoreceptors. *Front Biosci.* **7**, d2023–d2044 (2002).

115. Du, J. *et al.* Phototransduction Influences Metabolic Flux and Nucleotide Metabolism in Mouse Retina. *J. Biol. Chem.* **291**, 4698–710 (2016).

116. Mammucari, C. *et al.* Mitochondrial calcium uptake in organ physiology: from molecular mechanism to animal models. *Pflügers Arch. - Eur. J. Physiol.* 1–15 (2018). doi:10.1007/s00424-018-2123-2

117. Kennedy, B. N. *et al.* Identification of a Zebrafish Cone Photoreceptor–Specific Promoter and Genetic Rescue of Achromatopsia in the nof Mutant. *Investig. Opthalmology Vis. Sci.* **48**, 522–529 (2007).

118. Brockerhoff, S. E. Genome Editing to Study Ca2+ Homeostasis in Zebrafish Cone Photoreceptors. *Adv. Exp. Med. Biol.* **1016**, 91–100 (2017).

119. Villefranc, J. A., Amigo, J. & Lawson, N. D. Gateway compatible vectors for analysis of gene function in the zebrafish. *Dev. Dyn.* **236**, 3077–3087 (2007).

120. Kremers, G.-J., Goedhart, J., van den Heuvel, D. J., Gerritsen, H. C. & Gadella, T. W. J. Improved Green and Blue Fluorescent Proteins for Expression in Bacteria and Mammalian Cells. *Biochemistry* **46**, 3775–3783 (2007).

121. Tang, R., Dodd, A., Lai, D., McNabb, W. C. & Love, D. R. Validation of zebrafish (Danio rerio) reference genes for quantitative real-time RT-PCR normalization. *Acta Biochim. Biophys. Sin. (Shanghai).* **39**, 384–90 (2007).

122. McCurley, A. T. *et al.* Characterization of housekeeping genes in zebrafish: male-female differences and effects of tissue type, developmental stage and chemical treatment. *BMC Mol. Biol.* **9**, 102 (2008).

123. Andersen, C. L., Jensen, J. L. & Ørntoft, T. F. Normalization of real-time quantitative reverse transcription-PCR data: a model-based variance estimation approach to identify genes suited for normalization, applied to bladder and colon cancer data sets. *Cancer Res.* **64**, 5245–50 (2004).

124. Vandesompele, J. *et al.* Accurate normalization of real-time quantitative RT-PCR data by geometric averaging of multiple internal control genes. *Genome Biol.* **3**, 0034.1–0034.11 (2002).

125. Preibisch, S., Saalfeld, S. & Tomancak, P. Globally optimal stitching of tiled 3D microscopic image acquisitions. *Bioinformatics* **25**, 1463–5 (2009).

126. Schmitt, E. A. & Dowling, J. E. Early retinal development in the zebrafish, Danio rerio: light and electron microscopic analyses. *J. Comp. Neurol.* **404**, 515–536 (1999).

127. Giarmarco, M. M., Cleghorn, W. M., Hurley, J. B. & Brockerhoff, S. E. Preparing Fresh Retinal Slices from Adult Zebrafish for Ex Vivo Imaging Experiments. *J. Vis. Exp.* **135**, e56977 (2018).

128. Vinberg, F. & Kefalov, V. Simultaneous ex vivo Functional Testing of Two Retinas by in vivo Electroretinogram System. *J. Vis. Exp.* **99**, e52855 (2015).

129. Vinberg, F., Kolesnikov, A. V. & Kefalov, V. J. Ex Vivo ERG analysis of photoreceptors using an In Vivo ERG system. *Vis. Res.* **101**, 108–117 (2014).

130. Du, J. *et al.* Inhibition of mitochondrial pyruvate transport by zaprinast causes massive accumulation of aspartate at the expense of glutamate in the retina. *J. Biol. Chem.* **288**, 36129–40 (2013).

131. Du, J. *et al.* Cytosolic reducing power preserves glutamate in retina. *Proc. Natl. Acad. Sci.* **110**, 18501–6 (2013).

132. Du, J., Linton, J. D. & Hurley, J. B. Chapter Four – Probing Metabolism in the Intact Retina Using Stable Isotope Tracers. in *Methods in Enzymology* **561**, 149–170 (2015).

133. Richardson, K. C., Jarett, L. & Finke, E. H. Embedding in Epoxy Resins for Ultrathin Sectioning in Electron Microscopy. *Stain Technol.* **35**, 313–323 (1960).

134. Andrews, R. M., Griffiths, P. G., Johnson, M. A. & Turnbull, D. M. Histochemical localisation of mitochondrial enzyme activity in human optic nerve and retina. *Br. J. Ophthalmol.* **83**, 231–235 (1999).

135. Chinchore, Y., Begaj, T., Wu, D., Drokhlyansky, E. & Cepko, C. L. Glycolytic reliance promotes anabolism in photoreceptors. *Elife* **6**, (2017).

136. Sweet, I. R. *et al.* Dynamic Perifusion to Maintain and Assess Isolated Pancreatic Islets. *Diabetes Technol. Ther.* **4**, 67–76 (2002).

137. Mammucari, C. *et al.* Molecular structure and pathophysiological roles of the Mitochondrial Calcium Uniporter. *BBA - Mol. Cell Res.* **1863**, 2457–2464 (2016).

138. Korenbrot, J. I. & Rebrik, T. I. Tuning outer segment Ca2+ homeostasis to phototransduction in rods and cones. *Adv. Exp. Med. Biol.* **514**, 179–203 (2002).

139. Ames, A., Li, Y. Y., Heher, E. C. & Kimble, C. R. Energy metabolism of rabbit retina as related to function: High cost of Na+ transport. *J. Neurosci.* **12**, 840–853 (1992).

140. Pan, X. *et al.* The physiological role of mitochondrial calcium revealed by mice lacking the mitochondrial calcium uniporter. *Nat. Cell Biol.* **15**, 1464–1472 (2013).

141. Nichols, M. *et al.* Global ablation of the mitochondrial calcium uniporter increases glycolysis in cortical neurons subjected to energetic stressors. *J. Cereb. Blood Flow Metab.* 0271678X16682250 (2016). doi:10.1177/0271678X16682250

142. Kwong, J. Q. *et al. The Mitochondrial Calcium Uniporter Selectively Matches Metabolic Output to Acute Contractile Stress in the Heart*. *Cell Reports* **12**, (2015).

143. Flicker, D., Sancak, Y., Mick, E., Goldberger, O. & Mootha, V. K. Exploring the In Vivo Role of the Mitochondrial Calcium Uniporter in Brown Fat Bioenergetics. *Cell Rep.* **27**, 1364-1375.e5 (2019).

144. Hamilton, J. *et al.* Deletion of mitochondrial calcium uniporter incompletely inhibits calcium uptake and induction of the permeability transition pore in brain mitochondria. *J. Biol. Chem.* **293**, 15652–15663 (2018).

145. Murphy, E. *et al.* Unresolved questions from the analysis of mice lacking MCU expression. *Biochem. Biophys. Res. Commun.* **449**, 384–385 (2014).

146. Giarmarco, M. M., Cleghorn, W. M., Sloat, S. R., Hurley, J. B. & Brockerhoff, S. E. Mitochondria maintain distinct Ca^{2+} pools in cone photoreceptors. *J. Neurosci.* **37**, 2689–16 (2017).

147. Huang *et al.* Isoenzymes of Pyruvate Dehydrogenase Phosphatase. *Biochemistry* **273**, 17680–17688 (1998).

148. Rasmussen, T. P. *et al.* Inhibition of MCU forces extramitochondrial adaptations governing physiological and pathological stress responses in heart. *Proc. Natl. Acad. Sci.* **112**, 9129–9134 (2015).

149. Kwong, J. Q. *et al.* The mitochondrial calcium uniporter underlies metabolic fuel preference in skeletal muscle. *JCI Insight* **3**, (2018).

150. Vinberg, F., Wang, T., Molday, R. S., Chen, J. & Kefalov, V. J. A new mouse model for stationary night blindness with mutant Slc24a1 explains the pathophysiology of the associated human disease. *Hum. Mol. Genet.* **24**, 5915–5929 (2015).

151. Holmström, K. M. *et al.* Assessment of cardiac function in mice lacking the mitochondrial calcium uniporter. *J. Mol. Cell. Cardiol.* **85**, 178–182 (2015).

152. Luongo, T. S. *et al. The Mitochondrial Calcium Uniporter Matches Energetic Supply with Cardiac Workload during Stress and Modulates Permeability Transition*. *Cell Reports* **12**, (2015).

153. Li, S. *et al.* Rhodopsin-iCre transgenic mouse line for Cre-mediated rod-specific gene targeting. *Genesis* **41**, 73–80 (2005).

154. Jeon, C. J., Strettoi, E. & Masland, R. H. The major cell populations of the mouse retina. *J*

Neurosci **18**, 8936–8946 (1998).

155. Woodruff, M. L. *et al.* Measurement of cytoplasmic calcium concentration in the rods of wild-type and transducin knock-out mice. *J. Physiol.* **542**, 843–854 (2002).

156. Matthews, H. R. & Fain, G. L. The effect of light on outer segment calcium in salamander rods. *J. Physiol.* **552**, 763–776 (2003).

157. Fain, G. L., Matthews, H. R., Cornwall, M. C. & Koutalos, Y. Adaptation in vertebrate photoreceptors. *Physiol. Rev.* **81**, 117–151 (2001).

158. Pugh, E. N., Nikonov, S. & Lamb, T. D. Molecular mechanisms of vertebrate photoreceptor light adaptation. *Curr. Opin. Neurobiol.* **9**, 410–418 (1999).

159. Nakatani, K., Chen, C., Yau, K.-W. & Koutalos, Y. Calcium and Phototransduction. in *Photoreceptors and Calcium* (eds. Baehr, W. & Palczewski, K.) 1–20 (Springer US, 2002). doi:10.1007/978-1-4615-0121-3_1

160. Csordás, G. *et al.* MICU1 Controls Both the Threshold and Cooperative Activation of the Mitochondrial Ca2+ Uniporter. *Cell Metab.* **17**, 976–987 (2013).

161. Beutner, G., Sharma, V. K., Giovannucci, D. R., Yule, D. I. & Sheu, S. S. Identification of a Ryanodine Receptor in Rat Heart Mitochondria. *J. Biol. Chem.* **276**, 21482–21488 (2001).

162. Sparagna, G. C., Gunter, K. K., Sheu, S. S. & Gunter, T. E. Mitochondrial calcium uptake from physiological-type pulses of calcium: A description of the rapid uptake mode. *J. Biol. Chem.* **270**, 27510–27515 (1995).

163. Smets, I. *et al.* Ca2+ uptake in mitochondria occurs via the reverse action of the Na+/Ca2+ exchanger in metabolically inhibited MDCK cells. *Am. J. Physiol. - Ren. Physiol.* **286**, F784–F794 (2004).

164. Doonan, P. J. *et al.* LETM1-dependent mitochondrial Ca2+ flux modulates cellular bioenergetics and proliferation. *FASEB J.* **28**, 4936–49 (2014).

165. Gunter, T. E. & Sheu, S.-S. S. *Characteristics and possible functions of mitochondrial Ca2+ transport mechanisms*. **1787**, 1291–1308 (Elsevier, 2009).

166. Lombardi, A. A. *et al.* Mitochondrial calcium exchange links metabolism with the epigenome to control cellular differentiation. *Nat. Commun.* **10**, (2019).

167. Gage, G. J., Kipke, D. R. & Shain, W. Whole animal perfusion fixation for rodents. *J. Vis. Exp.* 1–9 (2012). doi:10.3791/3564

168. Millard, P., Letisse, F., Sokol, S. & Portais, J. C. IsoCor: Correcting MS data in isotope labeling experiments. *Bioinformatics* **28**, 1294–1296 (2012).

169. Lamb, T. D. & Pugh Jr, E. N. A QUANTITATIVE ACCOUNT OF THE ACTIVATION STEPS INVOLVED IN PHOTOTRANSDUCTION IN AMPHIBIAN PHOTORECEPTORS Our description of phototransduction differs from previous models in providing a. *J. Physiol. Chabre* **449**, 719–758 (1992).

170. Ozawa, T. *Genetic and Functional Changes in Mitochondria Associated With Aging*. *REVIEWS* **77**, (1997).

171. Liesa, M. & Shirihai, O. S. Mitochondrial dynamics in the regulation of nutrient utilization and energy expenditure. *Cell Metabolism* **17**, 491–506 (2013).

172. Görlach, A. *et al.* Reactive oxygen species, nutrition, hypoxia and diseases: Problems solved? *Redox Biology* **6**, 372–385 (2015).

173. Hahn, A. & Zuryn, S. Mitochondrial genome (mtDNA) mutations that generate reactive oxygen

species. *Antioxidants* **8**, 392 (2019).

174. Schieber, M. & Chandel, N. S. ROS function in redox signaling and oxidative stress. *Current Biology* **24**, R453 (2014).

175. Guo, C. Y., Sun, L., Chen, X. P. & Zhang, D. S. Oxidative stress, mitochondrial damage and neurodegenerative diseases. *Neural Regen. Res.* **8**, 2003–2014 (2013).

176. Chen, Y. & Sheng, Z.-H. Kinesin-1-syntaphilin coupling mediates activity-dependent regulation of axonal mitochondrial transport. *J. Cell Biol.* **202**, 351–64 (2013).

177. Caino, M. C. *et al.* Syntaphilin controls a mitochondrial rheostat for proliferation-motility decisions in cancer. in *Journal of Clinical Investigation* **127**, 3755–3769 (American Society for Clinical Investigation, 2017).

178. Baloh, R. H. Mitochondrial Dynamics and Peripheral Neuropathy. *Neuroscientist* **14**, 12–18 (2008).

179. Beal, M. F. Mitochondrial dysfunction in neurodegenerative diseases. *Biochim. Biophys. Acta - Bioenerg.* **1366**, 211–223 (1998).

180. Suzuki, S. C. *et al.* Cone photoreceptor types in zebrafish are generated by symmetric terminal divisions of dedicated precursors. *Neurosci. Downloaded Univ. Washingt. March* **110**, 2020 (2013).

181. Byrnes, J. *et al.* Pharmacologic modeling of primary mitochondrial respiratory chain dysfunction in zebrafish. *Neurochem. Int.* **117**, 23–34 (2018).

182. Tseng, Y. C. *et al.* Exploring uncoupling proteins and antioxidant mechanisms under acute cold exposure in brains of fish. *PLoS One* **6**, (2011).

183. McWilliams, T. G. *et al.* A comparative map of macroautophagy and mitophagy in the vertebrate eye. *Autophagy* **15**, 1296–1308 (2019).

184. Toyama, E. Q. *et al.* Metabolism: AMP-activated protein kinase mediates mitochondrial fission in response to energy stress. *Science (80-.).* **351**, 275–281 (2016).

185. Wu, S., Zhou, F., Zhang, Z. & Xing, D. Mitochondrial oxidative stress causes mitochondrial fragmentation via differential modulation of mitochondrial fission-fusion proteins. *FEBS J.* **278**, 941–954 (2011).

186. Qi, X., Disatnik, M. H., Shen, N., Sobel, R. A. & Mochly-Rosen, D. Aberrant mitochondrial fission in neurons induced by protein kinase Cδ under oxidative stress conditions in vivo. *Mol. Biol. Cell* **22**, 256–265 (2011).

187. Rambold, A. S., Kostelecky, B., Elia, N. & Lippincott-Schwartz, J. Tubular network formation protects mitochondria from autophagosomal degradation during nutrient starvation. *Proc. Natl. Acad. Sci. U. S. A.* **108**, 10190–10195 (2011).

188. Al, Z., Dache, A. & Tanos, R. Blood contains circulating cell-free respiratory competent mitochondria Characterization of novel neuroprotective pathways in Parkinson's disease View project Diagnostic and Prognosis Value of Circulating DNA for CRC Patients' Surveillance After Curative Treatment (ADNCirc) View project. *Artic. FASEB J.* (2020). doi:10.1096/fj.201901917RR

189. Lewis, A., Williams, P., Lawrence, O., Wong, R. O. L. L. & Brockerhoff, S. E. Wild-type cone photoreceptors persist despite neighboring mutant cone degeneration. *J. Neurosci.* **30**, 382–389 (2010).

190. Buj, R., Iglesias, N., Planas, A. M. & Santalucía, T. A plasmid toolkit for cloning chimeric cDNAs encoding customized fusion proteins into any Gateway destination expression vector. *BMC Mol. Biol.* **14**, (2013).

191. Tsai, M.-F., Jiang, D., Zhao, L., Clapham, D. & Miller, C. Functional reconstitution of the mitochondrial Ca2+/H+ antiporter Letm1. *J. Gen. Physiol.* **143**, (2013).

192. Beutner, G., Sharma, V. K., Giovannucci, D. R., Yule, D. I. & Sheu, S. S. Identification of a ryanodine receptor in rat heart mitochondria. *J. Biol. Chem.* **276**, 21482–8 (2001).

193. Jakob, R. *et al.* Molecular and functional identification of a mitochondrial ryanodine receptor in neurons. *Neurosci. Lett.* **575**, 7–12 (2014).

194. Piao, L. *et al.* Association of LETM1 and mrpl36 contributes to the regulation of mitochondrial ATP production and necrotic cell death. *Cancer Res.* **69**, 3397–3404 (2009).

195. Tarasov, A. I., Griffiths, E. J. & Rutter, G. A. Regulation of ATP production by mitochondrial Ca2+. *Cell Calcium* **52**, 28–35 (2012).

196. Barron, M. J. *et al.* Mitochondrial abnormalities in ageing macular photoreceptors. *Investig. Ophthalmol. Vis. Sci.* **42**, 3016–3022 (2001).

197. Sadun, A. *et al.* Morphological Findings in the Visual System in a Case of Leber's Hereditary Optic Neuropathy. *Clin. Neurosci.* **2**, 165–172 (1994).

198. Adams, J., Blackwood, W. & Wilson, J. Further clinical and pathological observations on Leber's optic atrophy. *Brain* **89**, 15–26 (1966).

199. Fraser, J. A., Biousse, V. & Newman, N. J. The Neuro-ophthalmology of Mitochondrial Disease. *Surv. Opthalmology* **55**, 299–334 (2010).

200. Kiyama, T. *et al.* Essential roles of mitochondrial biogenesis regulator Nrf1 in retinal development and homeostasis. *Mol. Neurodegener.* **13**, 1–23 (2018).

201. Cox, D. A., Conforti, L., Sperelakis, N. & Matlib, M. A. Selectivity of Inhibition of Na+-Ca2+ Exchange of Heart Mitochondria by Benzothiazepine CGP-37157. *J. Cardiovasc. Pharmacol.* **21**, 595–599 (1993).

202. Jiang, D., Zhao, L., Clish, C. B. & Clapham, D. E. Letm1, the mitochondrial Ca2+/H+ antiporter, is essential for normal glucose metabolism and alters brain function in Wolf-Hirschhorn syndrome. *PNAS* **110**, E2249–E2254 (2013).

203. Uchida, K. 4-Hydroxy-2-nonenal: A product and mediator of oxidative stress. *Progress in Lipid Research* **42**, 318–343 (2003).

204. Duan, J. *et al.* Low-dose exposure of silica nanoparticles induces cardiac dysfunction via neutrophil-mediated inflammation and cardiac contraction in zebrafish embryos. *Nanotoxicology* **10**, 575–585 (2016).

205. Vegh, R. B. *et al.* Reactive oxygen species in photochemistry of the red fluorescent protein 'killer Red'. *Chem. Commun.* **47**, 4887–4889 (2011).

206. Shibuya, T. & Tsujimoto, Y. Deleterious effects of mitochondrial ROS generated by KillerRed photodynamic action in human cell lines and C. elegans. *J. Photochem. Photobiol. B Biol.* **117**, 1–12 (2012).

207. Schwarz, T. L. Mitochondrial trafficking in neurons. *Cold Spring Harb. Perspect. Biol.* **5**, a011304 (2013).

208. Ligon, L. A. & Steward, O. Role of microtubules and actin filaments in the movement of mitochondria in the axons and dendrites of cultured hippocampal neurons. *J. Comp. Neurol.* **427**, 351–361 (2000).

209. Krendel, M., Sgourdas, G. & Bonder, E. M. Disassembly of actin filaments leads to increased rate and frequency of mitochondrial movement along microtubules. *Cell Motil. Cytoskeleton* **40**, 368–

378 (1998).

210. Quintero, O. A. *et al.* Human Myo19 Is a Novel Myosin that Associates with Mitochondria. *Curr. Biol.* **19**, 2008–2013 (2009).

211. Chen, Y. & Sheng, Z.-H. Kinesin-1-syntaphilin coupling mediates activity-dependent regulation of axonal mitochondrial transport. *J. Cell Biol.* **202**, 351–64 (2013).

212. Mateos, J. M. *et al.* Correlative super-resolution and electron microscopy to resolve protein localization in zebrafish retina. *J. Vis. Exp.* **2017**, e56113 (2017).